$LaBr_3$ gamma-ray spectrometers for space applications

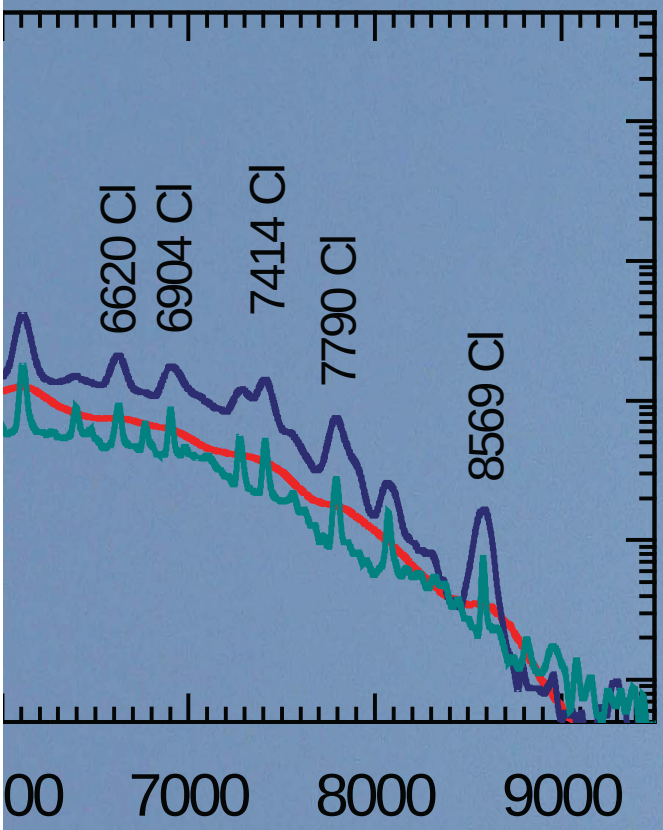

Francesco Quarati

Cover:
chorine-neutron-activation prompt-gamma-ray-spectra collected with $LaBr_3$, HPGe and NaI spectrometers at the Czech Metrology Institute in collaboration with the Institute of Experimental and Applied Physics of the Czech Technical University, both in Prague, Czech Republic.

$LaBr_3$ gamma-ray spectrometers for space applications

Proefschrift

ter verkrijging van de graad van doctor
aan de Technische Universiteit Delft,
op gezag van de Rector Magnificus prof. ir. K.C.A.M. Luyben,
voorzitter van het College voor Promoties,
in het openbaar te verdedigen op dinsdag 22 januari 2013 om 15:00 uur
door Francesco Giovanni Andrea QUARATI
Dottore in Ingegneria Nucleare, Politecnico di Torino
geboren te Cagliari, Italie

Dit proefschrift is goedgekeurd door de promotor:

Prof. dr P. Dorenbos

Samenstelling promotiecommissie:

Rector Magnificus, voorzitter	
Prof. dr. P. Dorenbos	Technische Universiteit Delft, promotor
Prof. dr. F.J. Beekman	Technische Universiteit Delft
Prof. dr. C. Pappas	Technische Universiteit Delft
Prof. dr. ir. E. Charbon	Technische Universiteit Delft
Prof. dr. F. Camera	Università di Milano
Prof. dr S. Brandenburg	Rijksuniversiteit Groningen
Dr. A. Owens	European Space Agency

Printed by: Proefschriftmaken.nl || Uitgeverij BOXPress

ISBN 9789088915642

December 2012

Contents

List of acronyms and abbreviations

AU	Astronomical Unit (149.6×10^6 km)
ESA	European Space Agency
FWHM	Full Width Half Maximum
FWTM	Full Width one-Tenth of the Maximum
HPGe	High Purity Germanium Detector
$LaBr_3$	Lanthanum bromide; if not otherwise specified it refers to the standard $LaBr_3$:Ce5% (5% doped Cerium)
LO	(Scintillation) Light Output, synonym of LY
LY	(Scintillation) Light Yield
MANGA	Mercury Analysis of Neutrons and GAmma-rays
MGNS	Mercury Gamma-Ray and Neutron spectrometer
MMO	Mercury Magnetospheric Orbiter (BepiColombo)
MPO	Mercury Planetary Orbiter (BepiColombo)
phe	photo-electron
PMT	Photo Multiplier Tube
QE	Quantum Efficiency
R&D	Research and Development
rms	root mean squared
SDD	Silicon Drift Detector
SiPM	Silicon Photo Multiplier
SPC	Science Programme Committee
sphe	Single photo-electron
TU Delft	Delft University of Technology
VD	Voltage divider referred to PMT operation
Z_{eff}	Effective atomic number, evaluated using: $Z_{eff} = \sqrt[2.94]{f_1 \times Z_1^{2.94} + f_2 \times Z_2^{2.94} + \ldots + f_n \times Z_n^{2.94}}$ where f is the fraction of the total number of electrons associated with each element and Z its atomic number

Chapter 1

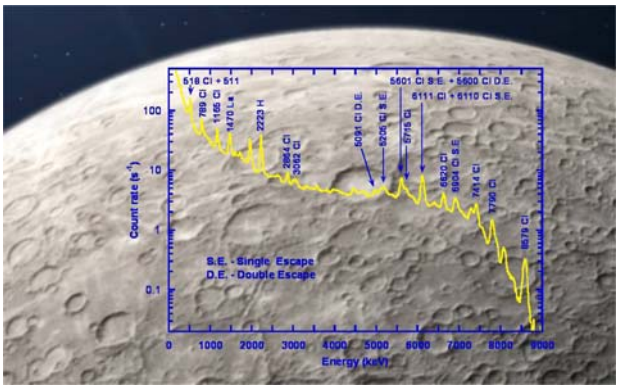

Introduction

This thesis presents my research activity supporting the space application of $LaBr_3$ scintillator detectors and of other high energy resolution scintillators such as $LaCl_3$ and $CeBr_3$. The thesis focuses on the essential aspects related to a successful utilization of $LaBr_3$ for application in gamma-ray spectrometry of planetary surfaces and provides the scientific and technical support needed for the design of a flight instrument.

At its beginning, the thesis progressed in the frame of a research and development programme initiated by the European Space Agency (ESA) and involving Saint Gobain Crystals & Detectors, the Delft University of Technology, and Cosine Research BV. The programme aimed to advance crystal growth technology in order to produce large volume $LaBr_3$ crystals for space applications. In the last two years, the thesis research was conducted within a new project, again initiated by ESA, for the development of $CeBr_3$ scintillator detectors and involving the Delft University of Technology, Præsepe BV, Scionix BV, Schott AG and more recently Hellma Materials GmbH.

In 2006, $LaBr_3$ was selected as the detection medium for the onboard gamma-ray spectrometer for the BepiColombo space mission to Mercury. Such a decision, which was strongly based on the radiation tolerance assessment presented in this thesis, required extensive experimental research aimed at acquiring a deep knowledge and expertise on the $LaBr_3$ scintillator detectors.
This introduction provides an overview of the thesis, including its scientific goals and challenges. It does also include an introduction to the fundamental properties of $LaBr_3$, which made it particularly attractive for space applications and a description of technical constraints for the gamma-ray spectrometer onboard BepiColombo.

1 Thesis's historical and scientific overview

I have worked on the subject of this thesis since 2005, not as a full time PhD student, but in parallel with my duties as employee of Praesepe BV. At the beginning, I was hired by ESA to support R&D programmes on novel radiation detectors, including compound semiconductors, and then, from 2010 as a guest researcher at TU Delft in the frame of a project to explore new scintillator materials potentially superseding $LaBr_3$.
The idea of this thesis started in 2006 during discussions with my senior colleague Dr Alan Owens of ESA, who also accepted to become senior advisor. The thesis was supported by the former head of ESA's Science Payload and Advance Concepts Office, Dr Antony Peacock, and by the Office's project controller, Ms Renee Fontaine. Thanks as well to their substantial help, it was possible to set up a collaboration with Prof. Pieter Dorenbos of TU Delft, who then in 2007 welcomed me as a guest PhD student in the Luminescence Material Laboratory, which he leads.
At the time I started working in ESA, numerous R&D programmes were on-going, aimed at the implementation of innovative radiation detectors for applications in space science. The main focus was on compound semiconductors, such as CdZnTe and TlBr. The discovery of $LaBr_3$ by TU Delft and Bern University opened new perspectives in the field. In fact, early results obtained with small volume samples of these scintillators triggered significant interest because of the promise of making available novel gamma-ray spectrometers with energy resolution approaching that of compound semiconductors but of much larger size resulting in substantial enhancement of the detection efficiency. Consequently ESA decided to initiate a R&D programme involving the Delft University of Technology, Saint Gobain Crystals & Detectors and Cosine Research BV to advance crystal growth technology. The programme aimed the implementation and production of large volume spectroscopic detectors based on $LaBr_3$ and $LaCl_3$ for which a concrete application would have been the gamma-ray spectrometer onboard the BepiColombo mission to Mercury [1].
After the release of BepiColombo's science requirements in 2004 [2], it was in fact envisaged that a gamma-ray spectrometer based on $LaBr_3$ could compete in terms of scientific performance with High Purity Germanium (HPGe) spectrometers [3] and with additional benefits in term of spacecraft's mass and power resource allocation, instrument reliability and robustness.
ESA's Science Programme Committee (SPC) and the BepiColombo Mission Definition Board decided to undertake a period of investigation before orienting the choice for the onboard gamma-ray spectrometer. Two instrument concepts were considered: the $LaBr_3$-based Mercury Gamma-Ray and Neutron spectrometer (MGNS) and the HPGe-based Mercury Analysis of Neutrons and

GAmma-rays (MANGA). A description of both instruments can be found in [4] and [5] respectively.
While $LaBr_3$ crystal growth technology was being developed, extensive radiation hardness tests were carried out on both precursor samples of $LaBr_3$ scintillators and HPGe spectrometers, in order to characterize their radiation tolerances. These tests and their results are the subject of Chapter 2. After extensive experimental investigations, early in 2006 $LaBr_3$ was selected for implementation as the onboard gamma-ray spectrometer.
This success required new research and investigations. Specifically, before flying $LaBr_3$ into the space environment, extensive experiments and studies were needed in order to acquire knowledge and expertise on this novel technology. Such research included synchrotron campaigns exploring $LaBr_3$ response below 100 keV, as presented in Chapter 3, also providing information on the suitability of $LaBr_3$ in x-ray astronomy. It was also necessary to verify whether, and to what extent, the properties of small crystals would scale to larger volume spectrometers. This is reported in Chapter 4. Experiments were then carried out to explore detection performances for high energy gamma-rays and the necessary capabilities to successfully calibrate and operate $LaBr_3$ spectrometer in space. In fact, $LaBr_3$ spectrometers due to their bright and fast scintillation pulses pose serious challenges to the scintillation readout.
Due to the BepiColombo mission schedule and budget constraints, the ideal solution of developing a novel and tailored scintillation readout could not be pursued in a synchronized programme and great effort was then devoted to develop effective solutions based on current readout technology able to optimize the spectrometer performance. This involved experimental campaigns with gamma-ray energies up to 15 MeV. Chapter 5 deals with these aspects. Moreover, the most serious limitation of $LaBr_3$ is the presence of the natural occurring radioactive isotope ^{138}La, which contributes to the so called intrinsic activity and limits instrument sensitivity. Of particular significance for space applications is the overlapping of the gamma-ray of ^{138}La with the gamma-ray of ^{40}K, whose detection is of interest in studies of planetary formation. It is towards the development of an intrinsic background clean spectrometer, potentially superseding $LaBr_3$ in terms of sensitivity, that recent efforts have been focused, implementing an alternative scintillator detector based on $CeBr_3$. Large volume samples of this scintillator are currently under study.

2 An overview of $LaBr_3$ scintillators

$LaBr_3$ scintillator detectors, discovered at Delft University of Technology and the University of Bern [6,7], have revolutionized spectroscopic systems because of their excellent energy resolution compared with traditional scintillators as NaI(Tl) and CsI(Na). $LaBr_3$, namely $LaBr_3$:Ce5%, has a fast scintillation decay time of 16 ns. Its scintillation emission spectrum extends from about 340 nm to 410 nm and peaks at 380 nm. Such emission matches the maximum quantum efficiency region of typical photomultiplier tubes (PMTs) with bialkali photocathode, making scintillation light collection rather efficient. The absolute light yield of $LaBr_3$ is > 60 000 photons per MeV of absorbed gamma-ray energy or 165% relative to a standard NaI(Tl) scintillator. The material density is 5.07 g/cm^3. At the start of this thesis, energy resolutions FWHM of 3% at 662 keV (^{137}Cs radioactive source) were reported for small volume crystals.

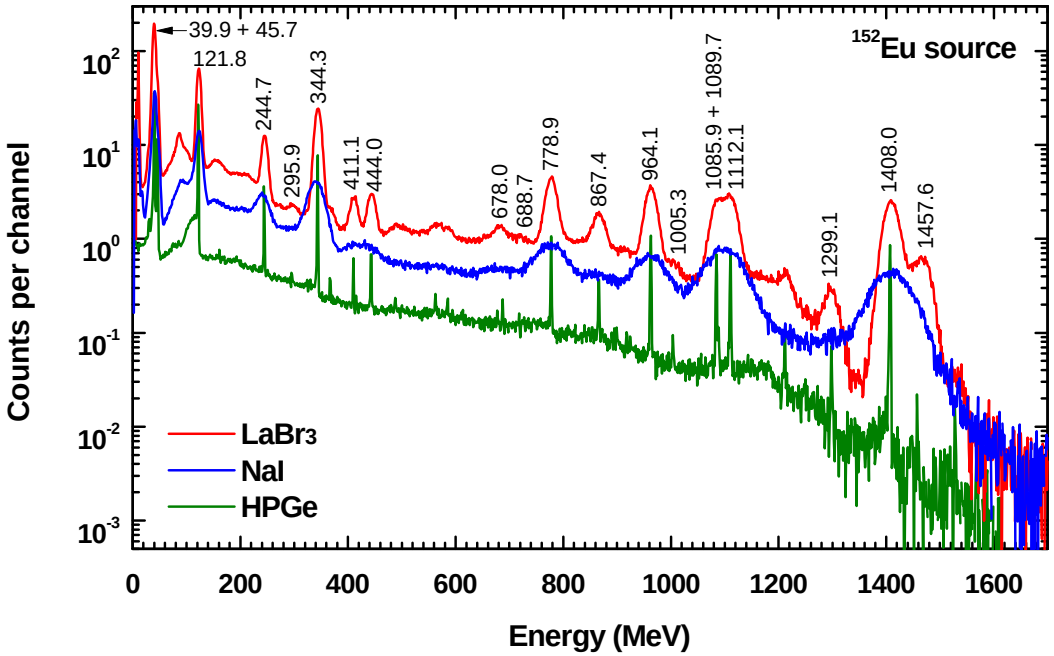

Fig. 1 – Pulse height spectra of ^{152}Eu acquired with HPGe, NaI(Tl) and $LaBr_3$.

A fundamental measurement of a radiation detector operated in pulse mode is the acquisition of a differential pulse height spectrum of a radioactive source, briefly called the pulse height spectrum. In it, the abscissa is divided in bins and represents the amplitude of the pulses generated in the detector by the impinging radiation. The ordinate represents the occurrence of a pulse of amplitude falling within a certain bin. Fig. 1 compares three pulse height spectra of an ^{152}Eu radioactive source. Two spectra are collected with standard gamma-ray spectrometers: NaI(Tl) scintillator and a liquid nitrogen cooled HPGe semiconductor; and one spectrum with $LaBr_3$. Even if the energy resolution of

HPGe is unchallenged by $LaBr_3$, it can be seen that the latter is still able to resolve virtually all of the gamma-ray lines emitted by ^{152}Eu.
However, lanthanum is characterized by the presence of the 0.09% of natural occurring isotope ^{138}La, which is also found in $LaBr_3$ spectrometer. ^{138}La radioactive decays strongly contribute in increasing the background of pulse height spectra, ultimately limiting the $LaBr_3$ sensitivity. The contribution to the background due to ^{138}La is typically of the order of 1.5 Bq/cm^3 and is distributed across an energy rage from few keV up to 1.5 MeV.

3 The gamma-ray spectrometer onboard BepiColombo

Gamma-ray spectroscopy is an established technique that has played a significant role in planetary exploration by determining elemental compositions of the Moon and Mars [8,9,10]. The technique was also baselined for surface composition studies of Mercury [11,12].
Spectroscopic gamma-ray measurements allow for the identification of nuclides, thereby giving information on the elemental composition of the object under observation (Fig. 2). In the context of planetary exploration, gamma-rays arise primarily from two sources: gamma-rays emitted spontaneously by naturally occurring radio-nuclides like ^{40}K, ^{232}Th and gamma-ray emission induced by cosmic-ray interaction with elements such as Fe, Si, H, C and O. Depending on gamma-ray escape probability, information on the composition of up to several tens of centimetres below the surface can be achieved [13].
Gamma-ray spectroscopy can be applied at a specific location of a planet by a landing vehicle or remotely from orbit provided that absorption from the planetary atmosphere is absent or not too strong.
Whereas gamma-ray measurements provide information on soil elemental composition, wider scientific value is achieved by combining gamma-ray detection with neutron detection. Neutrons are strongly moderated by water, therefore, if the neutron detector can discriminate at least thermal and epithermal neutrons, the presence of water can be indirectly observed.
In the case of BepiColombo, the gamma-ray spectrometer will operate from orbit and the expected integrated gamma-ray fluxes are therefore weak and probably of the order of few counts per second [14]. Therefore high detection photopeak efficiency becomes necessary to accomplish the scientific objectives. High detection efficiency is achieved with large volume detectors whose elementary composition includes materials with high atomic number Z. For the BepiColombo scientific goals, energy resolution of 1% at 1 MeV and relative

detection efficiency of 3% around 6 MeV are required [2]. The detection efficiency requirement is comfortably compatible with typical 3″×3″ scintillator but at the limit for HPGe operating in space. However, the energy resolution of scintillators was considered too poor to satisfy the energy resolution requirements for remote-sensing gamma-ray spectrometers, limiting their ability to uniquely separate the elemental gamma-ray lines emanating from the surface of the planet. The discovery of $LaBr_3$ allowed a reconsideration of using scintillator detectors for such applications as can be seen in Fig. 1. Hence, a revised set of science requirements was submitted to the Mission Definition Board and approved. The new requirements, specifically applying to novel scintillator spectrometers, relaxed the need in energy resolution to < 3% at 1 MeV provided that the no compromise was made on the photopeak detection efficiency. $LaBr_3$ did comfortably fit in, provided that its energy resolution did not deteriorate with the scaling up of samples size.

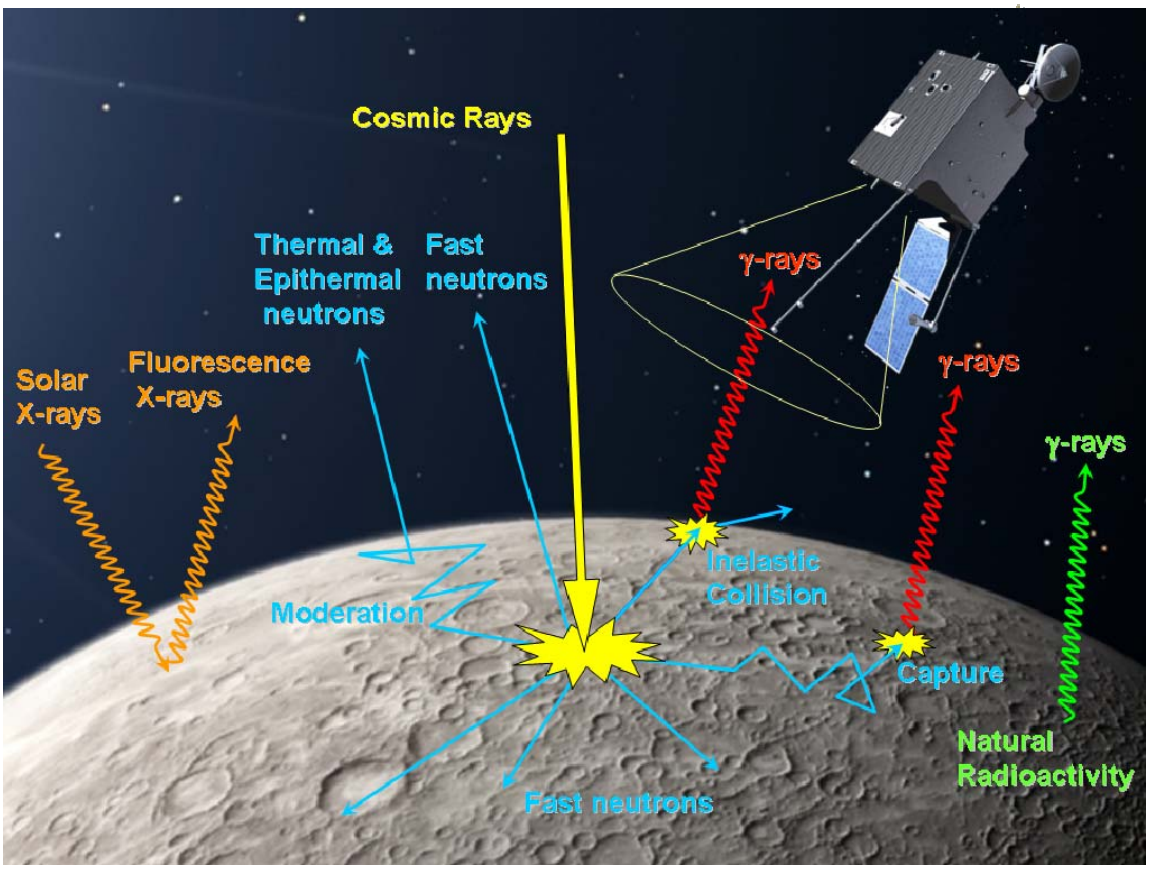

Fig. 2 –Formation of gamma-ray signature lines from a planetary surface by natural occurring radioactivity and by cosmic ray interactions.

In the case of BepiColombo an extremely strict resource allocation was a fundamental aspects of spacecraft design. All space missions face the need to minimize payload mass and power demands, since both resources are limited in space. Compared to near Earth missions, for exploration missions such as

BepiColombo, spacecraft resources are even more limited due to the high demand for fuel which for spacecraft designers leaves no other option than to further reduce payload mass and power demands.
BepiColombo comprises two different spacecrafts: the Mercury Planetary Orbiter (MPO) and the Mercury Magnetospheric Orbiter (MMO). The mission is a collaboration between ESA and the Japan Aerospace Exploration Agency (JAXA). For BepiColombo, in spite of a mass at launch of over 4 tonnes, the available total payload mass (MPO+MMO) is only 125 kg.
For the MPO alone, which will carry the gamma-ray spectrometer, the total resources for the payload are limited to a maximum volume of 1 m^3, a power consumption of about 70 W and a total payload mass of about 50 kg.
The original baseline payload comprised of 12 instruments, which means that on average, instruments will weight about 4.2 kg and consume about 5.8 W of power. Given such exiguous resources, boarding an HPGe spectrometer posed extreme complications. In fact, passive cooling cannot be implemented in view of the relatively large radiator area needed and the proximity of the spacecraft to both the planet and the Sun. Therefore a mechanical refrigerator would be required which in turn raises mass, power and reliability issues as well as limiting the maximum operable volume of the HPGe. For MANGA, the proposed HPGe had dimension of a right circular cylinder, 6 cm in diameter and 6 cm in height (~145 cm^3 of active volume) and requiring an allocation of 6.5 kg and 16 W of power for cooling down to an operational temperature of 90 K. The nominal detection efficiency at 6 MeV was estimated to be 3% [3].

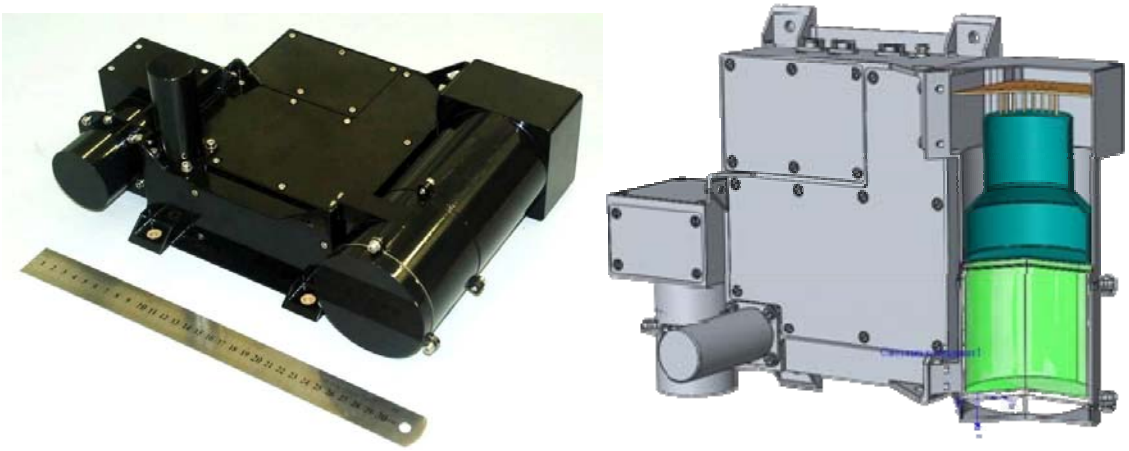

Fig. 4 – Picture of the demonstration module of the MGNS (left) and its technical drawing, highlighting in green the position of the $LaBr_3$ crystal (right), courtesy of M. Mokrousov, IKI, Moscow.

Overestimation of available payload allocation already led BepiColombo nearly to project cancellation and only the acquisition of extra budget needed to upgrade launch capabilities using a far more expensive Ariane V vehicle has

restored the project in 2009. The mission complexity can be quantified by keeping in mind the time already elapsed since its first proposal in 1993 up to the presently scheduled launch date 2014, i.e. 21 years.
With the availability of an Ariane V, payload resources for the MPO rose to 80 kg and 100 W. However, all the above strongly oriented the BepiColombo Mission Definition Board towards low-resource demanding options such as scintillator detectors for the onboard gamma-ray spectrometer. The decision was confirmed following the results of the radiation assessments presented in this thesis. The development of the gamma-ray and neutron spectrometer onboard BepiColombo (MGNS) was assigned to the Space Research Institute of the Russian Academy of Sciences (IKI RAS) in Moscow with principal investigator Dr I.G. Mitrofanov [3,13]. The instrument is funded by the Federal Space Agency of the Russian Federation and comprises of two parts, the gamma-ray spectrometer ($LaBr_3$) and a neutron detector with spectroscopic capability (Fig. 4).

4 Physical and technological background concepts

For all physical and technological concepts related to gamma-ray spectroscopy, including gamma-ray remote sensing, and the basic characteristics of scintillator and HPGe spectrometers, the thesis refers to the following books:

1) G.F. Knoll, Radiation Detection and Measurements, third ed., Wiley & Sons Ltd., New York, 2000;

2) G. Gilmore, Practical Gamma-ray Spectroscopy, second ed., Wiley & Sons Ltd., Chichester, 2008;

3) L. G. Evans, R. C. Reedy, and J. I. Trombka, Introduction to Planetary Remote-Sensing Gamma-ray Spectroscopy, in Remote Geochemical Analysis: Geochemical and Mineralogical Composition, ed. C. Pieters and P. Englert, Cambridge University Press, New York, 1993.

References

[1] BepiColombo http://bepicolombo.esa.int

[2] BepiColombo Science Requirements, European Space Agency (2004), SCI-PB-RS-1156.

[3] Alan Owens, "Comparative performance of the Mercury Gamma-Ray and Neutron Spectrometer (MGNS)", BepiColombo Internal Report, 2004. Available on request from the author.

[4] I.G. Mitrofanov et al., "The Mercury Gamma and Neutron Spectrometer (MGNS) onboard the Planetary Orbiter of the BepiColombo mission", Planetary and Space Sci. 58 (2010) 116.

[5] B. Pirard, "Etude et validation d'un spectrometer gamma pour la mesure de la composition chimique des surfaces planétaires. Application à une mission vers Mercure", Université Toulouse III (2006) (PhD thesis, French language).

[6] E.V.D. van Loef et al., "High-energy-resolution scintillator: Ce activated $LaBr_3$", Appl. Phys. Lett., 79 (2001) 1573.

[7] P. Dorenbos et al., "Gamma Ray Spectroscopy with a Ø19×19 mm^3 $LaBr_3$:0.5% Ce^{3+} Scintillator", IEEE Trans. Nucl. Sci., 51 (2004) 1289.

[8] T.M. Harrington et al., "The Apollo gamma-ray spectrometer", Nucl. Instr. and Meth., 118 (1974) 401.

[9] W.C. Feldman et al., "The Lunar Prospector gamma-ray and neutron spectrometers", Nucl. Instr. and Meth. A, 422 (1999) 562.

[10] W.V. Boynton et al., "The Mars Odyssey Gamma-Ray Spectrometer Instrument Suite", Space Science Reviews, 110 (2004) 37.

[11] R.E. Gold et al., "The MESSENGER mission to Mercury: scientific payload", Planetary and Space Science, 49 (2001) 1467.

[12] A. Anselmi and G.E.N. Scoon, "BepiColombo, ESA's Mercury Cornerstone mission", Planetary and Space Sci., 49 (2001) 1409.

[13] http://grs.lpl.arizona.edu/home.jsp

[14] J. Bruckner and J. Masarik, "Planetary gamma-ray spectroscopy of the surface of Mercury", Planet. Space Sci. 45 (1997) 39.

[15] http://l503.iki.rssi.ru/index-en.html

Chapter 2

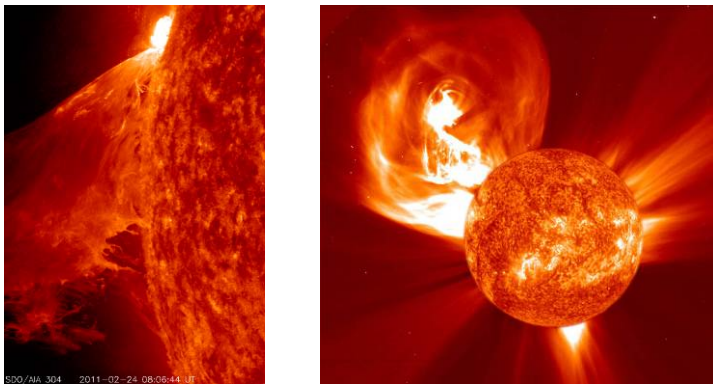

Courtesy of SDO/NASA and of SOHO/ESA & NASA

Radiation tolerance assessments

This chapter discusses a fundamental aspect in the process of evaluation and design of instruments for space applications: the assessment of their radiation tolerance.

The radiation assessments presented are specific and designed for the BepiColombo mission to Mercury, taking into account the planet's position in the inner solar system. This makes the radiation tolerance requirements more severe than for missions to the outer solar system, e.g. a mission to Mars.

In practice, there are not existing precursors of exploration missions flying and operate so close to the Sun as BepiColombo and an original radiation tolerance assessment has been implemented based on the best available models of solar activity and relative intensity.

The main achievements of an exhaustive effort to address the choice for the gamma-ray spectrometer onboard BepiColombo are reported. Two options have been evaluated and compared, one based on HPGe and the second on $LaBr_3$:Ce.

The results showed that $LaBr_3$:Ce withstands Mercury's harsh radiation environment without substantial impact on its performance. Whereas, a HPGe detector may suffer of a substantial reduction in its capability and it is questionable whether it could achieve its scientific objective.
The results of the following experiments together with mission resource allocation constraints, let the BepiColombo Mission Definition Board to opt in favour of a $LaBr_3$:Ce solution to the onboard gamma-ray spectrometer.

The content of this chapter is based on the following publications:

Quarati, F., Brandenburg, S., Buis, E.-J., Dressler, P., Kraft, S., Lampert, M.-O., Ostendorf, R.W., Owens, A., Peacock, A., Quirin, P., Quirion, D.
Solar proton event damage in space-borne Ge detectors
Nucl. Instr. and Meth. A 610 (2009) 354
DOI: 10.1016/j.nima.2009.05.108

Owens, A., Brandenburg, S., Buis, E.-J., Kiewiet, H., Kraft, S., Ostendorf, R.W., Peacock, A., Quarati, F., Quirin, P.
An assessment of radiation damage in space-based germanium detectors due to solar proton events
Nucl. Instr. and Meth. A 583 (2007) 285
DOI: 10.1016/j.nima.2007.07.144

Owens, A., Bos, A.J.J., Brandenburg, S., Buis, E.-J., Dathy, C., Dorenbos, P., van Eijk, C.W.E., Kraft, S., Ostendorf, R.W., Ouspenski, V., Quarati, F.
Assessment of the radiation tolerance of $LaBr_3$:Ce scintillators to solar proton events
Nucl. Instr. and Meth. A 572 (2007) 785
DOI: 10.1016/j.nima.2006.12.008

and on [17,18,19,20,22,25].

1 Introduction

As mentioned in Chapter 1, to accomplish the BepiColombo scientific goals two gamma-ray spectrometers were independently proposed one based on a $LaBr_3$:Ce scintillator detector and another based on a HPGe detector.
For inner solar system missions, radiation damage is potentially a serious problem in view of long cruise phases and the inverse scaling of the solar particle fluence. Consequently, the radiation tolerance was one of the criteria used to select between the two proposed instruments.
At the time of the BepiColombo mission definition (2005-06), only one spacecraft had approached the planet Mercury, NASA's Mariner 10, in the early 1970's. Mariner 10 was able to accomplish several fundamental observations but the collected data did not help in the evaluation of Mercury's radiation environment and therefore in the implementation of a specific radiation tolerance assessment. Mariner 10 was also the first mission making use of the flyby technique, based on ideas and calculations of Giuseppe Colombo (Fig. 1 - left). Flybys allowed the spacecraft to reach a resonant orbit with Mercury and to bend its trajectory to the level of Mercury's orbit.
Most recently, MESSENGER, a NASA mission presently in operation around Mercury, and BepiColombo use the flyby technique to reach and then orbit the planet.

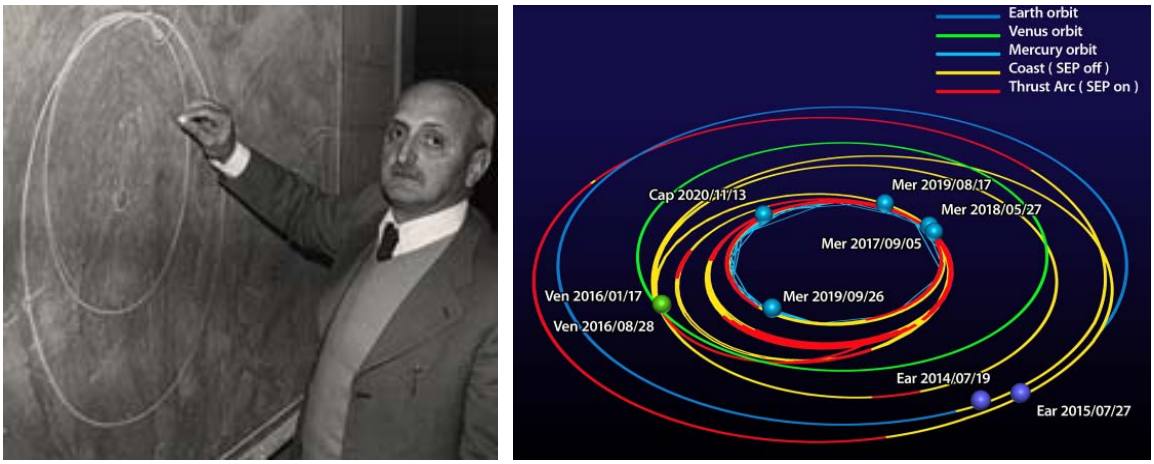

Fig. 1 – Left, Giuseppe Colombo (nicknamed Bepi) after who BepiColombo mission is named. Right, schematic of BepiColombo's 6.5 years cruise inwards the inner solar system towards Mercury (*image: BepiColombo/ESA & JAXA*). It can be seen as most of the cruise is spent at orbits much lower than 1 astronomical unit (AU).

If the flyby technique is effective to bring a spacecraft in orbit around Mercury, it on the other hand requires the spacecraft to spend many years in the inner solar system at orbits between those of Venus and Mercury.
BepiColombo is scheduled for launch in 2015 and will spend 6.5 years on its journey to Mercury and up to 2 years in operation [1]. More than half of the cruise phase will take place at a distance from the Sun of about 0.5 astronomical unit (AU) with minimum distances as low as 0.3 AU (Fig.1 - Right). This proximity to the Sun poses a strict constraint on the radiation tolerance as described below.
This chapter starts with a description of the space radiation environment relevant for BepiColombo and the definition of the most representative experiment to assess the radiation tolerance for such a mission. Then a brief description of the facility used for the irradiation is presented. Thereafter two separated sections summarize the experiments and results for $LaBr_3$ and HPGe, respectively. A summary including a direct comparison of the two spectrometers closes the chapter.

2 Space radiation environment and its effects

2.1 Sources of radiation in space

For space applications, two main sources of radiation must be considered: Galactic Cosmic Rays (GCR) and Solar Energetic Particles (SEPs) [2,3].
GCRs are produced outside the solar system during supernova explosions. They consist primarily of protons and include a smaller population of alpha particles, heavier nuclei and electrons. Particle energies range from 0.1 to 10 GeV and their flux is approximately constant over time, modulated between 2 and 4 particle/cm^2/s, in anti-phase with the actual activity of the 11-year solar cycle. The corresponding average annual fluence is of the order of 10^8 particle/cm^2.
SEPs are produced both by solar flares and by Coronal Mass Ejections (CMEs). As for the GCRs, their primary constituent is protons, which is the reason why they are also commonly referred as Solar Proton Events (SPEs), term that will be used throughout this text. The energy distribution varies from event to event, but rarely exceeds 200 MeV [4,5] as seen in Fig. 2 where energy spectral distributions for several large SPEs are reported. Their occurrence is totally stochastic and, contrary to GCRs, modulated in phase with solar cycle.

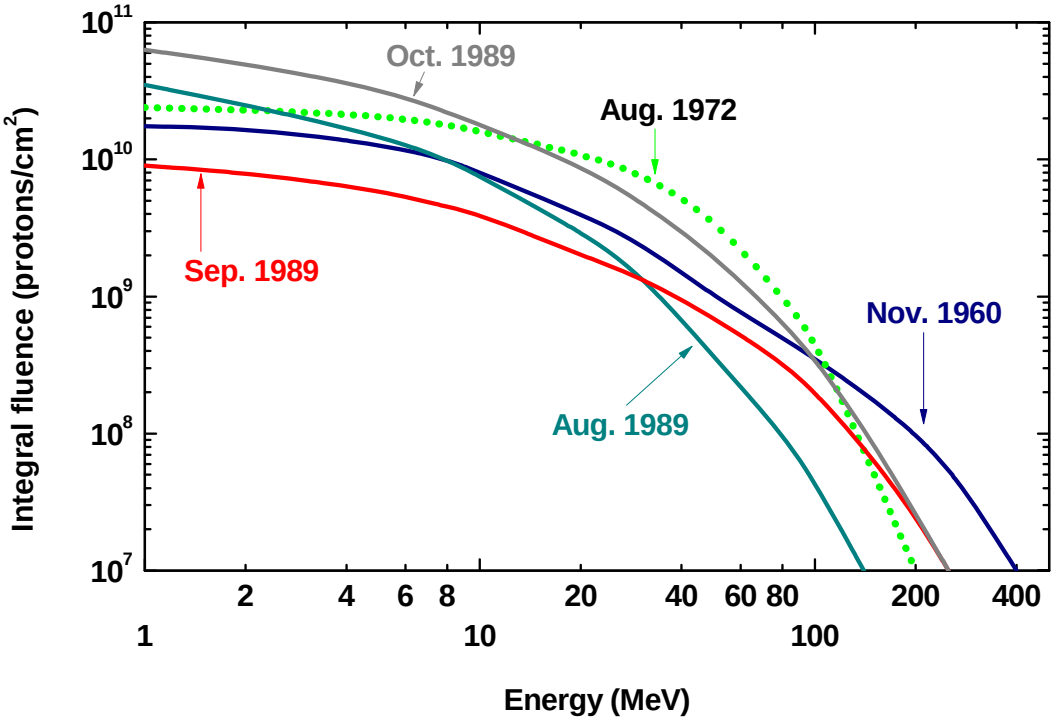

Fig. 2 – Energy distribution of several well known SPEs, adapted from [12]. Integral fluences are normalized at Earth's orbit, i.e. 1 AU from the Sun. It can be observed as the August 1972 event represents a good approximation of a typical SPE, a kind of average of the other events. For this reason in the present work the August 1972 event has been taken as reference for a standard event.

SPEs occur more frequently during the periods of intense solar activity. A typical event lasts from one to a few days and may include several hours of peak duration. There are extreme differences between single events in terms of the integrated fluence which can typically vary as much as 4 orders of magnitude from 10^5 to 10^9 protons/cm^2 at Earth's orbit, or 1 AU from the Sun [6]. The largest event ever observed, known as *Carrington event (1859)*, falls out of the previous range with an estimated integrated fluence of 2×10^{10} protons/cm^2 [7].
From the point of view of the radiation tolerance assessment, GCR contribution in terms of total dose is limited and, more importantly, predictable when compared to SPEs.
An example can be taken based on data from the Martian Radiation Environment Experiment (MARIE) instrument onboard the Mars Odyssey spacecraft [8,9]. Averaged over one year observation, April 2002 - April 2003, the instrument detected a GCR contribution to the radiation dose of 21.2 mrad/day with intermonth variations of only ±2 mrad/day [10,11]. During the same time period, the MARIE experiment detected also two small SPEs, in July 2002 and October 2002, of a total integrated fluence of about 3×10^7 proton/cm^2. In the month of occurrence, these events deposited a radiation dose of 150 mrad/day

and 90 mrad/day, respectively, that averaged over the year of observation accounted for another ~20 mrad/day in addition to the GCR dose.

2.2 Definition of a representative radiation environment for BepiColombo

Compared to the example above, for inner solar system missions, as for BepiColombo, the contribution of SPE has to be scaled to the actual position of the spacecraft in the inner part of the solar system. In fact SPEs originate at specific positions on the Sun's surface and then propagate outward towards the outer solar system. From the point of view of the propagation, events also differ from one another depending on the interplanetary magnetic field geometry and every event can be considered unique. A precise model describing event propagation does not exist. However, in the most conservative case, as proposed by Feynman et al. [5] and schematically depicted in Fig. 3, during the propagation the particle density decreases with the inverse of the square of the distance from the Sun. This means that a SPE at the orbit of Mercury would produces fluences about 10 times larger than at the orbit of the Earth, making any GCR contributions practically negligible, even in the case of the small, July 2002 and October 2002 SPEs, of MARIE. For this reason, the radiation tolerance assessment of BepiColombo concentrated exclusively on the effects due to SPEs.
Once established that SPEs are the most significant source of radiation damage for BepiColombo, the assessment proceeded by defining a SPE representative of an actual scenario. SPE energy spectra being quite variable from event to event, the so called August 1972 flare [12] was taken as the reference for the proton energy distribution as it is a good average within the known events as it can be seen in Fig. 2. For the August 1972 event, the integrated fluence was 5×10^9 protons/cm^2 for energy > 60 MeV [4]. Such an event, scaled using an inverse square of the distance proportionality at the orbit of Mercury, 0.4 AU, would correspond to an integrated fluence of $(1/0.4)^2 = 6.25$ times larger, i.e. of 3×10^{10} protons/cm^2.
The second step was then determining the probability of occurrence at Earth's orbit of a SPE of certain fluence for which the JPL model was used [5]. In this model, the occurrence probability of SPEs are categorized by integrated fluence above a certain energy threshold as reported in Table 1. For instance, the August 1972 event has ~12% annual probability to occur.

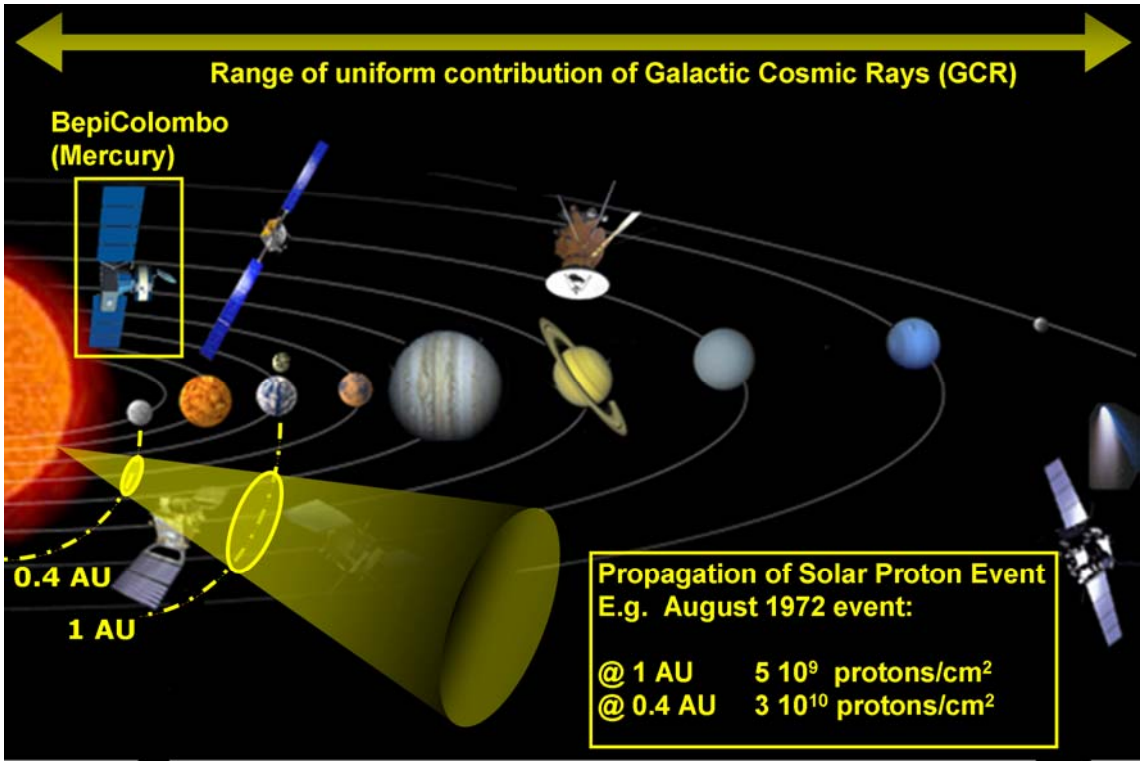

Fig. 3 – Representation of the model for inverse square distance scaling of SPE flux. *Solar system background image: ESA*.

Table 1 – Probability per annum that a solar proton event exceeds a specified fluence level at 1 AU. The data are based on the JPL-1991 model by Feynman et al., [5].

Fluence (proton/cm²)	**% Probability per annum of exceeding fluence at 1AU**			
	> 4 MeV	**> 10 MeV**	**> 30 MeV**	**> 60 MeV**
10^8	99	90	80	60
10^9	90	70	30	12
10^{10}	40	12	3	0.9
10^{11}	2	1	0.1	0.006

BepiColombo is scheduled for launch in 2015 and will spend 6.5 years on its journey to Mercury and up to 2 years in operation. Based on the previous statistics such a mission will certainly encounter one major SPE as large as August 1972 (with a probability of roughly the 12 × (6.5 + 2) = 102% and a radiation assessment must consider it, scaling the event fluence at Mercury orbit. The assessment of radiation tolerance then focused at irradiating the hardware to several reproduced August 1972 like SPEs with increasing fluence in order to observe what precise fluence could be assigned to a certain degree of damage.

2.3 Known radiation effects in gamma-ray spectrometers

Radiation damage is a complicated process which, in case of gamma-ray spectrometers, may involve not only the host crystal but also its impurities and defects. Radiation damage consists in an alteration of the operational and detection properties through interactions of radiation with the bulk material.
Apart from being the dominant constituent of GCRs and SPEs, protons present in general the largest interaction cross section. Neutrons resulting from intranuclear cascades in the detector or spacecraft systems can also contribute significantly, but usually at a level of only ~10% of that of the protons.
Examples of two HPGe gamma-ray spectrometers flown in space and exposed to radiation are reported by Kurczynsky et al. [13] and by Evans et al. [14] for the WIND and, again, Mars Odyssey missions respectively. Both missions operated at distances larger than 1 AU from the Sun (Mars orbit is at 1.5 AU).
For WIND, the GCRs were the main contributors to detector degradation since the mission did not encounter any severe SPE and the onboard spectrometer was exposed to the yearly fluence of 10^8 protons/cm^2 expected for GCRs. This exposure caused a degradation of energy resolution at ~1.35 MeV, from 3.6 keV to 8.6 keV during the first two years of operation and sensibly increasing thereafter. More importantly, the exposure caused a parallel 20% degradation in detection efficiency.
During its cruise (and before MARIE was put in operation), Mars Odyssey encountered another two SPEs (25 Sept. 2001 and 5 Nov. 2001) amounting to an integrated fluence of 8×10^8 protons/cm^2, which was ~80% of the total (SPE + GCR) fluence of 1×10^9 protons/cm^2 encountered by the spacecraft during its 11 months cruise [14]. Based on previous data one can deduce that the SPEs alone were responsible for the 5 times broadening of the energy resolution from 2.8 keV to 14 keV at ~1.35 MeV. For this mission no data have been reported on the instrument detection efficiency.
At the time of these experiments, there was no experimental data available on lanthanum halides and $LaBr_3$ in particular. In general, for inorganic scintillators, damage manifests itself as formation of colour centres and/or through dislocation of ions in the bulk material affecting the scintillation process.
The colour centres can interfere with the wavelength of the scintillation thereby reducing the light output and the energy resolution. The obvious physical manifestation of colour centre formation is cloudiness and/or colouration of the crystal. Elastic interactions of protons with the bulk material can form ion dislocations, and subsequent compensatory ion diffusions, acting as electron and hole traps and causing direct damaging to the scintillation mechanism through competing non-radiative processes. In the worse cases the luminescent centres may be rendered partially or even totally inoperable. Less severely, the traps can increase the afterglow (phosphorescence) of the crystal adding additional noise to the scintillation signal.

In general, noticeable effects are only apparent for absorbed doses of the order of at least 10 kGy (1 Mrad) and for this reason, scintillators are generally considered radiation tolerant when compared to other sensor materials such as semiconductors.

For both HPGe and $LaBr_3$, another potential problem is the proton induced activation. While all materials activate to some degree, the bulk material of gamma-ray detectors, to ensure high detection efficiency, is characterized by high atomic number Z which also increases proton activation cross sections and the propensity to activate. Activation increases the background counts in pulse height spectra with consequent decreasing of the instrument detection sensitivity.

3 The facility for irradiation experiments

3.1 The irradiation plan

The BepiColombo irradiation plan consisted of exposing the hardware to several irradiations with increasing fluence, all replicating the slope of the August 1972 SPE energy spectrum, and assessing the detectors performance in terms of energy resolution, detection efficiency and activation after each irradiation. The replication of the energy spectrum was achieved using 7 discrete proton energies with relative intensities tuned over the August 1972 SPE. Protons of 60 MeV are totally absorbed in 2 cm equivalent aluminium which typically corresponds to the self-shielding capability of a spacecraft. The minimum irradiation energy of 60 MeV was then set.
An integrated proton fluence of 8×10^8 protons/cm^2, as for Mars Odyssey, was chosen as the value for the first irradiation (for the $LaBr_3$ it was actually rounded to 10^9 protons/cm^2).
The maximum fluence was fixed to 6×10^{10} protons/cm^2 that corresponds to twice the fluence of an August 1972 like event scale at Mercury orbit. Again for the $LaBr_3$ the maximum fluence was rounded up to 10^{11} protons/cm^2. Moreover for a deeper understanding of radiation effects a fluence of 10^{12} protons/cm^2 was also used for $LaBr_3$.
Mote: a fluence of 6×10^{10} protons/cm^2 corresponds to a dose of ~100 krad (Gy) Si equivalent. Since the irradiations were characterized by the same energy spectrum, the dose scales proportionally with the fluence.

3.2 The irradiation beamline

To reproduce SPEs we used a proton beam of 191 MeV available at the AGOR superconducting cyclotron at the Kernfysisch Versneller Instituut (KVI), in Groningen, The Netherlands [15]. The first irradiations for both HPGe and $LaBr_3$ were carried out in the spring and summer of 2005.
A dual scatterfoil method [16] was used to expand and spatially linearize the narrow primary proton beam. A brass collimator provides well defined boundaries to the 10 cm wide irradiation field. The measured non-uniformity across this field was found to be less than 2% percent.
The irradiation target, HPGe or $LaBr_3$, could be positioned with millimetric accuracy inside the proton beam.

The incident particle flux (and fluence) on the detector was determined using a combination of three techniques – two absolute methods using scintillator detectors and activation measurements of aluminium foils along with a relative determination using a calibrated ion chamber. Combining the results from the three methods, the estimated precision in the flux and fluence determination is better than 10%.
A set of 6 degraders has been used to moderate the primary proton energy to replicate the spectrum of August 1972 event in 7 bins. Table 2 summarises the combination of degraders used to moderate the proton beam.
In Fig. 4 a panoramic picture of the irradiation beam line is shown together with its schematic drawing. The vacuum and air proton paths are also shown.

Table 2 – Proton energies, materials and their thicknesses and relative proton fluences used to simulate the August 1972 Solar Proton Event. In the last column the corresponding ranges in Ge.

Proton Energy (MeV)	**Degrader (thickness and material)**	**Relative fluence**	**Range in Ge (cm)**
184 ± 1	None	0.0074	6.7
160 ± 1	8 mm Cu	0.0150	5.3
140 ± 1	14 mm Cu	0.0304	4.2
120 ± 2	19 mm Cu + 3.5 mm polystyrene	0.0615	3.2
100 ± 2	24 mm Cu + 3.0 mm polystyrene	0.1240	2.4
80 ± 2	28 mm Cu + 4.5 mm polystyrene	0.2520	1.6
60 ± 2	32 mm Cu + 1.5 mm polystyrene	0.5100	1.0

A ~10 cm thick brass collimator was placed upstream the degraders to guarantee a uniform and well defined proton field, in our case of circular shape with a diameter of 8 cm. Protons stopping in the collimator produce secondary neutrons which can introduce extra damaging to the samples. Measurement and simulation carried out at the facility demonstrated that the total number of secondary neutrons incident at the detector constitutes only 1 % of the proton flux. Moreover, the secondary neutron contamination is more representative of an actual case scenario. In fact, the spacecraft is irradiated and activated by the protons as well, with consequent emission of secondary neutrons.

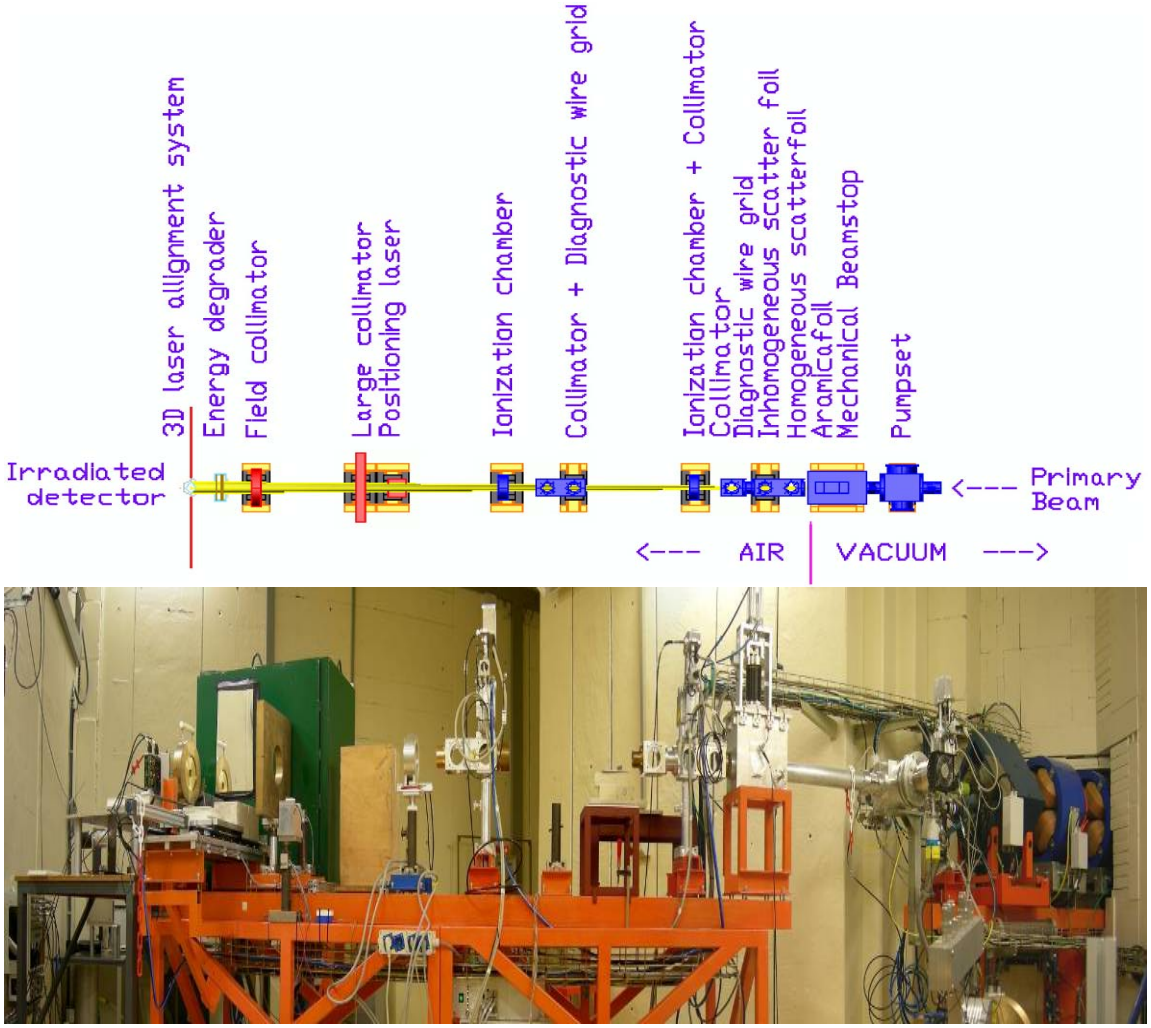

Fig 4 – Top: schematic drawing of the beam line used for the SPE irradiation. Bottom: panoramic picture of the beam line. Note that, roughly, the picture overlaps with the schematic.

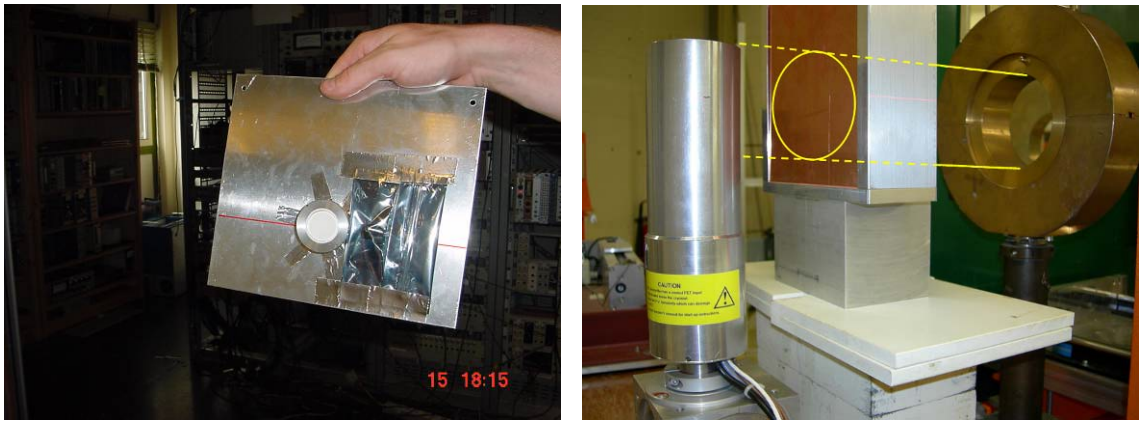

Fig 5 – Samples ready for proton irradiation. Left: a 1″×1″ $LaBr_3$. Right: a HPGe

4 Irradiations of $LaBr_3$ detectors

4.1 The first radiation assessment experiment

The $LaBr_3$ radiation tolerance assessment was carried out on a set of 5 packaged scintillator crystals produced by Saint Gobain Crystals and Detectors. The crystals were right circular cylinders of diameter 25.4 mm and length 25.4 mm, namely 1″×1″.

As usual for hygroscopic scintillators, the crystals were covered on all sides, except the read-out side, with reflective material and sealed in an aluminium container to prevent hydration. In order to extract the scintillation light a 30 mm diameter, 3 mm thick BK7 grade-A glass window was used, providing good optical performance over the UV to the near infrared wavelength region.

The scintillation light collection readout was provided by Photonis photomultiplier tubes (PMT) XP2060B with 10 dynode stages. Because of the high PMT gain, low voltage operation was necessary to avoid PMT saturation due to the very fast and bright scintillation light pulses of $LaBr_3$. This aspect is described in more details in Chapters 4 and 5. The optimum bias voltage was found to be around +700 V, providing, at 3 μs amplifier shaping time, energy resolutions of ~ 3% FWHM at 662 keV.

The pre-irradiation energy resolutions of all 5 crystals were assessed using a series of radioactive sources (^{241}Am, ^{137}Cs and ^{60}Co) placed coaxially in front of the detector. The results are summarized in Table 3. In addition, the uniformity of the response was assessed using a collimated ^{137}Cs source placed at various positions around the crystal. No variation was found within statistics.

The crystals were irradiated in July 2005. For the largest fluence about one hour was necessary to complete the irradiation.

Table 3 – Summary of pre-irradiation energy resolution measurement for all 5 crystals.

Detector	**HV bias**	**Energy (keV)**			
		60	662	1173	1332
Serial n.	**(V)**	**FWHM energy resolution %**			
J149	680	10.6	2.8	2.4	2.1
J150	680	12.0	3.3	2.8	2.4
J146	700	11.0	3.1	2.4	2.2
J148	700	10.6	3.0	2.3	2.2
J147	700	11.0	3.1	2.3	2.3

Various subcomponents of the packaging as reflective tape, optical window and an empty aluminium container were irradiated separately.
A total of 4 integrated fluences were set in one-order-of-magnitude increasing steps starting at 10^9 protons/cm^2 and then 10^{10}, 10^{11} and 10^{12} protons/cm^2. One of the 5 crystals was not irradiated and kept as a reference. The largest fluence probably overestimates even the worse case scenario as the spacecraft itself would likely not survive such a catastrophic event. Nevertheless that fluence gave a more solid overview of the evolution of the radiation effects with integrated fluence.
Compilations of ^{137}Cs and ^{60}Co spectra for each irradiation including the un-irradiated reference sample are shown in Fig. 6 and the results in terms of energy resolution are given in Table 4. All the spectra shown in Fig. 6 were taken 5 days after the irradiation with the exception of the one corresponding to the sample irradiated at the higher fluence of 10^{12} protons/cm^2 which was taken 16 days after the irradiation. Such elapsed times before collecting the spectra were necessary to guarantee a radiation safe handling.
Apart from the appearance of activation lines at the higher fluences, no obvious changes appear in the spectra for fluences up to 10^{11} protons/cm^2. At the fluence level of 10^{11} protons/cm^2 a very slight discolouration of the scintillator was noticeable, although there was no significant degradation of its energy resolution (Table 3 and Table 4).
However, the sample exposed to 10^{12} protons/cm^2 was clearly discoloured and its energy resolution had degraded by ~30% and the scintillation light output reduced by ~50%. However, it was also noted that the BK7 glass window sample irradiated to the same fluence had discoloured by the same amount as shown in Fig 7. A test in which the un-irradiated crystal was coupled to the PMT through the 10^{12} protons/cm^2 irradiated window reproduced the light output and energy resolution measured in the irradiated sample. We concluded that damage of the window was responsible for the observed degradation in energy resolution. The 10^{12} protons/cm^2 irradiated crystal was subsequently repackaged with a new window and the energy resolution and gain were found to be the same as the pre-irradiation values within statistics. Fig. 8 reports a close up of the ^{60}Co peaks measured before the irradiation, after the irradiation and after repackaging. In conclusion, no significant radiation damage to the light output could be observed in $LaBr_3$ up to a proton fluence of 10^{12} protons/cm^2.
At a later stage this conclusion was supported by the irradiation at 10^{12} protons/cm^2 of a brand new sample encapsulated using a radiation hard quartz window.

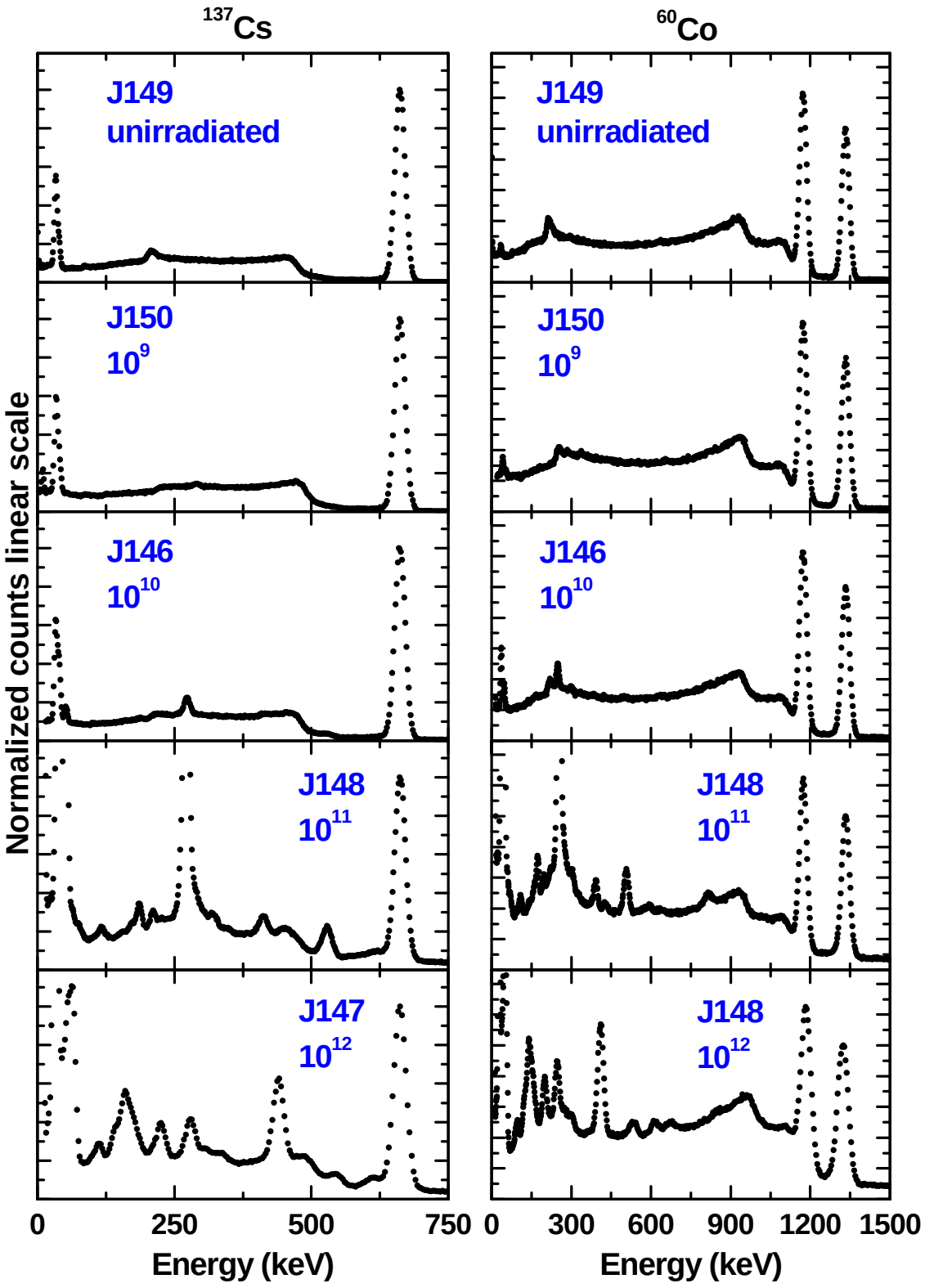

Fig. 6 – Compilation of ^{137}Cs and ^{60}Co spectra for all 5 crystals used for the radiation tolerance assessment, from top to bottom: unirradiated, 10^9, 10^{10}, 10^{11} and 10^{12} protons/cm^2. Spectra for the 10^{12} protons/cm^2 sample were taken 16 days after the irradiations, all the others 5 days after. The ordinates on the graphs have the same range.

Table 4. Summary of post-irradiation resolution measurements. The pre-irradiation values of Table 3 are shown in parenthesis. The absolute error on these measurements is estimated to be ± 0.2%.

Detector	**Fluence**	**Energy (keV)**			
		60	662	1173	1332
s/n	**(protons/cm²)**	**FWHM energy resolution %**			
J149	0	10.3 (10.6)	2.8 (2.8)	2.5 (2.4)	2.4 (2.1)
J150	10^{9}	12.1 (12.0)	3.0 (3.3)	2.9 (2.8)	2.5 (2.4)
J146	10^{10}	10.6 (11.0)	2.9 (3.1)	2.7 (2.4)	2.5 (2.2)
J148	10^{11}	11.5 (10.6)	3.1 (3.0)	2.6 (2.3)	2.6 (2.2)
J147	10^{12}	12.6 (11.0)	4.1 (3.1)	3.9 (2.3)	3.5 (2.3)
J147 repacked	10^{12}	11.2 (11.0)	3.2 (3.1)	2.3 (2.3)	2.4 (2.3)

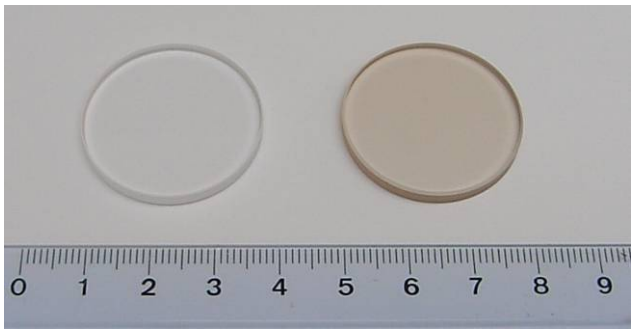

Fig. 7 – Effect of 10^{12} protons/cm² on the 3 mm thick BK7 grade A glass window used in the $LaBr_3$ crystal encapsulation.

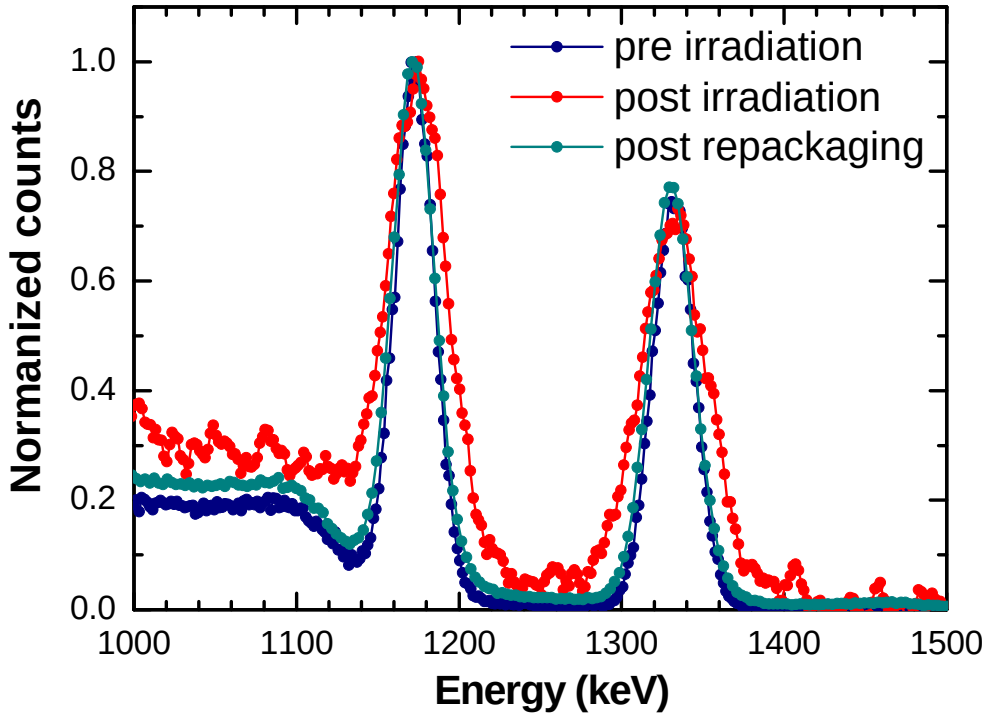

Fig. 8 – Compilation of ^{60}Co spectra collected with the sample irradiated at the largest fluence of 10^{12} protons/cm².

Analysis on proton induced activation was also carried out. For the 10^{10} and 10^{12} protons/cm^2 fluences it was possible to observe the decay of the activation starting from 18 hours after the irradiation. This was achieved collecting consecutive background spectra with the crystals coupled to the PMT. More correctly such a measurement refers to self activation. The results in term of integral counts in the energy range 250 keV 2 MeV are plotted in Fig. 9. The same fast decay with half live of 20 hours is observed with both samples.
Activation spectra for all samples are reported in Fig. 10, including the activity measured with the un-irradiated sample.
Integral activation in the energy range 20 keV – 3 MeV (the same range shown in Fig. 10) are reported in Table 5. Prior to irradiation, an intrinsic activity of 41.5±1.5 Bq was measured for all samples which includes contributions from ^{138}La, ^{40}K from the PMT and packaging and laboratory background. As more deeply investigated in Chapter 6, ^{138}La alone accounts for approximately 20 Bq for a 1″×1″ crystal, i.e. ~1.5 Bq/cm^3.

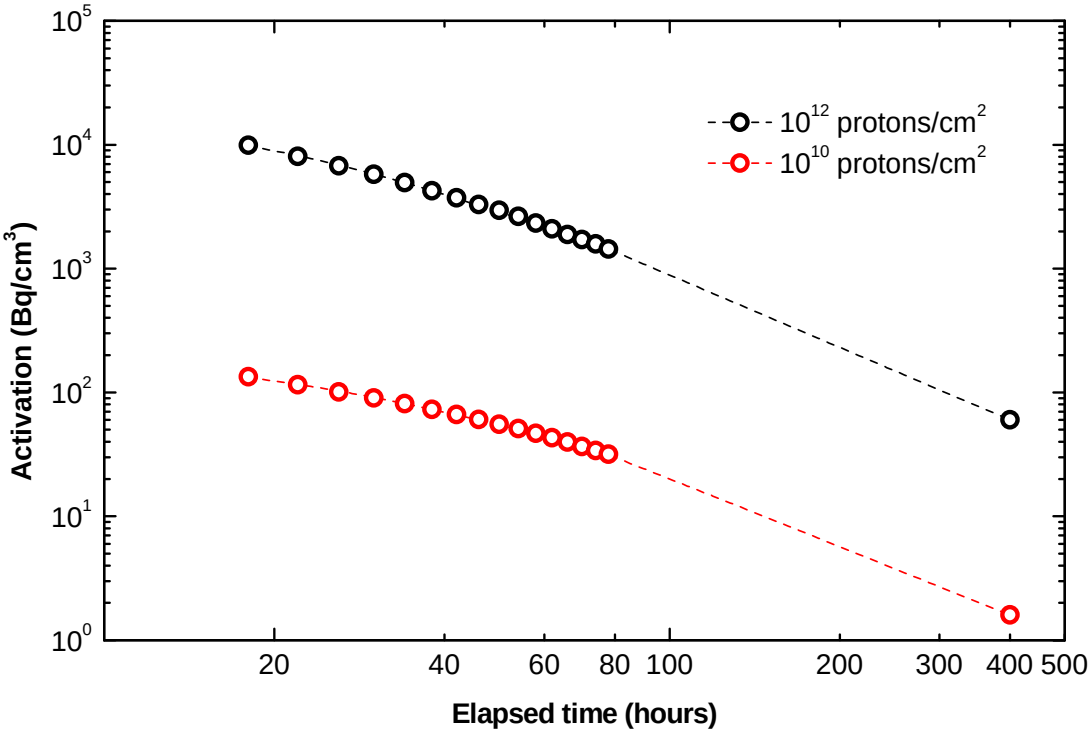

Fig. 9 – Activation decay of two $LaBr_3$ crystals irradiated with protons at fluences of 10^{10} and 10^{12} protons/cm^2. The activation is evaluated as the integral counts in the energy range 250 keV – 3 MeV. In such a range, 400 hours after the irradiation, the value observed with the sample irradiated to 10^{10} protons/cm^2 already matches the intrinsic activity due to ^{138}La.

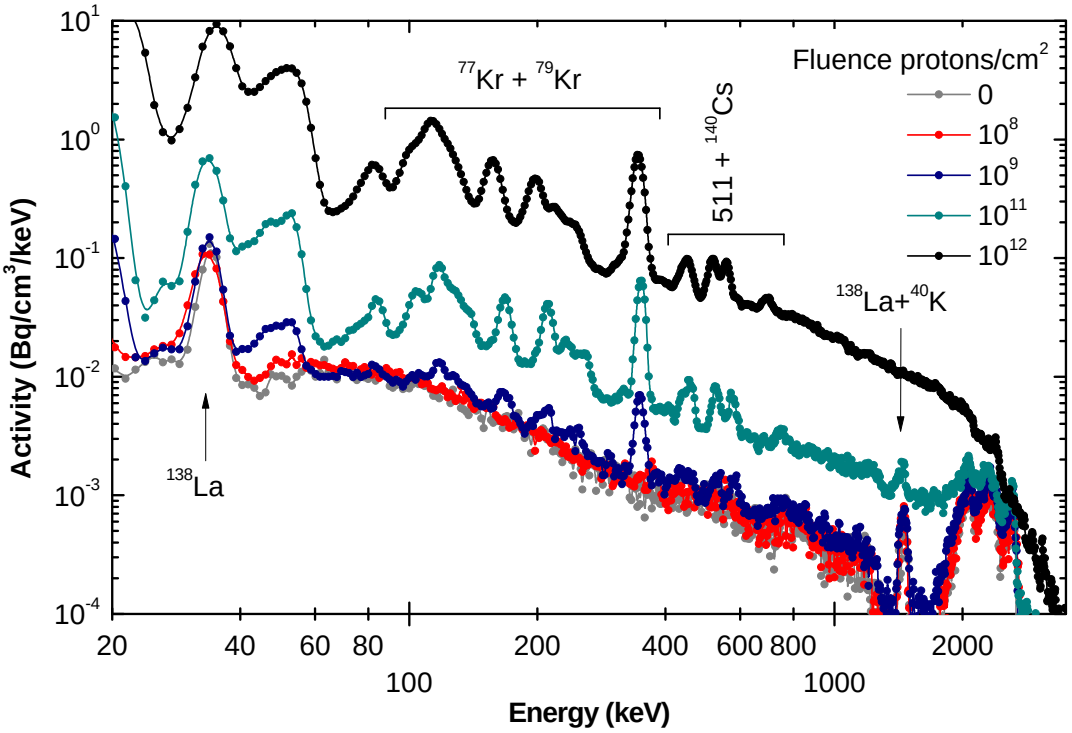

Fig. 10 – Proton activation of $LaBr_3$ samples 18 days after the irradiation.

Table 5. Summary of post-irradiation activation measurements 18 days after irradiation. For each of the 5 samples used, pre- and post-irradiation activation are reported. The net activation, i.e. the difference between the post-irradiation and the pre-irradiation activity, was found proportionally consistent to the actual proton fluence. Typical measurement error is ±5%.

Detector	**Fluence**	**Activity, energy range 20 keV - 3 Mev (Bq)**		
s/n	**(protons cm^{-2})**	Pre-irradiation	Post-irradiation	Net activation
J149	0	42.1	42.4	0.3
J150	10^9	40.7	42.7	2.0
J146	10^{10}	42.7	65.2	22.5
J148	10^{11}	42.4	281.5	239.1
J147	10^{12}	43.5	2312.1	2268.6

In order to investigate proton activation, more measurements were carried out using a standard gamma-ray spectroscopy setup for nuclide identification which consisted of an HPGe detector and a Pb castle. A notable result was that ^{79}Br and ^{81}Br, the two Br isotopes and lighter elements of $LaBr_3$, showed the largest contribution to the proton induced activation. Gamma-ray signatures of ^{77}Kr and ^{79}Kr dominate the intrinsic background of activated samples both produced by Br + p nuclear reactions, e.g. ^{79}Br(p,n)^{79}Kr. Other identified nuclides include ^{140}Cs and ^{139}Ce, both produced by ^{139}La + p nuclear reactions. More detailed results are available in [17,18] and are not further reported here. The ^{79}Kr half-life of 35 hours is consistent with the observed activation fast decay component discussed above.
At a later stage, experiments were repeated using crystals encapsulated with quartz window as well as bare crystals in order to verify the conclusions [19]. Also in these cases, no effects of light yield degradation could be observed after proton irradiation up to the fluence of 10^{12} proton/cm^2.

4.2 Irradiation of a 3″×3″ $LaBr_3$

The first $LaBr_3$ radiation tolerance assessment was done at the beginning of the R&D project when large volume crystals were not yet available. At the end of 2007, the experiment could be repeated using a large 3″×3″ crystal encapsulated using a radiation-hard quartz-window. For this irradiation a fluence of 10^{11} protons/cm^3 was chosen. It should be noted that because of the crystal size a larger absorbed dose is expected for the 3″×3″ compared to the smaller 1″×1″ used in the first assessment. Moreover, in order to uniformly distribute the radiation dose as in a real case scenario, the irradiation was carried out irradiating for 1/3 of the total fluence with the crystal rotating around its axis, for 1/3 the top side and for 1/3 the bottom side.
The new results substantially confirmed the earlier conclusions, however thanks to the experience gained, the minor effects of radiation damage could be observed as described below.
After irradiation a slight decrease in light output of about 10% was observed, which had no measurable effect on the energy resolution. Visually, the crystal did show a slightly darker colour than pre-irradiation. The crystal was then shipped to the factory for deeper inspections and possible encapsulation dismounting. Once at the factory, a further light output measurement showed a value consistent with the pre-irradiation value as the crystal had self recovered in the meantime. Shipped back to ESA/ESTEC, the recovery could be confirmed. In addition, the darkening observed initially had vanished.

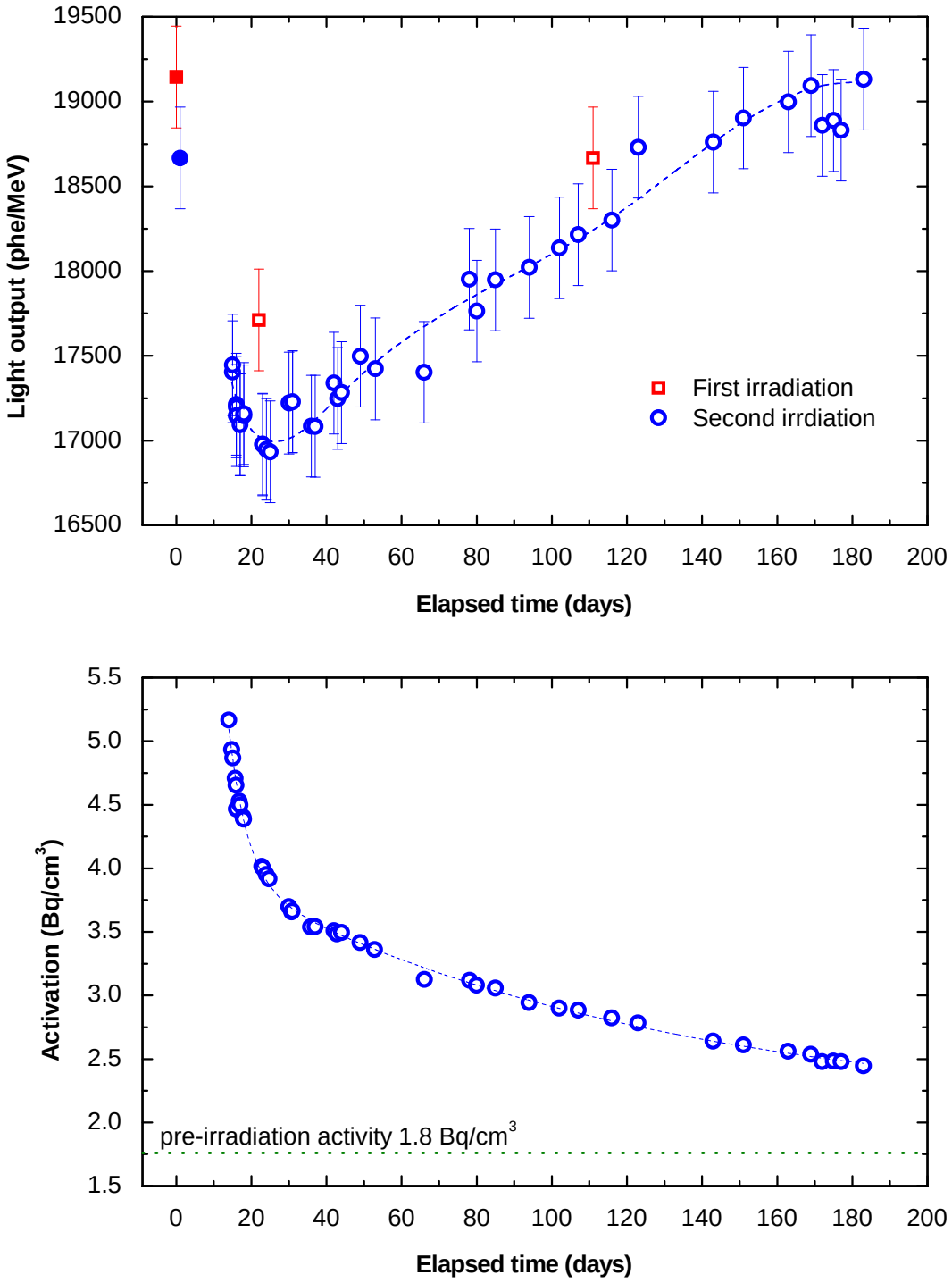

Fig. 11 – Top: light output restoration after deterioration of a 3″×3″ $LaBr_3$ twice irradiated with a fluence of 10^{11} protons/cm^3. Two decay times are found: a faster one of ~5 days (120 hours) and a longer one of ~100 days (2400 hours). The ~20 hours fast decay observed with the smaller crystal was not observed, because the measurement could only start 7 weeks after irradiation.

The irradiation was then repeated and the light output constantly monitored thereafter.
A dedicated setup was put in place for the light output measurement in order to minimize any systematic error. To optimize reproducibility the light output measurements were carried without using optical coupling between crystal and PMT. All the above ensured that the relative measurement error was within ±2%. In fact, fluctuations of < 1% were found in the peak position of the single photo-electron multiplication along the experiment duration, which was the main source of measurement error.
The result was that after an initial decrease following the second irradiation (and possibly to effects of the self irradiation due to activation) the light output of the crystal slowly restored it-self. The evolution of the light output and the activation decay are presented in Fig. 11. It can be seen that light output data available after the first irradiation consistently overlapped with the data of the second irradiation.
Since in space the spectrometer will be constantly recalibrated using well know gamma-ray lines such as the 511 keV annihilation line, the slow recovering does not pose any problem of misinterpretation.

4.3 Other radiation tolerance assessments

Experiments were carried out in TU Delft by irradiating $LaBr_3$ (and other scintillator crystals as $LaCl_3$ and $CeBr_3$) with gamma-rays using a high activity ^{60}Co source (Gammacell 220 Excel). A notable result was that in particular for $LaBr_3$ a kind of shock effect was observed following the most moderate dose which disproportionally affected the light yield and energy resolution. Full details are available from [20]. However, following the first experiment the results could not be reproduced, leaving doubt on their reliability. In addition a similar experiment was carried out independently by Normand et al. [21] showing for $LaBr_3$ a similar self recovering capability as the one observed with the 3″×3″ sample described in the previous section.
Further investigation up to doses of 1 Mrad (100 kGy) highlighted that the shock effect as well as the light output deterioration with increased cumulative dose was much more severe for a packed crystal than for a bare crystal. Full details are available in [22].
From the BepiColombo application point of view, the deterioration at 1 Mrad was not of real concern being a too high gamma-ray dose for a realistic case scenario. Of more concern was the shock effect for moderate doses. However the observed loss of light yield and energy resolution does not pose a serious treat to the spectrometer operation.

4.4 Summary of the $LaBr_3$ radiation tolerance assessment

The main conclusion of the radiation tolerance assessments is that $LaBr_3$ is suitable for a mission like BepiColombo. No signs of deterioration of scintillation performance could be detected following even the largest fluence of 10^{12} protons/cm^2. The only significant effect is due to the activation as discussed in Section 6, in parallel with the activation observed with HPGe.

5 Irradiations of HPGe detectors

For the radiation tolerance assessment three HPGe detectors have been used, all provided by Canberra, Lingolsheim. Table 6 summarizes the dimensions and pre-irradiation detection performances for the three detectors. The detectors are *closed-ended* coaxial high purity Ge detectors in the reverse electrode configuration, or n-type. For this kind of HPGe detector, negative high voltage bias is applied to the outer boron implanted p^+ contact, where holes are collected. A schematic of the detector is shown in Fig. 12. It has been demonstrated by Pehl et al. [23] that the reverse electrode configuration is more tolerant to radiation than the conventional p-type. Being developed for space applications, it is common to refer to them as space-born Ge detectors.

Table 6 – Properties of the three Ge detectors used in this study. Detector s/n 72079 has been irradiated with proton energies simulating the spectrum of August 1972 SPE. Detector 73423 has been just annealed while detector s/n 7481 has been irradiated with 55 MeV protons in two different positions.

	s/n 72079	**s/n 73423**	**s/n 7481**
Active Volume (cm^3)	110	53	71
Diameter (mm)	49	44	50
Length (mm)	67.5	35.9	38
Depletion bias (V)	-3000	-3000	-5000
Relative Efficiency at 1332 keV	17.2	11	16
FWHM at 1332 keV	2.0 (2.8)	1.8 (1.9)	2.0
Ratio FWTM/FWHM at 1332 keV	1.87	1.87	1.98
Ratio Peak to Compton at 1332 keV	42.9	41.4	40.5

Detector s/n 72079 was used for the most fundamental radiation tolerance experiment, the one reproducing the August 1972 SPE; detector s/n 7481 to observe the different effects of irradiating the detector while rotating around its axis and while keeping it at a fix position during the irradiation; and the third detector, s/n 73423, was simply annealed in order to observe the effect of the annealing alone on the detection performances.

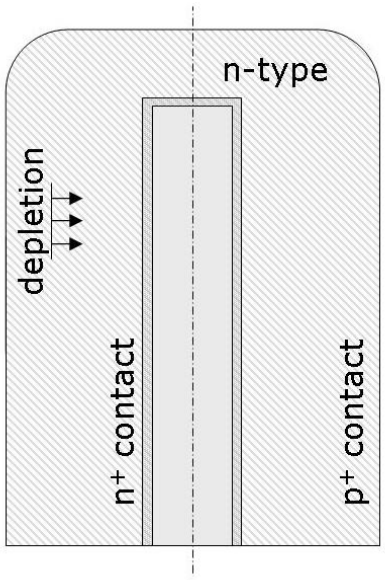

Fig. 12 – Schematic drawing of a spaceborne (reverse electrode) High Purity Ge detector. The inner n+ contact is obtained by Li diffusion while the external p+ contact by boron implantation. Right:

5.1 Irradiation simulating a Solar Proton Event and detector restoration

The first Ge detector (s/n 72079 in Table 6) has been irradiated three times with increasing fluences of 8×10^8 p/cm^2, 6×10^9 p/cm^2 and 6×10^{10} p/cm^2. To simulate the actual radiation environment in space the detector was rotating around its axis during the irradiation, as to uniformly expose its surface and volume.
During these and other irradiations specific care was taken in order to avoid irradiation of the Field Effect Transistor (FET) used as signal preamplifier and integrated in the detector assembly. This provided confidence that the observed radiation effect could totally be ascribed to the HPGe rather than to a deteriorated amplification. Also, since the FET preamplifier is a fundamental part for the performance of a HPGe spectrometer, several FET samples were irradiated separately. The result is that up to 10^{11} protons/cm^2 radiation effects on the FET can be neglected and only at 10^{12} protons/cm^2 the FET original characteristics deteriorated making the best achievable energy resolution about twice worse.
After each irradiation the detector was annealed at 100 °C to restore the detection performances within the operational values of 5 keV FWHM and 15% relative efficiency at 1332 keV (^{60}Co). We divided the annealing process into cycles, each one lasting 1 week.

The results of the irradiation and annealing tests are summarised in Table 7 and Fig. 13. We found a power law correlation with 0.6 exponent between the fluence and the required annealing time, *i.e.* the damage to be *annealed out*.
The first fluence, 8×10^8, was chosen to reproduce the damage observed for Mars Odyssey. We found a good agreement in the FWHM degradation observed by us and by Evans at al. [14], in both cases of about ~5 times broadened compared to pre-irradiation.
After the largest fluence irradiation (6×10^{10} p/cm^2), it took 14 weeks of annealing to restore the detector spectral performance within acceptable operational limits of FWHM < 5keV and efficiency > 85% of pre-irradiation values, *i.e.* > 15 % relative efficiency. After a further 11 weeks of annealing we eventually succeeded to fully restore the detector spectral performance as pre-irradiation values. This includes the recovering of the ratio FWTM/FWHM which was then 1.85 nearly as expected for a Gaussian shape (1.823), indicating that all residual hole traps were annealed out.

Table 7 – Irradiations simulating SPE and recovering phases. All values refer to the 1332 keV gamma-ray photons from a ^{60}Co source.

	FWHM (keV)	**Efficiency** (% of pre-irradiation)	**Ratio FWTM/FWHM**
Pre irradiation (March 2005)	2.5	100	1.9
1st Irradiation 8 × 10^8 p/cm² (1 May 2005)			
Post 8×10^8 p/cm² (May 2005)	11.2	100	2.4
1 week annealing (1st cycle) (May 2005)	2.7	100	1.9
2nd Irradiation 6 × 10^9 p/cm² (26 May 2005)			
Post 6×10^9 p/cm² (May 2005)	13.8	73	Undeter-minable
3 weeks annealing (2nd to 4th cycle) (May-July 2005)	5.0	100	2.2
3rd Irradiation 6 × 10^{10} p/cm² (16 July 2005)			
Post 6×10^{10} p/cm² (August 2005)	41.0	3.6	Undeter-minable
14 weeks annealing (5th to 18th cycle) (August 2005 - April 2007 ~2 years)	4.7	91.4	2.1
Restoration of operational limits (April 2007)			
11 weeks annealing (19th to 29th cycle) (May 2007 – February 2008)	2.3	93.3	1.9
Full recovery achieved (February 2008)			

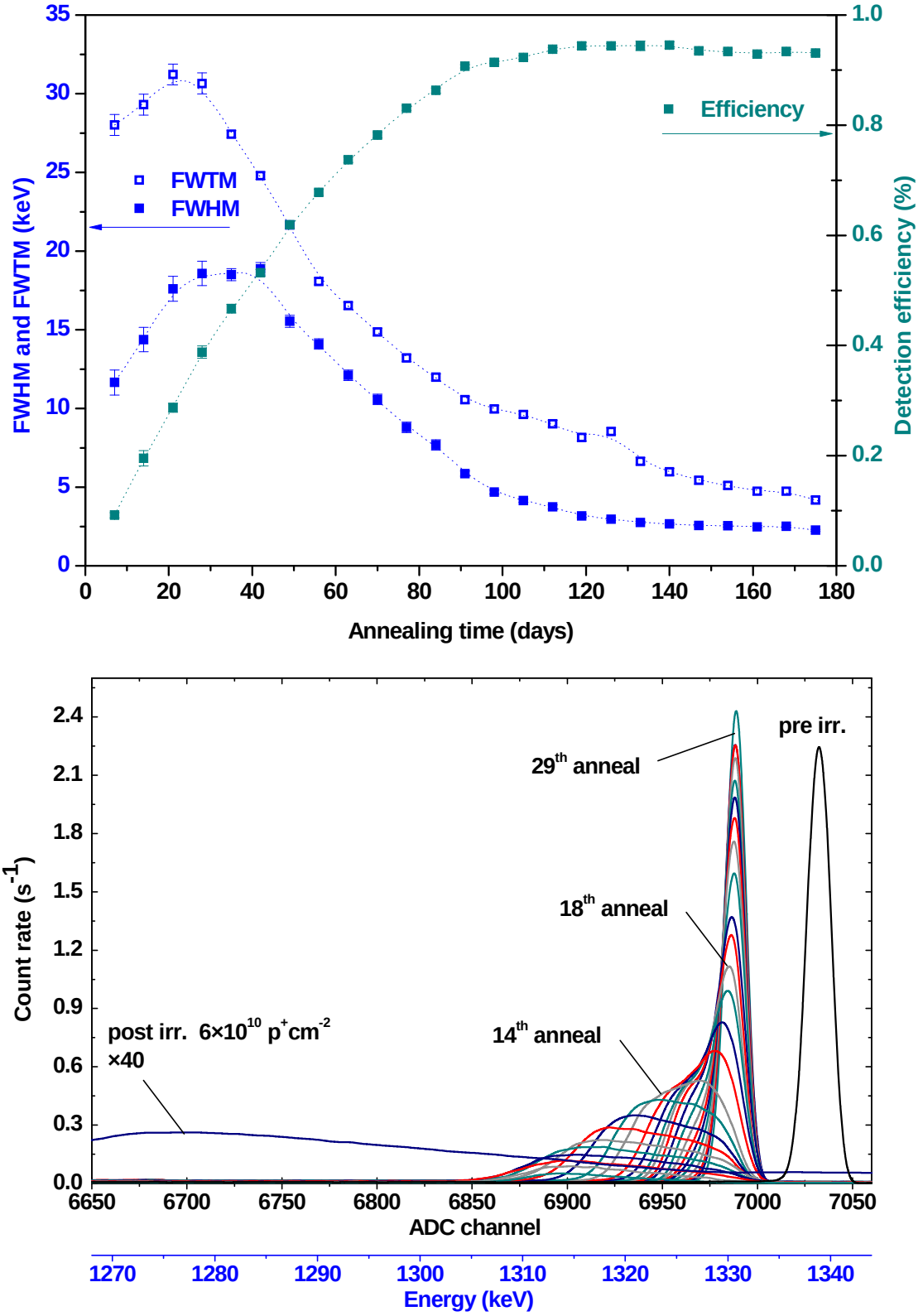

Fig. 13 – Recovery of the 1332 keV ^{60}Co gamma ray line with annealing cycles. Bottom: peak shape evolution from almost full damage to full recovering. The ^{60}Co gamma-ray at 1173 keV, which is out of the shown energy range, presents similar behaviour. Top: measured efficiency, FWHM and FWTM versus annealing time.

5.2 *Irradiation with fixed and rotating detector*

We investigated how the detection efficiency is affected for two different irradiation cases: with the detector rotating around its axis during the irradiation and with the detector kept in a fixed position, *i.e.* irradiating one side only. For this experiment we used detector s/n 7481, monoenergetic protons of 55 MeV and a total fluence of 2.4×10^{10} p/cm^2 for both irradiations. After each irradiation we tested detection performance with ^{109}Cd and ^{60}Co sources positioned above the detector's top face and at four perpendicular positions around its side: north (irradiated side) east, south and west. After the first irradiation (fixed position) and before the second (rotating), the detector was annealed until fully recovered.
Using the 1332.5 keV gamma-ray of ^{60}Co and the source positioned above the detector, we measured an efficiency degradation of ~70% relative of its pre-irradiation value for the fixed case, and ~35% for the rotating case. These values are reported in Table 8 together with those corresponding to the 88.06 kev gamma-ray of ^{109}Cd.

Table 8 – Effect on detection efficiency of to the two irradiations, detector fixed and detector rotating, at 88.06 keV (^{109}Cd) and at 1332.5 keV (^{60}Co).

	Detection efficiency %	
	^{109}Cd 88.06 keV	**^{60}Co 1332.5 keV**
Pre irradiation	100%	53
After 1st irradiation - fixed	57%	70%
After 2nd irradiation - rotating	44%	34%

For the side, the results for both ^{109}Cd and ^{60}Co sources are plotted in Fig. 14 showing for the fixed case that most of efficiency loss occurs in the irradiated side. The energy resolution at 1332.5 keV showed a similar behaviour being more affected in the irradiated side. These results are in agreement with the observations of Pirard et al [24].
Because of the nature of their propagation, SPE are essentially isotropic at the spacecraft. Therefore, the rotating case is the most representative and it must be specifically considered to avoid an underestimation of the damage.

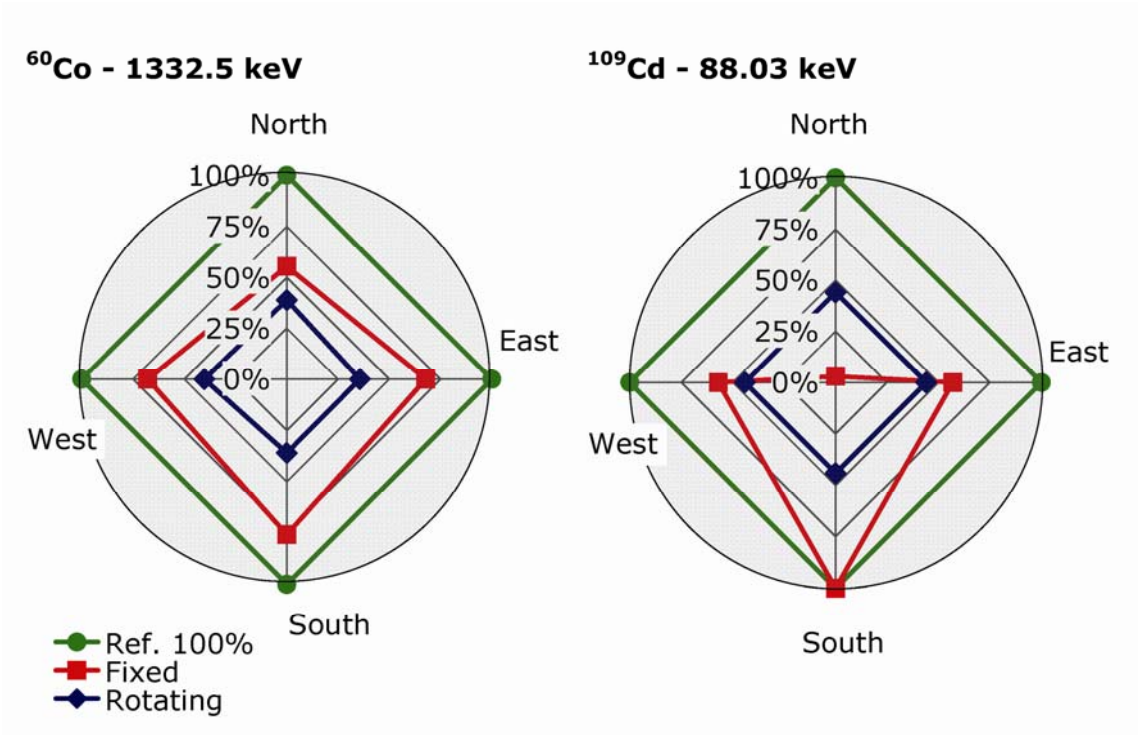

Fig. 14 – Comparison of the damaging subsequent to two different irradiations: keeping the detector in a fixed position relative to the beam and rotating the detector around its axis, as for the SPE simulation.

5.3 Annealing effects

Because of the long annealing time required for restoration we carried out a separate experiment consisting of annealing an undamaged detector (s/n 73423 in Table 6). We found that a slight loss of efficiency is produced after every annealing cycle. The explanation is that the lithium inner contact diffuses into the crystal during annealing, thereby reducing the depletion volume. After 10 weeks of annealing the initial efficiency at 1332 keV was reduced by a 15% and by 20% after a total 19 weeks. The rate of efficiency loss could be described by a model based on Fick's diffusion laws [25]. Obviously the magnitude of the effect depends on detector size nevertheless the efficiency loss due to annealing cycles can be predicted simply knowing the detector geometry.
All the above explains why, in spite of the full recovery achieved with detector s/n 72079 in term of FWHM and FWTM, a lack of efficiency is still present (Table 7 and Fig. 13).

5.4 Summary of the HPGe radiation tolerance assessment

Even if by means of annealing it has been possible to fully restore the spectral performance of Ge detector after proton irradiation replicating a SPE of integrated fluences up to 6×10^{10} protons/cm^2, the long annealing time required to restore the detection performances rises the question on the actual suitability of Ge detector for inner solar system missions, as BepiColombo.
The required annealing time to achieve the restoration of energy resolution, the ratio FWTM/FWTM and detection efficiency, to pre-irradiation values, is of the order of 25 weeks. However, about half of this time might be considered sufficient to restore the detector within acceptable operational limits for most applications. The probability of encountering one large SPE for a mission scheduled to cruise for 6.5 years and to operate for 2 years makes the required annealing time hardly feasible for the operational management of a mission such as BepiColombo.
An efficiency lack of 5% after full recovery has been observed and is caused by diffusion of the n^+ inner contact which reduced the active volume. We can conclude that severe radiation damage is reversible and non-permanent but it takes time of the order of months for the damage to be annealed out.

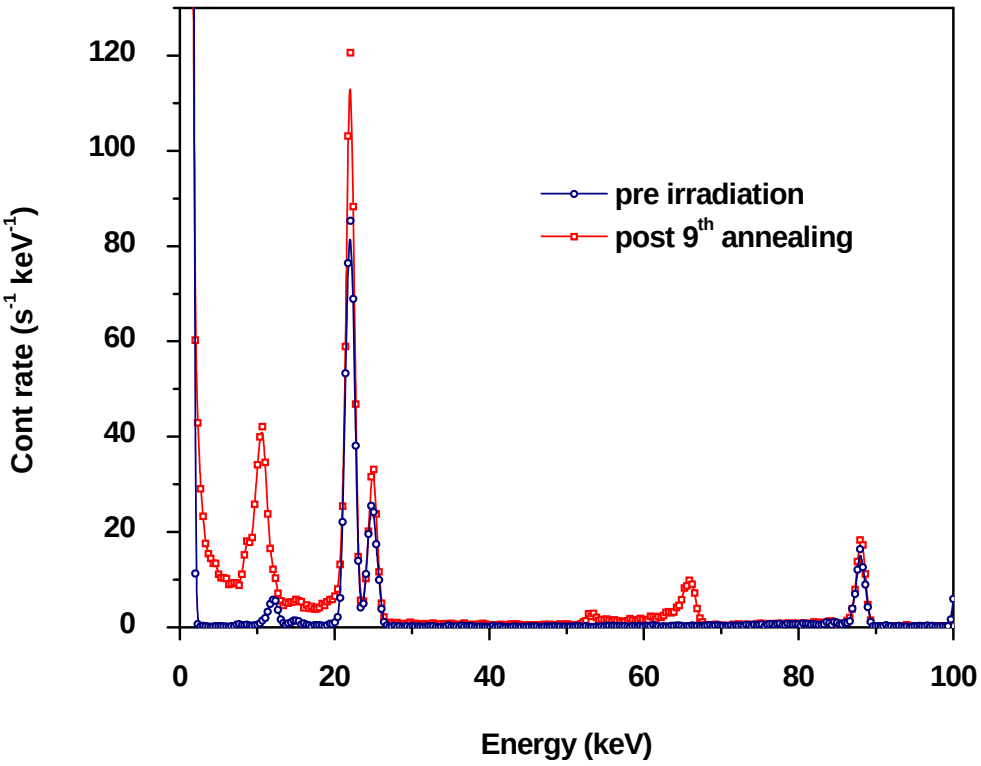

Fig. 15 – ^{109}Cd spectra collected pre-irradiation and after 5 weeks of annealing following the 6×10^{10} p/cm^2 SPE irradiation. The lines at 22 keV and 88 keV perfectly overlap indicating that the outer region of the detector is already recovered.

An efficiency loss subsequent to irradiation has been reported before by Kurczynsky et al [13] mainly caused by GCR. They explained the efficiency loss as a type inversion of the Ge crystal, from n- to p-type, as a consequence of the interaction of high energy protons (GeV). Traversing the crystal, these protons displace Ge atoms and cause disordered regions acting as acceptor defects (p-type). In our case, because of their lower energy, protons stop in the crystal forming interstitial hydrogen atoms. We can assume to be the same interstitial hydrogen atoms which act as donors and increase the crystal n-type concentration. In a Ge detector with reverse electrode configuration, an increased n-type concentration limits the depletion to a reduced volume close to the outer side. This is somewhat confirmed by the observation that recovery is faster for lower energy gamma-rays detection. For instance, after 5 annealing weeks the spectrum of a ^{109}Cd source is already full recovered (Fig 15).
With reference to Table 7, after the 8th annealing cycle a test was done to observe whether it would have been possible to compensate at least in part the efficiency loss using a stronger HV bias to deplete the crystal. Extrapolating the observations, the results show that even a HV bias of 7 kV is not enough to substantially increase the efficiency.

6 Discussion of the results

$LaBr_3$ has shown to be able to withstand very intense radiation from the Sun without significant deterioration besides activation. Even in the unlikely case of an extremely severe SPE, in principle, a $LaBr_3$ based gamma-ray spectrometer will still be able to accomplish scientific objectives.
A comparison of the activation for $LaBr_3$ and HPGe was carried out and results are plotted in Fig. 16. For reference, a data point corresponding to the irradiation of a CsI sample is also included. The evaluation of HPGe activation, especially for the highest fluence of 6×10^{10} protons/cm^2, is strongly affected by the severe, almost total, loss of efficiency caused by radiation damage. We could evaluate that at a time of approximately 18 days after irradiation the HPGe showed an activation of about 5 Bq/cm^3. At the time of this evaluation the efficiency loss at 1332 keV was more than 80%, roughly averaged in the energy range 100 keV to 2 MeV, meaning that the true activation would be about 25 Bq/cm^3. As seen in Fig. 16, this value matches the activation measured with $LaBr_3$, i.e 18.6 Bq/cm^3, allowing to conclude that no substantial difference in propensity to activate can be observed between HPGe and $LaBr_3$.

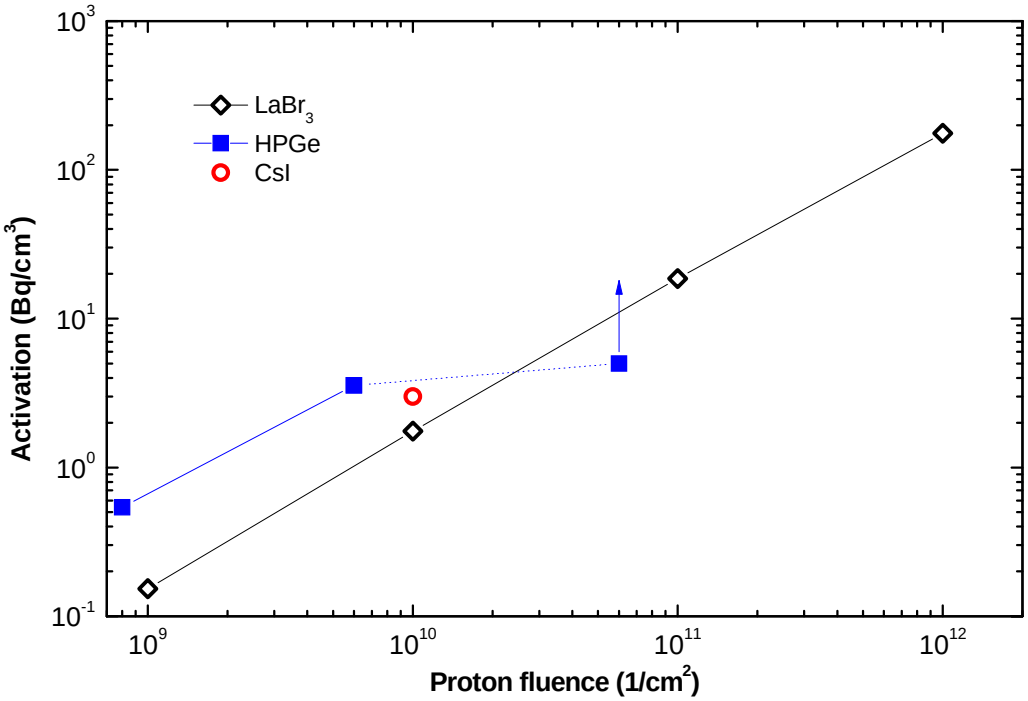

Fig. 16 – Activation yield (Bq/cm^3) of $LaBr_3$, HPGe and CsI(Tl) given for different irradiation fluences. Intrinsic pre-irradiation activities have been subtracted. The data were all taken 18 days (450 h) after irradiation. The Ge data point at 6×10^{10} protons/cm^2 is a lower limit since the efficiency of the detector had been seriously reduced by radiation damage.

Based on the work of Cooper and Chupp [26,27] a figure of merit (FoM) proportional to detection sensitivity of a gamma-ray spectrometer can be defined as:

$$FoM \propto \frac{\varepsilon(E)}{\sqrt{b(E) \times R(E)}} \tag{1}$$

where $\varepsilon(E)$ is the photopeak detection efficiency (full energy events), $b(E)$ the gamma-ray background, intrinsic and extrinsic, and $R(E)$ the energy resolution expressed in keV FWHM. All theabove quantities are energy dependent.
Using the results of the radiation assessments, it was possible to evaluate the FoM in the range 10 keV 10 MeV for both $LaBr_3$ and HPGe and directly compare their performances after a severe SPE. The evaluation is made using the results of the irradiation of the 3″x3″ $LaBr_3$ (10^{11} protons/cm^2) and of the HPGe the s/n 72079 after the irradiation at 6 x 10^{10} protons/cm^2 and after 4 weeks of annealing. This way the comparison refers to the detection sensitivity expected for the two gamma-ray spectrometers about 1 month after a severe SPE. Note that the comparison is carried out assuming the possibility to anneal the HPGe during that time at 100 °C.

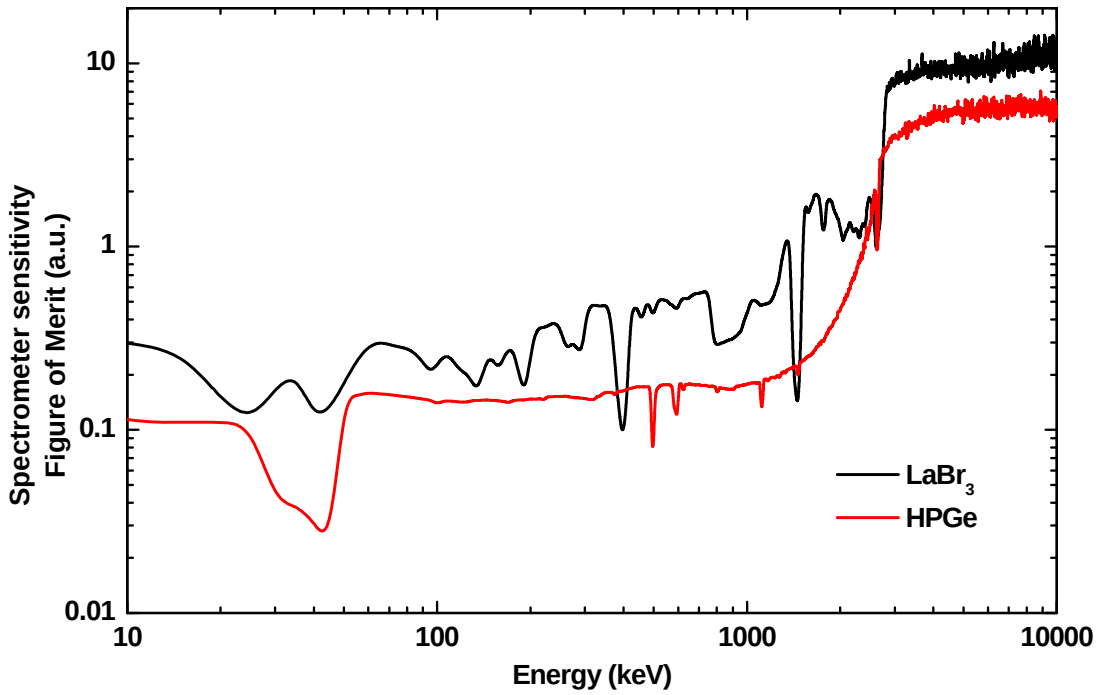

Fig. 17 – FoM, proportional to the spectrometer sensitivity 1 month after a severe SPE.

As seen in Fig. 17, where the FoM is plotted for both $LaBr_3$ and HPGe in the energy range 10 keV 10 MeV, after an SPE like August 1972 the sensitivity of an HPGe will be dramatically affected even after 4 weeks of annealing at 100 °C. On

the other hand $LaBr_3$ simply because of the natural decay of the activation will be again able to accomplishing scientific observation.
At the present time, the application of Ge detectors for inner solar system missions requires faster annealing and restoration cycles. Raising the annealing temperature with a specially designed crystal encapsulation is in principle feasible. Moreover it has been proposed to evaluate the capability of annealing by means of ultrasound. Similar technologies have been already applied to semiconductors [28,29] but not in the context of space exploration.
Following the radiation tolerance assessments, $LaBr_3$ was shown to be a solid choice for BepiColombo, carrying less risk compared to an HPGe.
Because of the above and because of the strict mass and power allocation for BepiColombo, the Mission Definition Board opted in favour of $LaBr_3$:Ce as the detection medium for the onboard gamma-ray spectrometer, which gave rise to the following research and study in support of the space applications of $LaBr_3$.

References

[1] J. Benkhoff et al., BepiColombo—Comprehensive exploration of Mercury: Mission overview and science goals, Planetary and Space Science, 58 (2010) 2.

http://dx.doi.org/10.1016/j.pss.2009.09.020

[2] Space Radiation Hazards and the Vision for Space Exploration, The National Academy Press, 2006, ISBN-10: 0-309-10264-2.

http://www.nap.edu/catalog/11760.html

[3] Radiation Design Handbook, European Space Agency, 1993, ISSN 0379-4059.

[4] D.F. Smart et al., Advances in Space Research, 37 (2006) 1734.

[5] J. Feynman et al., J. Geophys. Res., 98-A8 (1993) 13281.

and

J. Feynman et al., Journal of Atmospheric and Solar-Terrestrial Physics 64 (2002) 1679.

[6] D. Smart, M. Shea, A review of solar proton events during the 22nd solar cycle, Advances in Space Research, 30 (2002) pp. 1033.

[7] McCracken et al., "Solar cosmic ray events for the period 1561-1994. 1. Identification in polar ice, 1561-1950", J. Geophys. Res. 106 (2001) 21585.

doi:10.1029/2000JA000237

[8] C. Zeitlin et al., Overview of the Martian radiation environment experiment, Adv. Space Res., 33 (2004) 2204.

http://dx.doi.org/10.1016/S0273-1177(03)00514-3

[9] S. Saunders et al., 2001 Mars Odyssey Mission Summary, Space Sci. Rev., 110 (2004) 1.

DOI: 10.1023/B:SPAC.0000021006.84299.18

[10] P. Saganti et al., MARIE Measurements and Model Predictions of Solar Modulation of Galactic Cosmic Rays at Mars, in: Proceeding of the 29th ICRC, vol. 1, 2005, pp. 319.

NASA Technical Reports Server (NTRS) Document ID 20110011286

[11] C. Zeitlin et al., Mars Odyssey measurements of galactic cosmic rays and solar particles in Mars orbit, 2002–2008, Space Weather 8 (2010) S00E06.

doi:10.1029/2009SW000563, 2010

[12] Shielding Strategies for Human Space Exploration, NASA Conference Publication 3360, 1997.

[13] P. Kurczynski et al., Nucl. Instr. and Meth. A 431 (1999) 141.

[14] L.G. Evans et al., Charged-particle induced radiation damage of a HPGe gamma-ray detector during spaceflight Nucl. Instr. and Meth. A 422 (1999) 586.

http://dx.doi.org/10.1016/S0168-9002(98)00943-7

and

L.G. Evans et al., Background lines in the Mars Odyssey 2001 gamma-ray detector, Proc. of SPIE, 4784 (2002) 31.

http://dx.doi.org/10.1117/12.455976

[15] http://www.rug.nl/kvi

and

S. Brandenburg et at., AIP Conf. Proc. 600 (2001) 99.

[16] E. Grusell et al., A general solution to charged particle beam flattening using an optimized dual-scattering-foil technique, with application to proton therapy beams, Phys. Med. Biol., 39 (1994) 2201.

[17] E.-J. Buis, F. Quarati, S. Brandenburg, A.J.J. Bos, C. Dathy, P. Dorenbos, S. Kraft, E. Maddox, R. Ostendorf and A. Owens, Proton induced activation of $LaBr_3$:Ce and LaCl3:Ce, Nucl. Instr. and Meth. A 580 (2007) 902.

[18] E.-J. Buis, H. Beijers, S. Brandenburg, A.J.J. Bos, C. Dathy, P. Dorenbos, W. Drozdowski, S. Kraft, E. Maddox, R. Ostendorf, A. Owens and F. Quarati, Measurement and simulation of proton induced activation of $LaBr_3$:Ce, Nucl. Instr. and Meth. A 578 (2007) 239.

[19] W. Drozdowski, P. Dorenbos, A.J.J. Bos, J.T.M. de Haas, S. Kraft, E. Maddox, A. Owens, F.G.A. Quarati, C. Dathy and V.W. Ouspenski, Effect of proton dose, crystal size, and cerium concentration on scintillation yield and energy resolution of $LaBr_3$:Ce, IEEE Trans. Nucl. Sci. 54 (2007) 736.

[20] W. Drozdowski, P. Dorenbos, A.J.J. Bos, S. Kraft, E. Maddox, A. Owens, F.G.A. Quarati, C. Dathy and V.W. Ouspenski, Gamma-ray induced radiation damage in $LaBr_3$:5%Ce and LaCl 3:10%Ce scintillators, IEEE Trans. Nucl. Sci. 54 (2007) 1387.

[21] S. Normand et al., Resistance to gamma irradiation of $LaBr_3$:Ce and LaCl3:Ce single crystals, Nucl. Instr. and Meth. A 572 (2007) 754.

[22] W. Drozdowski, P. Dorenbos, A.J.J. Bos, A. Owens and F.G.A. Quarati, Gamma ray induced radiation damage in 1 in × 1 in $LaBr_3$:5 %Ce, Radiation Measurements, 43 (2008) 497.

[23] R.H. Pehl et. al., IEEE Trans. Nucl. Sci., NS-26 (1979) 321.

[24] B. Pirard et al., Nucl. Instr. and Meth., A 572 (2007) 698.

[25] A. Owens, S. Brandenburg, E-J. Buis, A.G. Kozorezov, S. Kraft, R.W. Ostendorf and F. Quarati, Effect of prolonged annealing on the performance of coaxial Ge gamma-ray detectors, JINST 2 (2007) P01001

[26] J.A. Cooper, "Factors Determining the Ultimate Sensitivity of Ge(Li) Gamma-Ray Spectrometers", Nucl Instr and Meth 82 (1970) 273.

[27] E.L. Chupp, "Gamma Ray Astronomy (Nuclear Transition Region)", D. Reidel Publishing Company, Dordrecht, Holland (1976).

[28] P. Brovetto, private communication.

[29] Ya. M. Olikh and N.I. Karas, Semiconductors, 30 (1996) 765.

Chapter 3

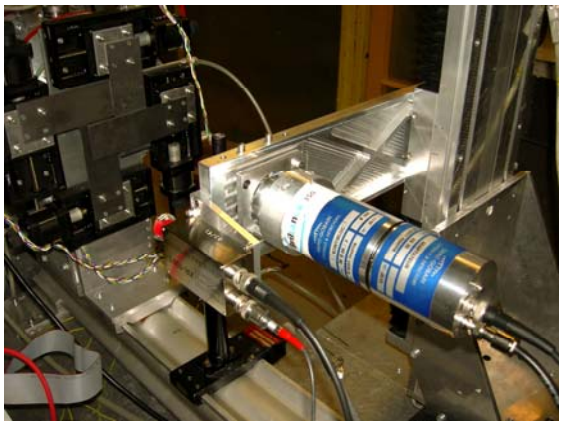

The X-ray response of $LaBr_3$

An established beamtime allocation at HASYLAB synchrotron radiation facility made it possible, in 2006, to carry out X-ray measurements on early grown 1″×1″ samples of $LaBr_3$ and $LaCl_3$ scintillators using a highly monochromatic pencil beams across the energy range 10.5 keV to 100 keV.

The response of $LaBr_3$ and $LaCl_3$ showed marked deviations from linearity, in particular at energies immediately above and below the K-shell binding energy of La (edge) at 39.8 keV, where the scintillators response changes steeply by 2% for $LaBr_3$ and by 3% for $LaCl_3$.

The energy resolution of $LaBr_3$ and $LaCl_3$ in the energy range below 100 keV is found inferior to that of a standard NaI(Tl), posing a limit on spectroscopic application of this two materials in this energy range, as, for instance, for the X-ray astronomy applications.

Because of the very low penetration depth of 100 keV photons in $LaBr_3$ and $LaCl_3$ (90% absorption occurs in few mm) it was not planned to repeat the measurements once larger volume samples became available. However, the technique used at HASYLAB opened new perspectives in the study of the non-proportionality of the response of scintillators. Extensive new experiments have been carried out by TU Delft on a wide number of compounds fucussing the research toward the improvement of scintillator response proportionality.

The content of this chapter is based on the following publication:

Owens, A., Bos, A.J.J., Brandenburg, S., Dorenbos, P., Drozdowski, W., Ostendorf, R.W., Quarati, F., Webb, A., Welter, E.
The hard X-ray response of Ce-doped lanthanum halide scintillators
Nucl. Instr. and Meth. A 574 (2007) 158

DOI: 10.1016/j.nima.2007.01.092

1 Introduction

The Ce doped lanthanum halide scintillators $LaBr_3$:Ce and $LaCl_3$:Ce present superior energy resolutions and proportionality of response when compared with traditional scintillating materials such as NaI:Tl. Both lanthanum halide scintillators have very fast light output decay (~20 ns) and high light yields of 60,000 and 50,000 ph/MeV (or of 165% and 80% compared to NaI) for $LaBr_3$ and $LaCl_3$ respectively. The chloride has a similar density as NaI at 3.8 g/cm^3, while the bromide has a density similar to Ge (5.1 g/cm^3). At gamma-ray energies, FWHM energy resolutions of 2.9% ($LaBr_3$) and 3.3% ($LaCl_3$) at 662 keV have been reported for very small crystals [1,2].
What is of interest here is the response at hard X-ray wavelengths – an energy range not usually exploited by scintillators, because of inherent non-linearities in their energy response, but potentially very interesting for synchrotron and differential X-ray absorbtiometry applications and for X-ray astronomy.

2 Experiments

The Cerium doped $LaCl_3$ and $LaBr_3$ crystals used were grown from melt by Saint Gobain Crystals and Detectors [3]. The cerium fraction was 10% for the chloride and 5% for the bromide. The ingots were processed into one inch high, one inch diameter, right circular cylinders (1″×1″) and packaged in hermetic aluminum housings to prevent hydration.
The scintillation read-out was obtained using a Photonis, XP2060B 10-stage photomultiplier tube (PMT), the same used for the radiation tolerance experiment on the 1″×1″ samples. As in that case, the problem of PMT gain saturation was avoided using a high voltage bias of 700V provided by a Canberra 3106D high voltage supply unit. The PMT assemblies also contain a unity gain preamplifier whose signal output is shaped and amplified by an external Ortec 671 spectroscopy amplifier. The output of the amplifier is digitized by an Amptek 8000A multichannel analyzer (MCA). An amplifier shaping time of 1 μs was chosen so as to give an optimum spectral resolution at 662 keV of 3.0% FWHM for $LaBr_3$ and 4.1% for $LaCl_3$ in the beamline environment.
The relative light yield ($LaBr_3$/$LaCl_3$) of the two crystals was determined at 22.1 keV, 32.2 keV and 60 keV using calibration sources to be ~1.75. This was achieved by coupling both crystals sequentially to the same PMT under identical

bias and operating conditions. Compared to $LaBr_3$, $LaCl_3$ scintillation emission is shifted of about 30 nm towards shorter wavelengths, and the value observed for relative light yield is affected by the photocathode quantum efficiency (QE) at that shorter wavelength.

2.1 X-ray detection experiments

X-ray detection experiments were carried out at the X-1 beamline at the Hamburger Synchrotronstrahlungslabor (HASYLAB) radiation facility in Hamburg, Germany [4]. This beamline is illustrated in Fig. 1. It utilizes a double Si crystal monochromator to produce highly monochromatic X-ray beams across the energy range 10.5 keV to 100 keV.
To achieve such a large energy range, a [511] Si crystal reflection was used, yielding an intrinsic energy resolution of ~1 eV at 10 keV rising to 20 eV at 100 keV. The beam spot size was set by a pair of precision stepper-driven slits, positioned immediately in front of the detector (see Fig. 1).
An ion chamber inserted between the monochromator and the exit slits controls the element of a servo loop to ensure constant beam intensity at the detector. The detector was mounted on an X-Y table capable of positioning the array to a precision of < 1 μm in each axis.
For the measurements described here the beam was normally incident at the center of the forward face of the detector. For the majority of the measurements, a slit size of 50 × 50 μm^2 was used. For completeness, additional full-area illumination measurements were carried out using radioactive sources.

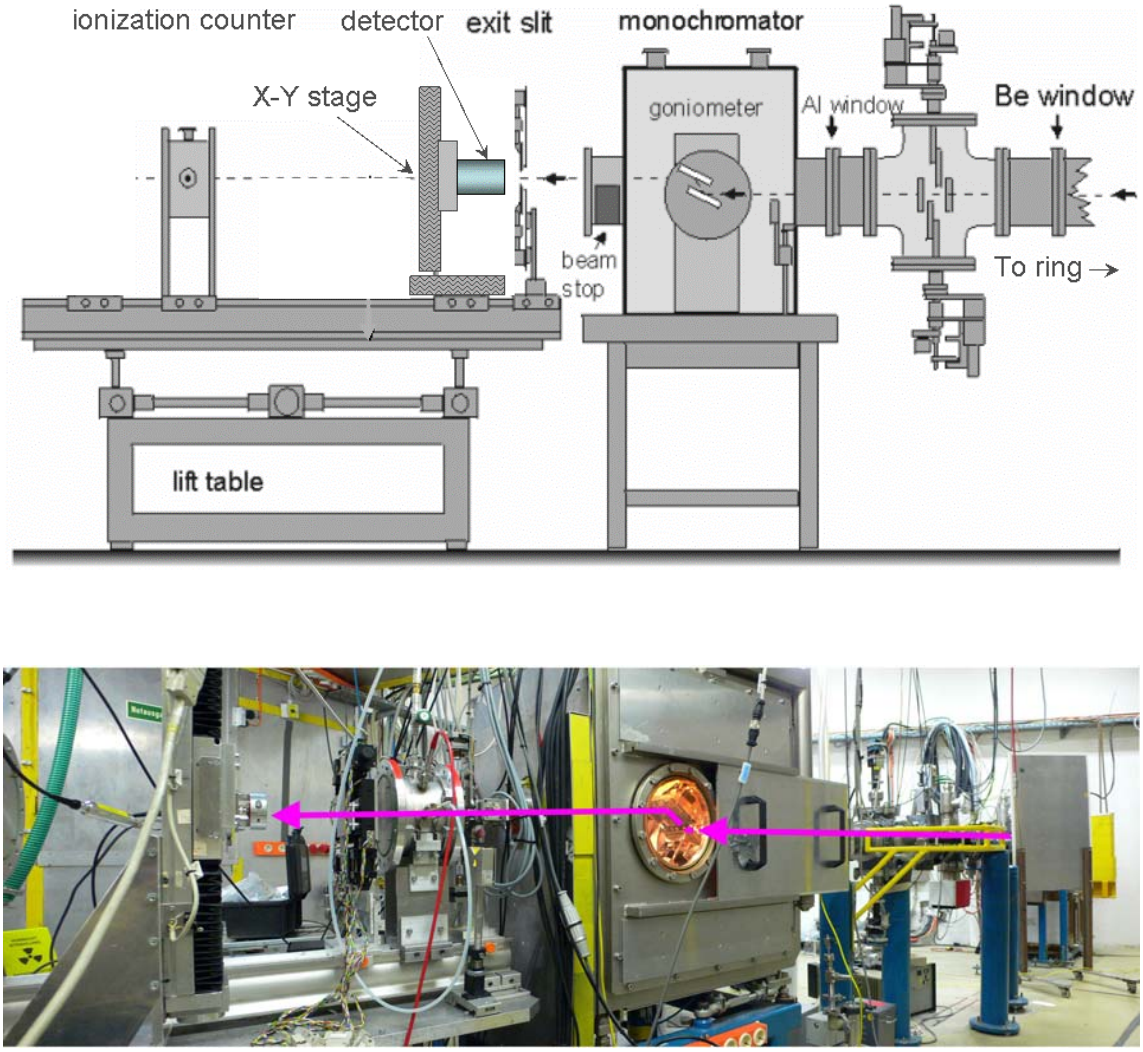

Fig. 1 - Experimental set-up at the HASYLAB X-1 beamline. Top: schematic. Bottom panoramic picture.

3 Results

The hard X-ray response of the detectors was determined using a number of monoenergetic energies between 10.5 keV and 100 keV. Fig. 2 shows a compilation of energy spectra measured for both the $LaBr_3$ and $LaCl_3$ detectors with 10 keV intervals. The measurements were carried out at room temperature. The noise threshold (defined as the energy for which the low energy noise attains an amplitude of 0.5 of the photopeak) is ~3 keV for both detectors.

The collected spectra are characterized by several features, besides their main photopeak. At an x-ray energy of 10.5 keV (the minimum energy used in this experiments) the monochromator 3rd harmonic (3×10.5 keV) is detected as indicated in Fig. 2 top inset for $LaCl_3$. Another features, also indicated in Fig. 2 top inset, is the detection of the peak caused by the escape of La fluorescence x-rays. Similar features are present in the $LaBr_3$ spectra as well. However, due to its higher density, the x-ray fluorescence escape probability is lower and the escape peaks are less pronounced compared to the main photopeak.

3.1 Proportionality of response

The response proportionality has been evaluated using the peak centroids of the spectra in Fig. 2. To accentuate deviations from linearity the response is plotted in the form of centroid divided by energy versus energy as shown in Fig. 3 for both the $LaCl_3$ and $LaBr_3$ crystals. The apparent larger output of the chloride is due to the amplifier gain used and does not reflect the actual light yield. For a perfectly linear system, this ratio should be constant with energy. As can be seen from Fig. 3, below the 38.9 keV of the La K-shell electron binding energy the non-linearity increases rapidly with a clear discontinuity at the edge. At the edge, the energy response changes by 2% for the bromide and 3% for the chloride. For the bromide there is also a discontinuity of 3.5% at the Br K-shell binding energy at 13.5 keV. The Cl K-shell binding energy (2.8 keV) falls out the energy range.
Fig. 4 shows the residuals for 2nd and 5th order polynomial fits of the detector response, i.e. energy to peak channel position calibration, for both $LaBr_3$ and $LaCl_3$. Residuals represent the percentage deviation from a best fit as:

$$Residuals = 100 \times \frac{Measured\ \ peak\ channel - Calculated\ \ peak\ channel}{Calculated\ \ peak\ channel} \quad (1)$$

For $LaBr_3$, we see that for the 2nd order polynomial fit, the residuals are quite deviant at energies below 15 keV. Increasing the order of the fit improves the situation - from a maximum deviation of 2.5% for the 2nd order fit down to 1.5% for the 5th order fit.
The corresponding root mean square (rms) deviations were 1.5% and 0.8%, respectively. However, the dominant deviations are found at the edge energy, reflecting the simplistic nature of the fitting functions.

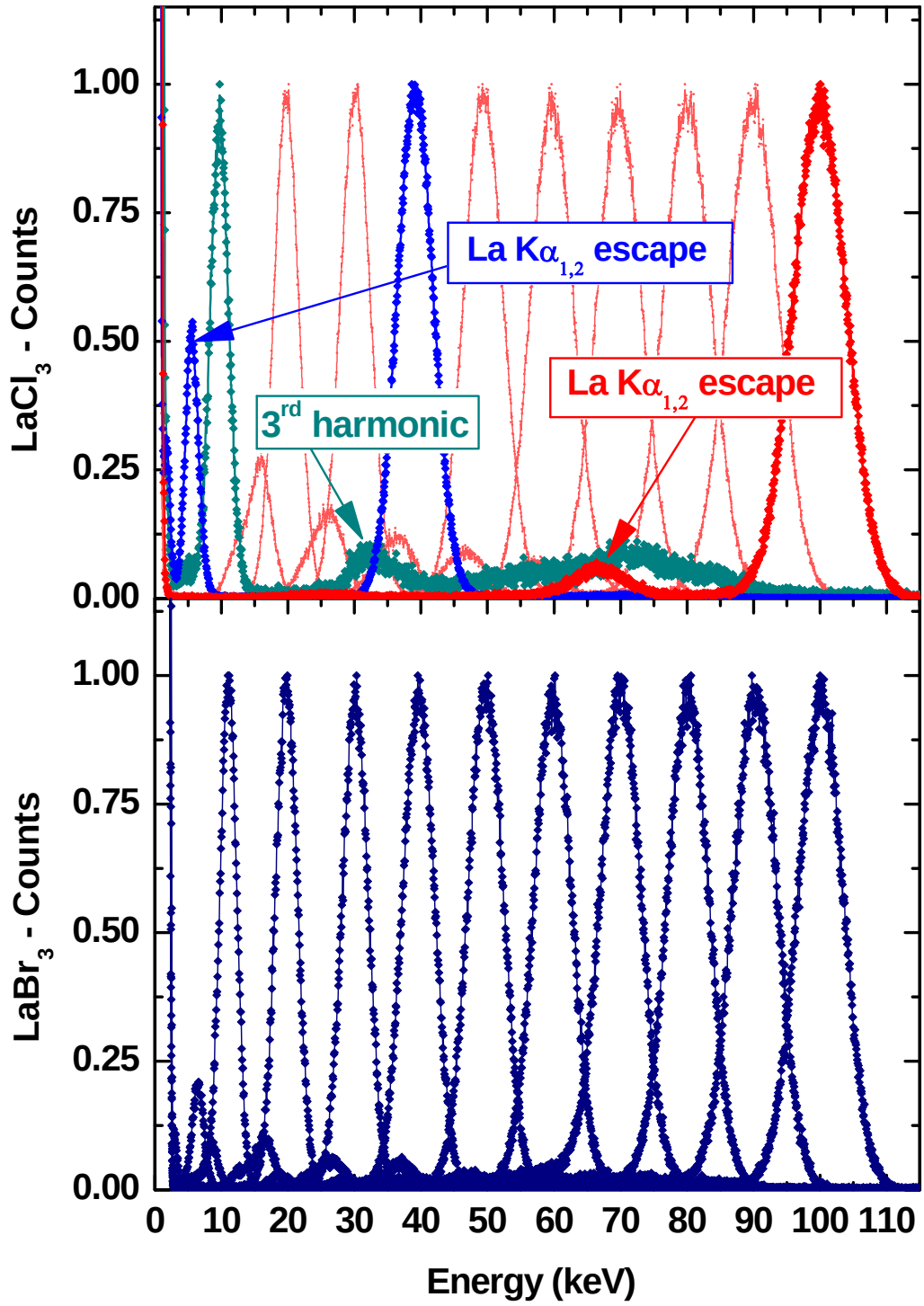

Fig. 2 - Composite of pulse height spectra measured with 10 keV intervals for the one inch $LaCl_3$ (top) and $LaBr_3$ (bottom) detectors. For $LaCl_3$ some spectral features are indicated. For example, the 10.5 keV spectrum is characterized by the presence of the monochromator 3rd harmonic falling just above 30 keV as indicated by the dark green arrow.

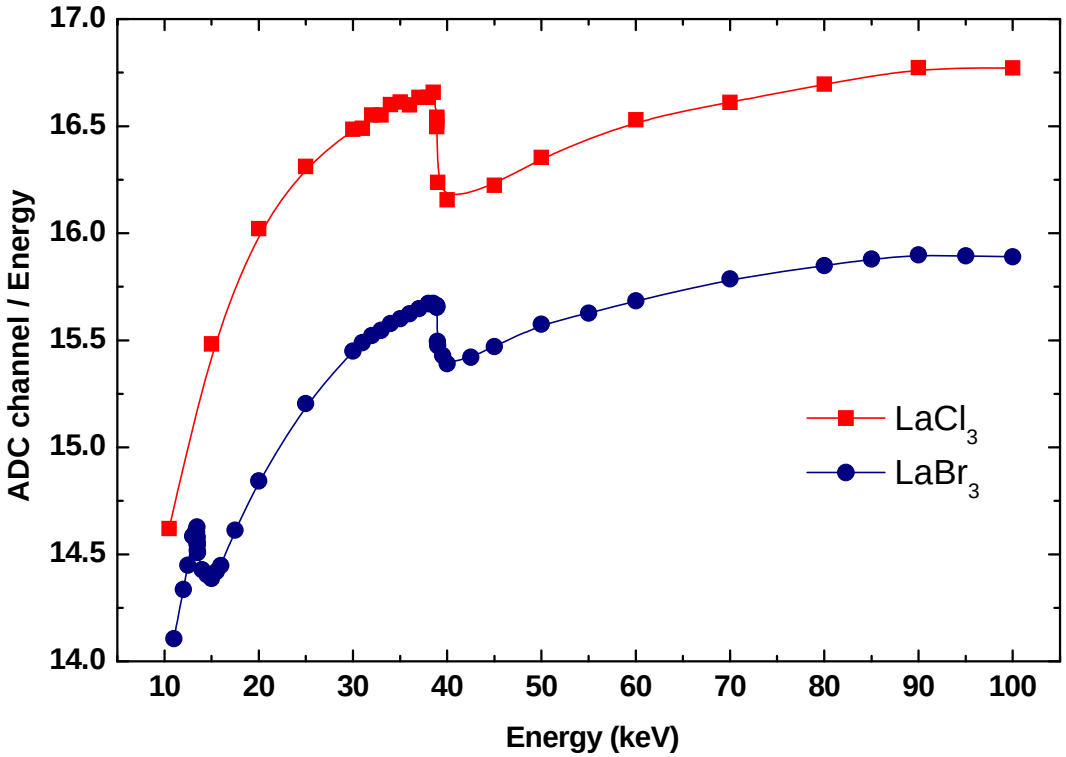

Fig. 3 - The detector proportionality of response or linearity curve for both the 1″×1″ $LaBr_3$ and $LaCl_3$ crystals.

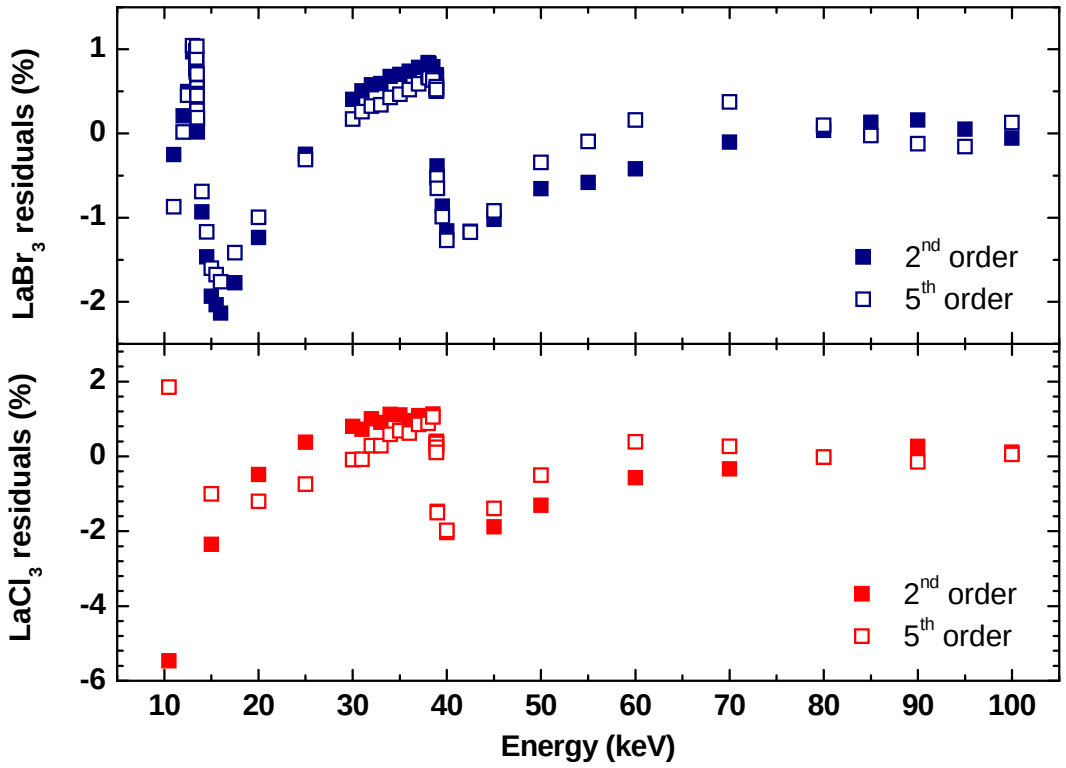

Fig. 4 –Residuals, as defined in Eq. (1), of 2nd and 5th order polynomial fits of the response of both $LaBr_3$ (top) and $LaCl_3$ (bottom).

3.2 Energy resolution

The energy resolutions were determined from the spectra in Fig. 2 and ranged from ~3 keV FWHM at 10.5 keV to ~8 keV FWHM at 100 keV as plotted in Fig. 5. As for the response proportionality, there is a clear discontinuity around the La K-edge at 38.9 keV for both $LaBr_3$ and $LaCl_3$ and a less pronounced deviation at Br K-edge (13.5 keV) for $LaBr_3$. Both above and below the edge (but above the Br edge for $LaBr_3$), the resolution data are well fit by power laws. In fact, the best fit for the curve above the edge includes the data point at 662 keV.
Also shown in Fig. 4 (top inset), it is the energy resolution for a 1″×1″ NaI crystal. The data were accumulated using the same PMT, although with a higher bias (750 V). NaI energy resolution is better than the halides below 100 keV and worse above. Similar observation was already reported in [5].
In the lower graph of Fig. 5, we show the ratio of the measured energy resolutions of $LaBr_3$ and $LaCl_3$. The ratio continues to fall slowly at higher energies. For example at 662 keV it is 0.77.

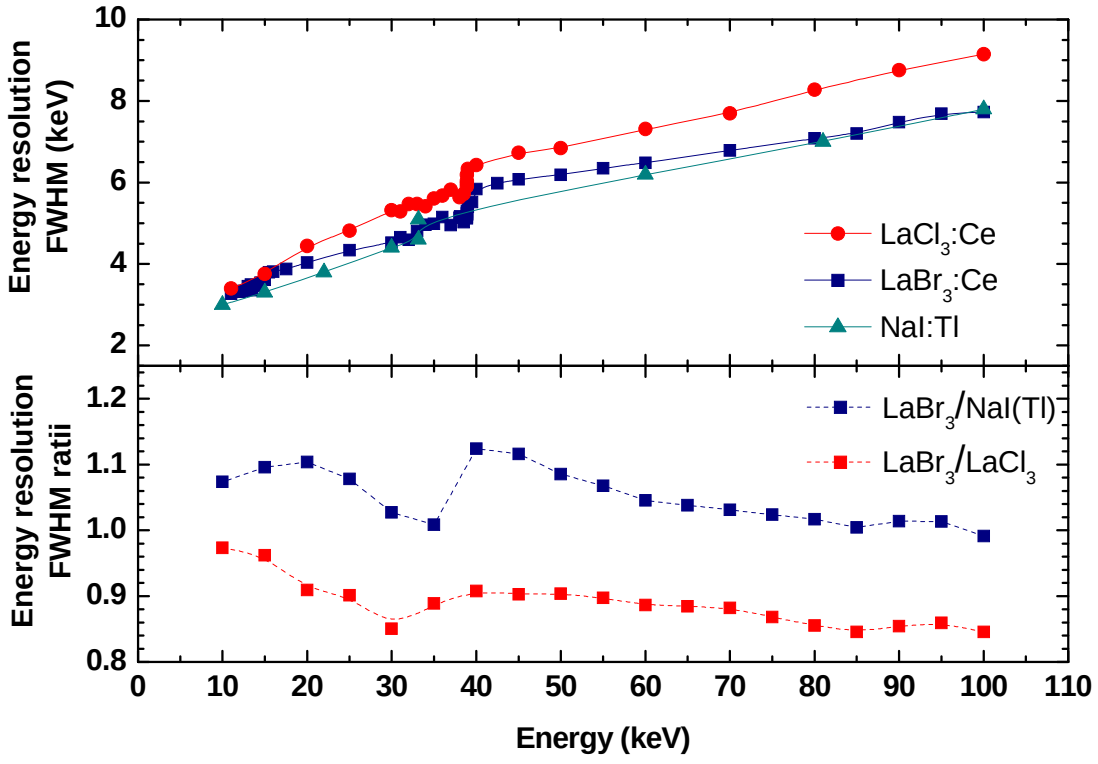

Fig. 4 – Top: measured energy resolution for $LaBr_3$, $LaCl_3$ and NaI crystals. Bottom: the ratio of the measured energy resolutions $LaBr_3/LaCl_3$ and $LaBr_3$/NaI. The ratios continue to fall at higher energies.

4 Summary of results

At hard X-ray energies < 100 keV, the energy resolution of NaI is slightly better than that of $LaBr_3$ and substantially better than that of $LaCl_3$. Compared to NaI the halides could excel in applications where high scintillation speed can be exploited – such as synchrotron physics.
The limited spectroscopic performance of $LaBr_3$ and $LaCl_3$ at energies below 100 keV coupled with the high intrinsic activity produced in that range by radioactive decays of ^{138}La, discourage applications in X-ray astronomy. However lanthanum halides show great promise as new workhorses for gamma-ray spectroscopy.
The technique used for these experiments proved very effective for further studies of scintillator response and in particular, the tunable X-ray source available at HasyLab did provide the ideal facility for implementing a new technique to investigate the scintillator response to electron with energy down to ~ 100 eV [6].

References

[1] E.V.D. van Loef et al., "High-energy-resolution scintillator: Ce^{3+} activated $LaBr_3$", Appl. Phys. Lett., 79 (2001) 1573.

[2] E.V.D. van Loef et al., "High-energy-resolution scintillator: Ce^{3+} activated $LaCl_3$", Appl. Phys. Lett., 77 (2000) 1467.

[3] http://www.detectors.saint-gobain.com/

[4] http://www-hasylab.desy.de/

[5] P. Dorenbos et al., "Gamma ray spectroscopy with a Ø19×19 mm^3 $LaBr_3$:0.5% Ce^{3+} Scintillator", IEEE Trans. Nucl. Sci., 51 (2004) 1289.

[6] I. V. Khodyuk et al., "Nonproportional scintillation response of NaI:Tl to low energy x-ray photons and electrons", J. Appl. Phys. 107(2010) 113513

Chapter 4

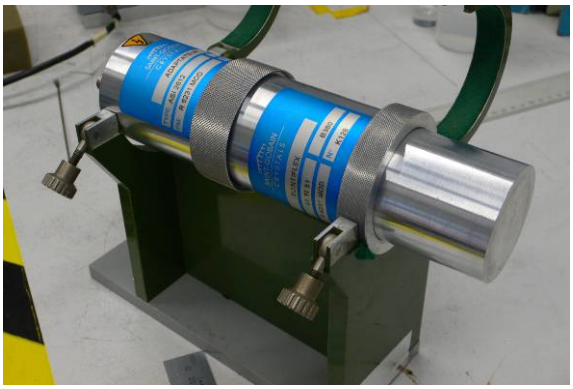

X- and gamma-ray response of a 2″×2″ $LaBr_3$:Ce scintillator detector

In the middle of 2006, advances in material growth techniques made 2″×2″ $LaBr_3$:Ce crystals available and in ESA we started assessing their suitability for use as remote sensing gamma-ray spectrometers. The main interest was observing whether or not the superior gamma-ray detection properties observed with small $LaBr_3$ crystals would scale to larger size samples without worsening.
Here the results are presented of an investigation of the response of a 2″×2″ $LaBr_3$:Ce crystal. The experiments were carried out using radioactive sources over the energy range 14 keV to 3220 keV. The work also presents a successful attempt to investigate the optimum PMT bias setting, in order to maximize scintillation collection without causing PMT gain saturation.
The response of the crystal was found to be largely linear over the upper 95% of the dynamic range and the larger deviations observed at lower energies can be attributed to the shortcomings of the PMT. Compared to smaller volume

crystals, no substantial degradation in light output, or alternately, in energy resolution was observed. For example, at 662 keV an energy resolution of 3.1% FWHM was measured.
Further on, using the AGOR cyclotron in Groningen, the same facility used for the radiation tolerance assessment experiments, the scintillator response to monoenergetic protons was characterized showing that protons create approximately half the light output of gamma-rays.

The content of this chapter is based on the following publication:

Quarati, F., Bos, A.J.J., Brandenburg, S., Dathy, C., Dorenbos, P., Kraft, S., Ostendorf, R.W., Ouspenski, V., Owens, A.
X-ray and gamma-ray response of a 2″×2″ $LaBr_3$:Ce scintillation detector
Nucl. Instr. and Meth. A 574 (2007) 115

DOI: 10.1016/j.nima.2007.01.161

1 Introduction

Since the beginning of the lanthanum halide development programme, considerable effort was spent on evaluating the effects of cerium doping and crystal growth techniques able to reproduce the superior performance for gamma-ray detection observed in small crystals [1,2]. In mid 2006, volumes of up to a few hundreds of cm^3 were grown with cerium concentration of 5%, which soon after became the standard Ce concentration for $LaBr_3$. From the largest grown ingots, it was possible to select and cut high quality material with volumes of 103 cm^3 (2″×2″).
Using both radioactive and synchrotron radiation sources, we measured the properties of $LaBr_3$ crystals of dimensions of 0.5″×0.5″, 1″×1″ and 1.5″×1.5″ as reported in Chapter 2 and 3 and [3,4]. In this chapter we report on new extensive measurements on a 2″×2″ crystal. In Table 1 we list the energy resolutions measured in our laboratory as crystal sizes have evolved, from which we observe that $LaBr_3$:Ce has not suffered a worsening of detection properties with increasing crystal size - from the early ~1 cm^3 detectors up to the present dimensions of ~100 cm^3.

Table 1 - The table shows the steps of large crystals implementation from the first processed crystal in 2001, up to 2″×2″ in 2006. Measurements have shown that the energy resolution of large crystals does not deteriorate compared to the smaller precursors.

Crystal size dia. × height (cm)	Volume (cm^3)	Volume increase factor	ΔE/E(%) at 662 keV
0.3 × 0.3 × 1.0	0.90	1.0	3.2 ± 0.2%
1.3 × 1.3	1.73	1.9	3.4 ± 0.2%
1.9 × 1.9	5.39	6.0	3.4 ± 0.2%
2.5 × 2.5	12.27	14	2.8 ± 0.2%
3.8 × 3.8	43.10	48	2.8 ± 0.2%
5.1 × 5.1	102.9	114	3.1± 0.2%

Fig. 1 - Photograph of a family of $LaBr_3$:Ce scintillator detectors. Crystal dimensions are, from right to left, 1″×1″, 1.5″×1.5″ and 2″×2″.

2 Experimental

The $LaBr_3$ crystal was grown by Saint Gobain Crystals and Detectors [5]. Experience with smaller crystals [1], has shown that the very high photon yield coupled with the fast photon emission times, makes light collection problematic using standard photomultiplier tubes (PMTs). Specifically, when biased at nominal voltages of ~ 1000 V, PMTs easily saturate, resulting in response non-proportionality and a reduced dynamic range. Lowering the bias, on the other hand, may extend the dynamic range, but at the expense of a deteriorated energy resolution. To partially overcome these limitations, the 2″×2″ scintillator detector discussed here uses a Hamamatsu R6231 PMT, which has a lower number of dynodes, 8 instead of the usual 10-12. A picture of the detector assembly is shown in Fig. 1.

Table 2 - X- and gamma-lines used in the present measurements, sorted by energy. The transition probability* and respective nuclide are also given.

γ line (keV)	Tran. Prob. (%)	Nuclide
14.14	52.2	^{88}Y
17.54	18.61	^{241}Am
22.1	83.6	^{109}Cd
26.34	2.40	^{241}Am
30.85	98.0	^{133}Ba
32.06	5.53	^{137}Cs
39.91	59.1	^{152}Eu
59.54	35.9	^{241}Am
70.11	61.0	^{203}Hg
81.00	34.06	^{133}Ba
83.0	2.83	^{203}Hg
88.03	3.63	^{109}Cd
121.78	28.58	^{152}Eu
122.06	85.60	^{57}Co
244.70	7.58	^{152}Eu
276.40	7.16	^{133}Ba
279.20	81.46	^{203}Hg
302.85	18.33	^{133}Ba
344.28	26.5	^{152}Eu
356.02	62.05	^{133}Ba
411.12	2.23	^{152}Eu
443.96	3.15	^{152}Eu
511.0	179.8	^{22}Na
661.66	85.00	^{137}Cs
778.90	12.94	^{152}Eu
834.84	99.98	^{54}Mn
867.37	4.25	^{152}Eu
898.04	94.0	^{88}Y
964.08	14.60	^{152}Eu
1173.2	99.85	^{60}Co
1274.5	99.94	^{22}Na
1332.5	99.98	^{60}Co
1408.0	21.00	^{152}Eu
1457.6	0.50	^{152}Eu
1836.1	99.33	^{88}Y
2505.7	Sum Peak	^{60}Co
2734	0.61	^{88}Y
3219.7	0.007	^{88}Y

*The transition probability for each mode of the primary decay expressed as percentages of the total number of the nuclear transformation of the relevant nuclide. Some references refer to the transition probably as emission probability or as intensity.

2.1 Measurements

Bias for the detector was provided by a Canberra 3001D high voltage supply. The PMT base also incorporates a unity gain preamplifier. The output of the preamplifier is amplified and shaped by a Tennelec TC244 shaping amplifier before being digitized by an 8000A Amptek multi-channel analyzer.
A set of calibrated radioactive sources were used to characterize the response of the detector at various X- and gamma-ray energies in the range 14.1 to 3219.7 keV. The complete list of the sources used together with their respective gamma-X-ray emission lines and relative intensities are reported in Table 2.
To accumulate the spectra, the sources were positioned 20 cm coaxially above the detector axis. The measurement acquisition times were set to have ~10^5 events in the main photo peaks. Examples of recorded spectra are shown in Fig. 2. In addition, the ^{152}Eu spectrum is shown in Fig.1 of Chapter 1. From the figures, it can be seen that virtually all the full energy peaks of the principal lines are resolved.

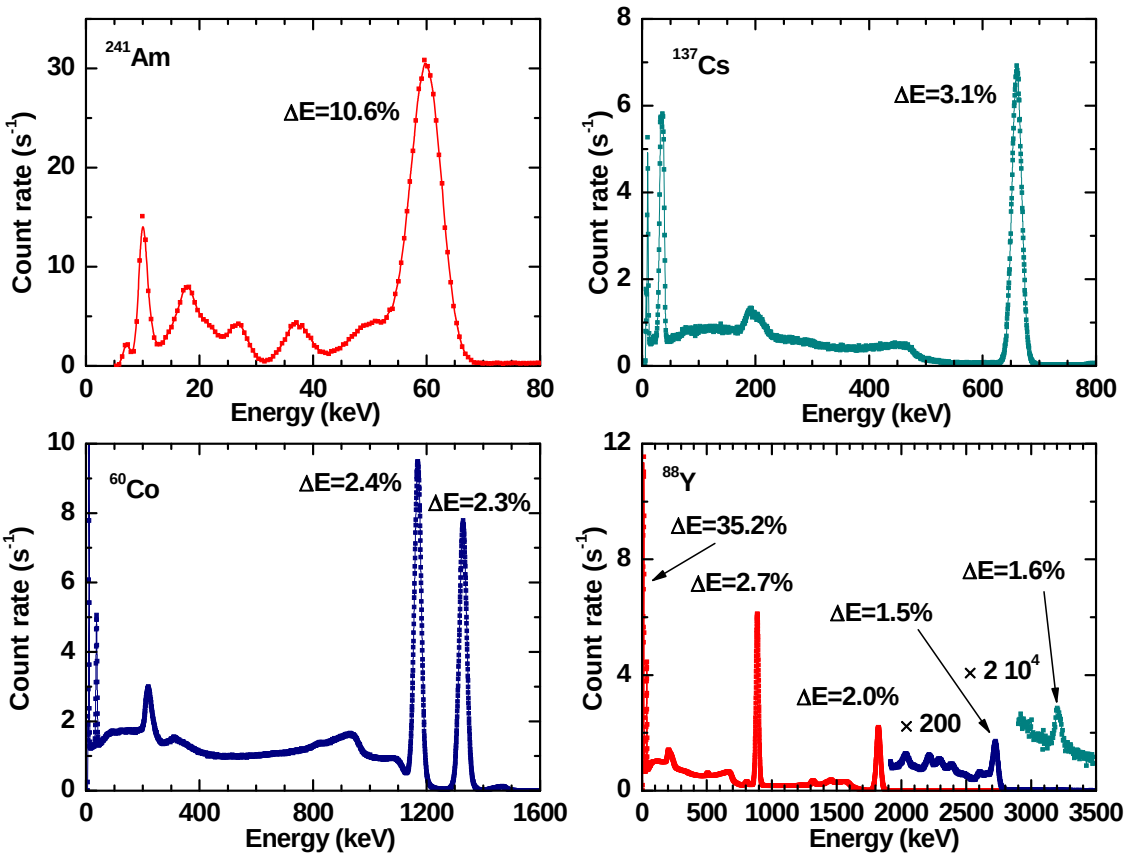

Fig. 2 - The measured response of the detector to ^{241}Am, ^{137}Cs, ^{60}Co and ^{88}Y radioactive sources. Measurements were carried out at room temperature under full area illumination. The FWHM energy resolutions range from 10.6 % at 60 keV to 2.3% at 1332 keV and to 1.6% at 3219.7 keV.

The bias voltage and shaping time settings have been optimized using ^{88}Y and ^{152}Eu radioactive sources. These sources cover a wide range of energy from 14 keV up to 1836.1 keV using direct line emission and up to 2734 keV using sum peaks. For these measurements the ^{88}Y peak at 3219.7 keV was not used because of its low intensity.

We found that above +700 V the detector response starts to show signs of PMT saturation, as illustrated in Fig. 3 (left) in which we plot the residuals of linear fits for biases ranging from 300 V to 800 V as a function of energy. The residuals are defined for a given data point, as the difference between the experimental value and the expected or fit value, divided by the experimental value. An optimum resolution of 2.8% for the ^{152}Eu line at 778.9 keV is reached at +400 V.

Following initial tests, we choose an operating bias of +520 V, which gave a good compromise between considerations of wide dynamic range, linearity and energy resolution.

In Fig. 3 (right) we plot the measured FWHM energy resolution at the optimum bias as a function of energy for four different shaping time settings. The best resolution is found for the shortest shaping time of 0.375 μs, as this is a better match to the characteristic signal decay time of the scintillator (16 ns), especially at high count rates.

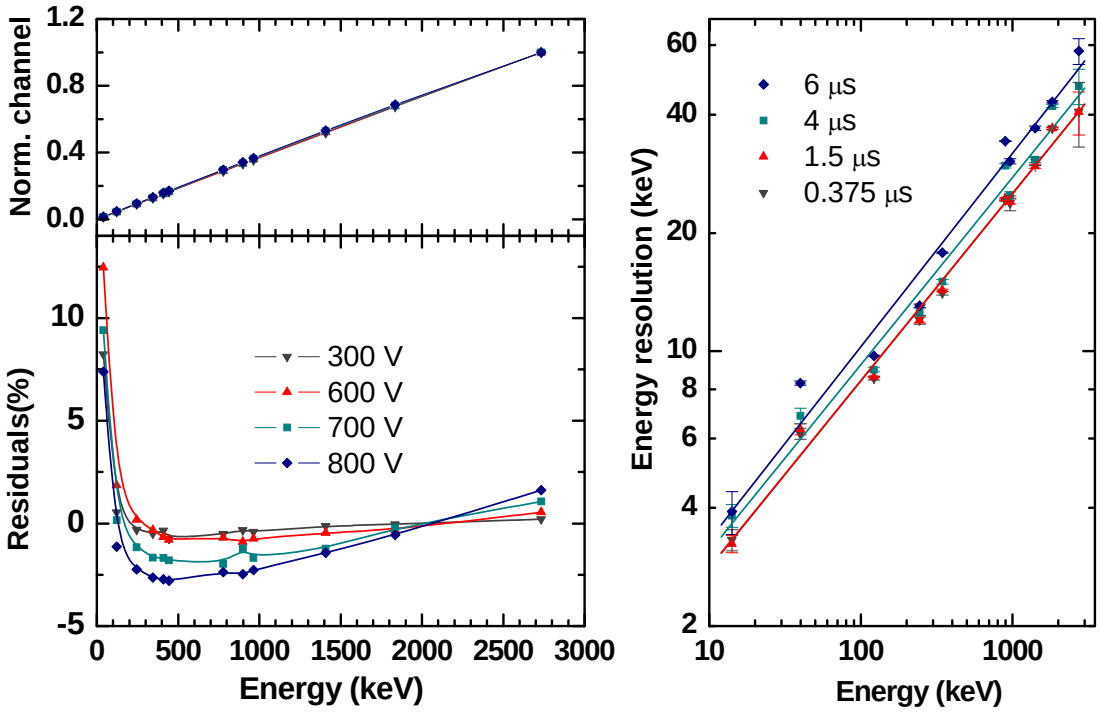

Fig. 3 - Test results obtained with ^{88}Y and ^{152}Eu radioactive sources. Left: the peak centroids and residuals derived from the spectra are plotted as a function of PMT bias. An optimum setting of +520 V was chosen for the PMT bias (see text). Right: the measured FWHM energy resolutions as a function of shaping time at +520V.

2.2 Intrinsic activity

Using the optimized settings we proceeded to collect source and background spectra for all the sources, see, e.g., Fig. 2 and Fig. 4. To prevent possible systematic errors, the spectra were collected using the same PMT bias setting (i.e. without un-biasing the PMT). A large intrinsic activity component is apparent in background spectra, which may in fact represent a fundamental limitation for low level activity measurements. This activity arises primarily from two components: the decay of radioactive ^{138}La which comprises 0.09% of naturally occurring lanthanum and a large internal alpha contamination resulting from the decay of ^{227}Ac [6]. Crystal processing refinements have already reduced this contamination for the 2″×2″ crystal by a factor of 15 compared with its 1″×1″ precursors.

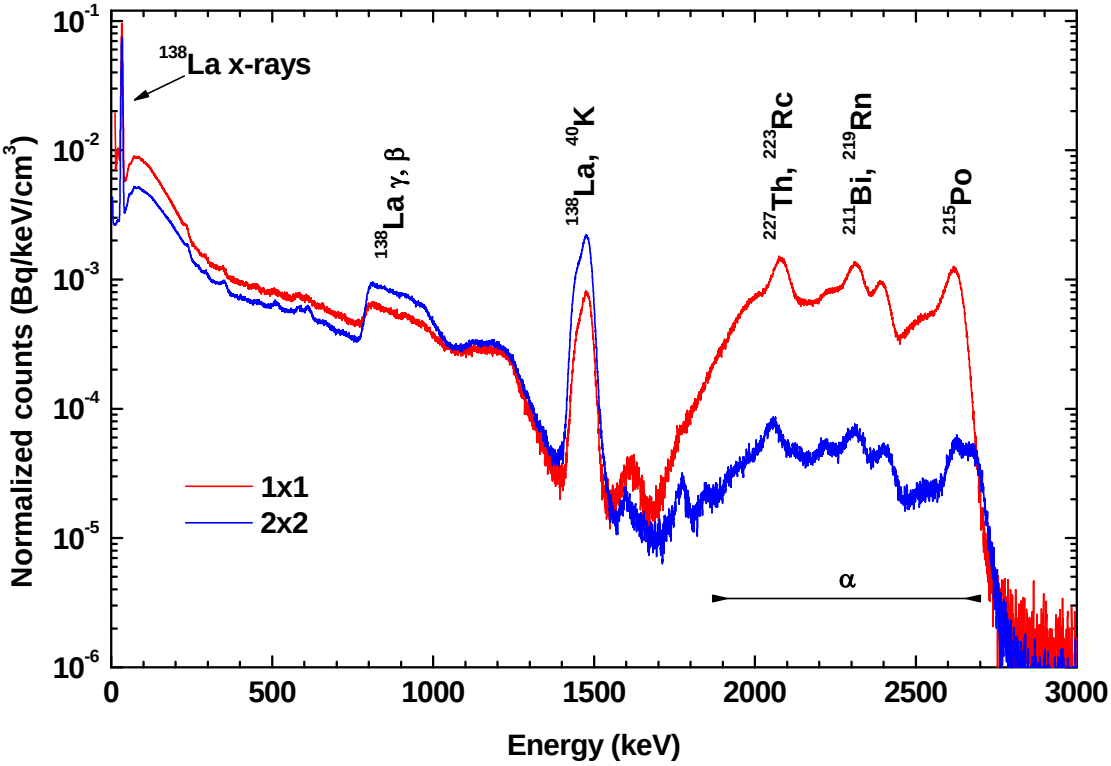

Fig. 4 - Comparison of the background spectra measured in the 2″×2″ and 1″×1″ crystals. The alpha contamination occurring in the energy range 1700 keV to 2700 keV has been drastically reduced with refinements in the processing of the precursors used in the growth technique from 0.6 cts/s/cm^3 to 0.04 cts/s/cm^3. The recorded total background rate (intrinsic activity plus laboratory background) is about 2 cts/s/cm^3 and 3 cts/s/cm^3 for the 2″×2″ and 1″×1″ crystal, respectively in the energy range 20 keV to 3000 keV.

In gamma-ray spectra, ^{138}La and ^{227}Ac activities manifest themselves as a line at 1436 keV and a broad triple peaked component between 1.7 MeV and 2.7 MeV, respectively (see Fig. 4). We estimate the light signal for alpha particles in $LaBr_3$

to be 35% of that for gamma-rays, in agreement with that measured by Hartwell and Gehrke for $LaCl_3$ [7].

2.3 Linearity

To measure the energy to channel conversion, the spectra collected were analyzed and their full energy peaks fitted with Gaussian functions in order to extract peak centroids and FWHM. Prior to the linearity measurements, the multi-channel analyzer was checked using a precision pulse generator to verify that channel zero corresponds to zero energy (within ± 1 channel) and the ADC conversion gain is linear with signal amplitude within ± 0.5% deviation.
The proportionality of response or linearity curve is shown in Fig. 5 (top) in which we show the peak channel data versus their nominal energies. The average error in the peak channel determination is less than 0.5%. In Fig. 5 (bottom) we show the residuals for linear and quadratic interpolations of the energy to channel conversion.

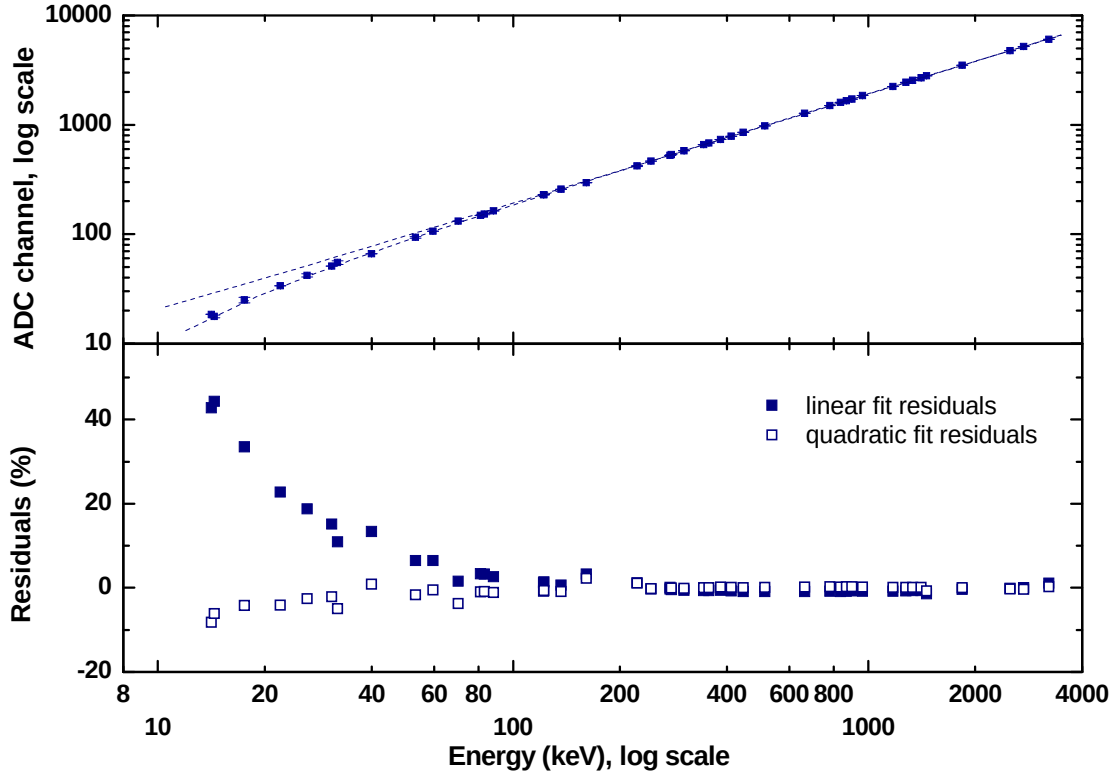

Fig. 5 – Top: detector energy to ADC channel conversion, or linearity curve. Experimental data are plotted with linear and quadratic polynomial fits. Bottom: residuals for linear and quadratic fits. As can be seen, a serious departure from linearity occurs below ~100 keV (~5% of the dynamic range).

For energies below 100 keV, *i.e.* the lower 5% of the dynamic range, a quadratic approximation better represents the experimental data. The non-linear proportionality is alternatively represented in Fig. 6 where, to enhance the non-linearity, ADC peak channel divided by the energy is plotted against energy. For a perfectly linear detector this value would be constant over the entire energy range. After normalization, we compare this result with that obtained at HASYLAB (Fig. 3 of Chapter 2). The stronger deviation observed below 100 keV in the present case is evidence of PMT shortcomings.

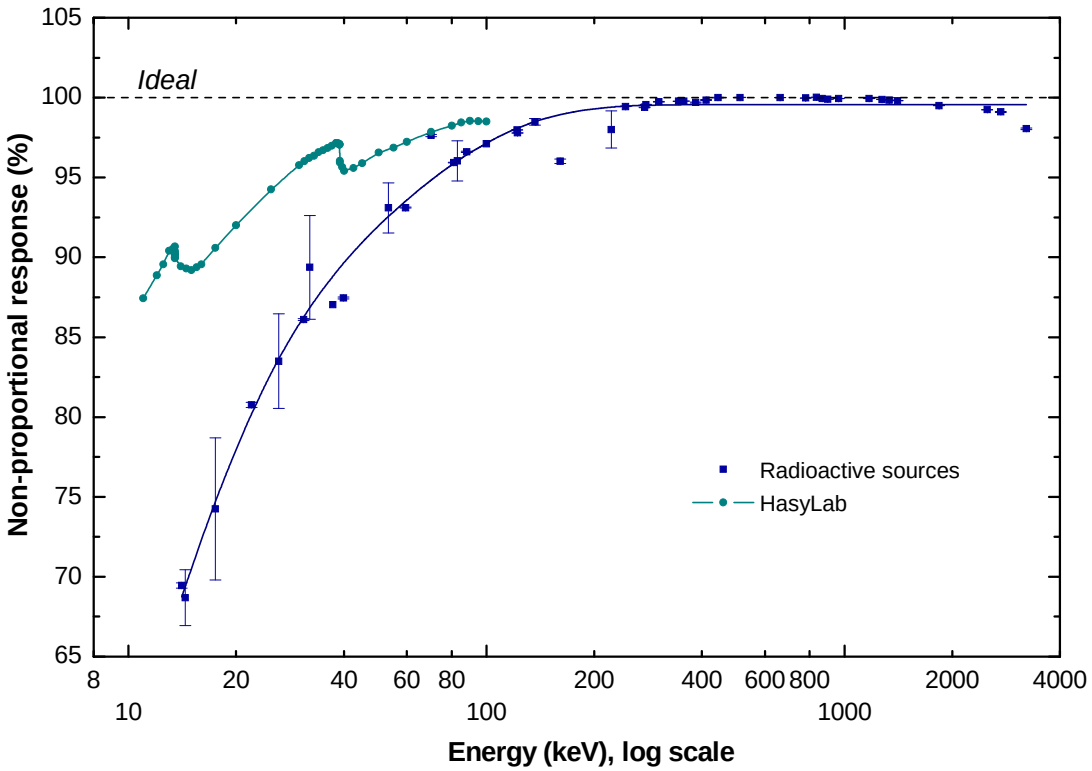

Fig. 6 - The detector proportionality curve as ADC peak channel position divided by the energy plotted against energy. Below 100 keV the same curve obtained at HasyLab is plotted for comparison after normalization.

2.4 Energy resolution

From the same analysis, we have evaluated the FWHM energy resolution versus energy. The conversion from FWHM channels to FWHM-energy has been carried out correcting for the non linearity in the detector response using a quadratic calibration. The results are plotted in Fig. 6, in terms of both energy resolution expressed in keV (ΔE) and energy resolution expressed as a percentage ($\Delta E / E$).

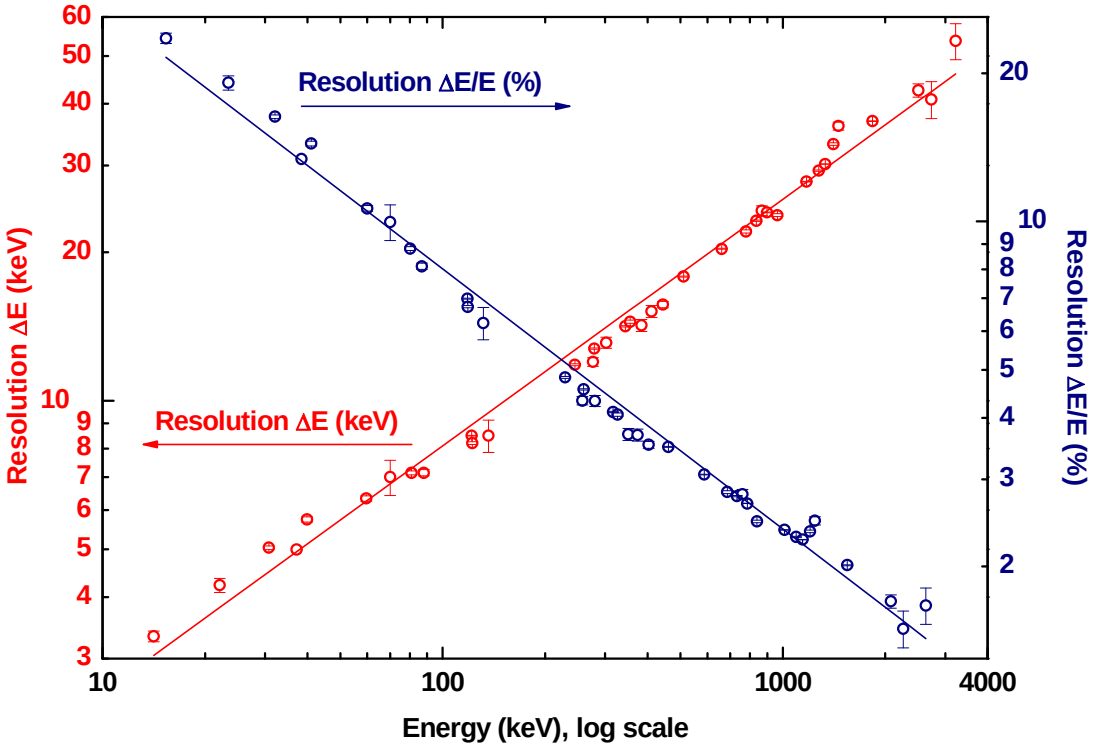

Fig. 6 – Data points are the measured energy resolutions for the 2″×2″ $LaBr_3$, in blue $\Delta E / E$ in percent and in red ΔE in units of keV. Lines are best fits of the data points.

The data are best-fitted by power laws as:

$$\Delta E(keV) = 0.81\, E^{0.499}$$

$$\frac{\Delta E}{E}(\%) = 81\, E^{-0.501} \qquad (1)$$

for the energy resolution expressed in keV and in %, respectively. The exponent of ~0.5 indicates that either the statistical fluctuation dominates the energy resolution or that other present contributions scale with the same root of the energy as well. The statistical term of the energy resolution due to the Poisson

statistics in the number of detected photons can be analytically expressed as [8,9,10]:

$$\frac{\Delta E}{E}(\%) = 100 \times 2.35 \sqrt{\frac{1+\nu}{\eta \alpha N_{ph}}} \tag{2}$$

where ν is the variance in the PMT gain due to the statistic of the electron multiplication; η is the PMT quantum efficiency (for a bi-alkali photocathode $\eta \cong 0.28$ at 380 nm [11]); N_{ph} is the number of photons generated in the scintillator, for $LaBr_3$ $N_{ph} \cong 60E$ (when the energy E is expressed in keV) [1,2,5]; α is the fraction of generated photons which are hitting the PMT photocathode and its typical value ~0.95. Using these last three values, expression (2) can be rewritten as:

$$\frac{\Delta E}{E}(\%) = 58.8 \sqrt{1+\nu}\ E^{-0.5} \ . \tag{3}$$

The variance ν cannot be directly measured because of the low PMT bias setting used, however it can be evaluated as follows. Using the gain versus bias characteristic available from the manufacturer, we can first evaluate the multiplication factor δ characteristic of our PMT (Hamamatsu R6231). With a constant potential difference between consecutive dynodes, as in our case, the overall gain and multiplication factor are related by [12]:

$$overall\ gain = G = a\ \delta^N \tag{4}$$

where N here is the number of dynodes (or stages) in the PMT and *a* is the fraction of photoelectrons collected by the multiplier structure: *a* is nearly unity for a well designed PMT. At the bias we chose for operation, +520 V, the manufacturer data show a PMT gain of ~8000. We then have for the multiplication factor:

$$\delta = \left(G \big/ a\right)^{1/N} = (8000)^{1/8} = 3.1 \ . \tag{5}$$

Assuming Poissonian statistics for the electron multiplication process, the variance ν is related to the multiplication factor δ by [12]:

$$\left(1+\nu\right) \sim 1 + \frac{1}{\delta - 1} = \frac{\delta}{\delta - 1} = \frac{3.1}{3.1 - 1} \sim 1.5 \tag{6}$$

so that 1+ν~1.5 is the variance characterizing our PMT. This value differs from that expected by the PMT specifications of about 1.25. The worse variance found in our setup is a consequence of the HV setting of +520V, a bias nearly half of the recommended (+1000 V), but chosen to preserve dynamic range and linearity. In other words, the compromise we made to achieved dynamic range and linearity did not allow the PMT to operate with the best possible multiplication variance.
For 1+ν = 1.5, Eq. (3) gives an analytical expression for the energy resolution of:

$$\frac{\Delta E}{E}(\%) = 72\, E^{-0.5} \quad . \tag{7}$$

The larger coefficient found by best fitting, see Eq. (1), which is 81, indicates that other contributions than photon statistics are indeed affecting the energy resolution. Moreover we can deduce that such contributions approximately scale with $E^{-0.5}$.
Indicating with R_{tot} the overall energy resolution and with R_{stat} the statistical contribution only, we can also evaluate the non statistical contribution, $R_{non\text{-}stat}$, as:

$$R_{non-stat}(\%) \sim \sqrt{R_{tot}^2 - R_{stat}^2} = \sqrt{\frac{81^2 - 72^2}{E}} = 37\, E^{-0.5} \tag{8}$$

Similarly, we can evaluate the energy resolution that would be achieved operating the PMT with its optimum variance of 1+ν = 1.25, i.e. $\Delta E/E(\%) = 75\, E^{-0.5}$. Specifically at 662 keV, the possible improvement is quantified as $\Delta E/E = 2.9\%$ instead of the measured 3.1%.

2.5 Proton response

The response of the detector to 90 MeV protons was assessed at the Kernfysisch Versneller Instituut in Groningen, Netherlands using the AGOR cyclotron. This machine can produce intense and tunable monoenergetic proton beams in the energy range 50 MeV to 191 MeV [13]. The spectrum corresponding to 90 MeV proton energy is reported in Fig. 7. In the spectrum is visible a second peak, of lower intensity corresponding to the simultaneous detection of two protons. The true energy of such an event is 2 × 90 = 180 MeV, however because of PMT gain saturation it is detected at 120 MeV only. The spectrum is also characterized by the presence of prompt gamma-ray following activation of material as the Al of the present in scintillator and PMT assembly. Taking the saturation into account, we estimated for the $LaBr_3$ detector an energy resolution $\Delta E / E = 0.8\%$ of which

0.4% can be attributed to the intrinsic spread in the beam energy (see Fig. 7 inset). Note, the measured 0.8% resolution must be considered an upper limit since, due to time constraints, we could not optimize the system to cover such a wide dynamic range.

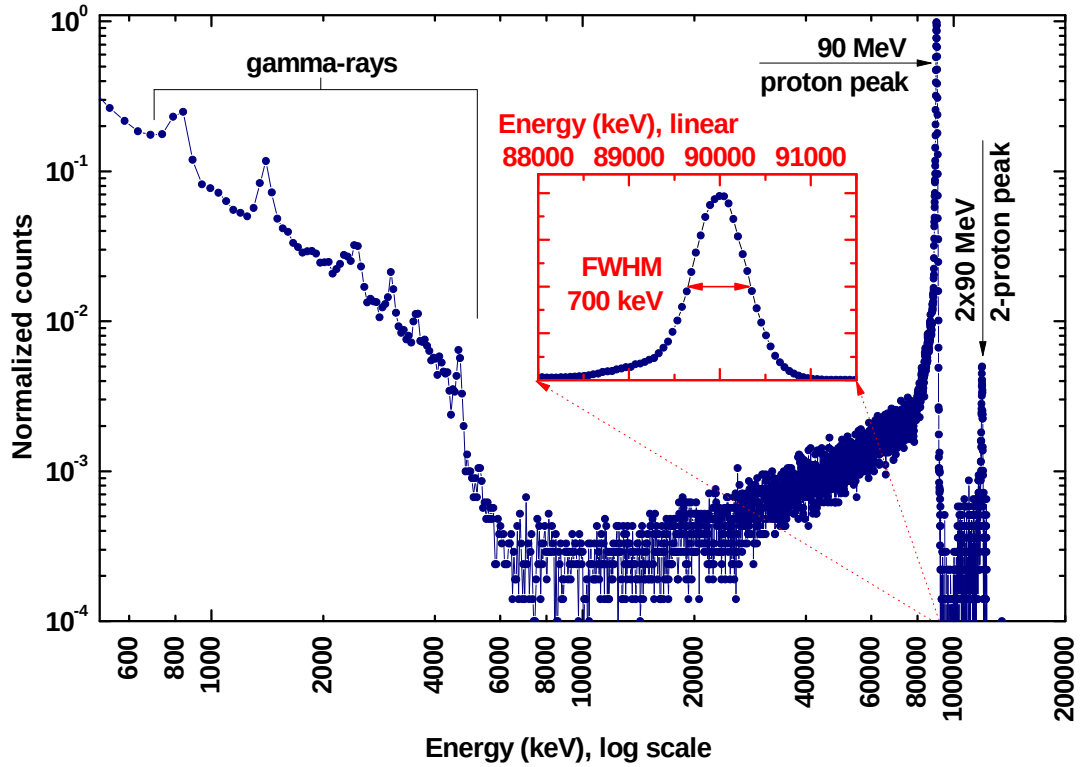

Fig. 7 - Detector response to 90 MeV protons measured at the AGOR cyclotron. The FWHM is 0.8%. The low energy peaks are due to secondary gamma-rays produced in the irradiation vault.

Extrapolating the gamma-ray calibration up to 90 MeV, we estimate the light yield for protons to be significantly less than that for gamma-rays, see also Chapter 5 Section 2.1. Protons generate higher ionization density compared to electrons of the same energy. We believe it is the protons higher ionization density that effectively quenches and reduces their relative light output compared to gamma-rays.

3 Summary of the results

The present results show that $LaBr_3$ is indeed a very promising material, particularly for those applications where large volume scintillators still provide the most sensitive approach to gamma-ray spectrometry (*e.g.,* remote sensing, home-land security). Refinements in the production techniques have reduced the internal specific activity to a level much less than for the earlier generation crystals. For energies above 1.6 MeV, this potentially extends applications into low level counting.

Finally, the last generation of large volume detectors has been readout with PMTs that utilize a lower number of dynode stages and thus better matches the high light output of the crystal. This has been partially successful. Lowering the number of dynodes benefits in the system dynamic range and linearity but does not allow the best energy resolution to be achieved. All this suggests that alternative read out have to be explored. Currently we are experimenting with silicon drift detectors (SDD) for which excellent results have been already demonstrated for small 1 cm^3 crystals [10].

References

[1] P. Dorenbos et al., "Gamma Ray Spectroscopy with a Ø19×19 mm^3 $LaBr_3$:0.5% Ce^{3+} Scintillator", IEEE Trans. Nucl. Sci., 51 (2004) 1289.

[2] G. Bizarri et al. "Scintillation Properties of Ø1×1 $Inch^3$ $LaBr_3$:0.5% Ce^{3+} Crystals", IEEE Trans. Nucl. Sci., 53 (2006) 615.

[3] A. Owens et al., "The hard X-ray response of Ce doped lanthanum halides scintillators", Nucl. Instr. and Meth. A 574 (2007) 158.

[4] A. Owens et al., "Assessment of the tolerance of $LaBr_3$:Ce scintillators to Solar proton events", Nucl. Instr. and Meth. A 572 (2007) 785.

[5] http://www.detectors.saint-gobain.com/

[6] B.D. Milbrath et al., "Characterization of alpha contamination in lanthanum trichloride scintillators using coincidence measurements", Nucl. Instr. and Meth., A547 (2005) 504.

[7] J.K. Hartwell and R.J. Gehrke, "Observations on the background spectra of four $LaCl_3$(Ce) scintillation detectors", Applied. Radiation and Isotopes, 63 (2005) 223.

[8] E. Breitenberger, "Scintillation spectrometer statistics", Progress in Nucl. Phys., 4 (1955) 56.

[9] P. Dorenbos et al., "Non-Proportionality in the Scintillation Response and the Energy Resolution Obtainable with Scintillator Crystals", IEEE Trans. Nucl. Sci., 46 (1995) 2190.

[10] C. Fiorini et al., "Gamma-ray spectroscopy with $LaBr_3$:Ce Scintillator Readout by a Silicon Drift Detector", Nuclear Science Symposium Conference Record,. 1 (2005) 230.

[11] "Photomultiplier Tubes, Basics and Applications", 3rd ed., Hamamatsu Photonics K.K., Electron Tube Division, 2006, 138. *Available on line at www.hamamatsu.com*

[12] G. Knoll, "Radiation detection and measurements", 3rd ed., John Wiley and Sons, 2000, 270.

[13] S. Brandenburg et al., "AGOR status report", Proceedings of the XVIth International Conference on Cyclotrons and their Applications, East-Lansing (USA), ed. F. Marti, AIP Conf. Proc., 600 (2001) 99.

Chapter 5

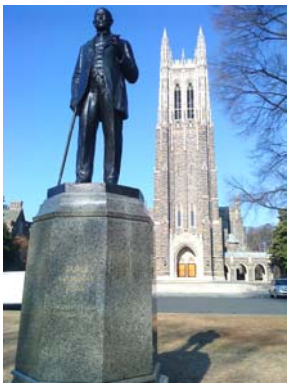

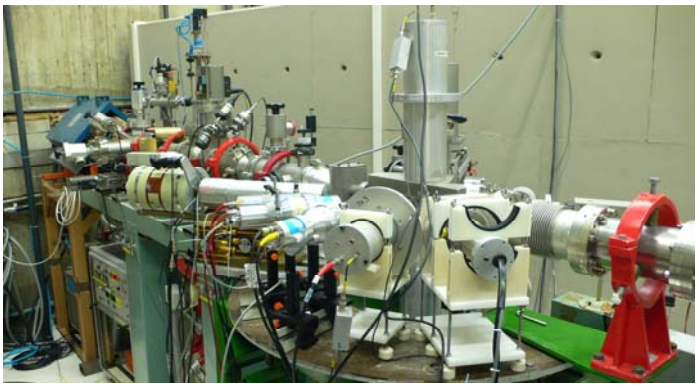

High energy gamma-ray spectroscopy with $LaBr_3$ scintillator detectors

Lanthanum bromide scintillator detectors produce very high light outputs (~60000 ph/MeV) within a very short decay time (typically ~20 ns) which means that high instantaneous currents can be generated in the photocathode and dynode chain of the photomultiplier tube (PMT) used for the scintillation readout. The net result is that signal saturation can occur long before the recommended PMT biasing conditions can be reached.

In search of an optimised light readout system for $LaBr_3$, we have tested and compared two different PMT configurations for detection of gamma-rays up to 15 MeV. This range was chosen as being appropriate for gamma-ray remote sensing and medium energy nuclear physics applications. The experiments were conducted at two facilities: the Laboratori Nazionali del Sud (LNS) in Catania, Italy [1] and the High Intensity Gamma-ray Source (HIγS) at Triangle University Nuclear Laboratory, in Durham, North Carolina, USA [2].

The PMT configurations we have tested are: 1) a standard dynode chain operated under-biased; 2) a 4-stage reduced chain operated at nominal inter-dynode bias. The results are that shortening the number of active stages, as in configuration 2), has advantages in preserving energy resolution and avoiding PMT saturation over a large energy range. However, the use of an under-biased PMT, configuration 1), can still be considered a satisfactory solution, at least in the case of PMTs manufactured by Photonis.
The results of this study will be used in support of the Mercury Gamma-ray and Neutron Spectrometer (MGNS) on board of BepiColombo, the joint ESA/JAXA mission to Mercury, scheduled for launch in 2015.

The content of this chapter is based on the following publication:

Quarati, F.G.A., Owens, A., Dorenbos, P., De Haas, J.T.M., Benzoni, G., Blasi, N., Boiano, C., Brambilla, S., Camera, F., Alba, R., Bellia, G., Maiolino, C., Santonocito, D., Ahmed, M., Brown, N., Stave, S., Weller, H.R., Wu, Y.K.
High energy gamma-ray spectroscopy with $LaBr_3$ scintillation detectors
Nucl. Instr. and Meth. A 629 (2011) 157

DOI: 10.1016/j.nima.2010.11.035

1 Introduction: *Lanthanum bromide for space exploration*

In late 2006, about 5 years after its discovery [3], large volume (3″×3″) $LaBr_3$ spectrometer became available within the European Space Agency (ESA) project for their application in space exploration. As part of the development project, a comprehensive assessment of their radiation tolerance was undertaken, see Chapter 2 and [4,5], after which it was confirmed the choice to fly a $LaBr_3$ scintillator detector on the joint ESA/JAXA mission to Mercury: BepiColombo.
For the mission, a 3″×3″ $LaBr_3$ gamma-ray spectrometer will remotely sense Mercury by detecting gamma-ray lines emanating from natural and activated surface elements. More information on this particular application of $LaBr_3$ spectrometers can be found in [6,7,8]. The energy range of the instrument needs to extend over the nuclear transition region (150 keV – 10 MeV) in order to successfully investigate the chemical composition of Mercury's shallow surface.
We have tested our detectors up to 15 MeV, exceeding the instrument's dynamic range by nearly a factor of two which is standard pre-flight calibration practice to avoid uncertainty encountered at the end of the detection range. Specifically, if we could demonstrate the operation of $LaBr_3$ spectrometers with a proportional response at nearly twice the required energy range, we gain a safe margin to avoid any deterioration in response due to instrument aging during the cruise and subsequent operation in space.
We also need to guarantee the ability to quickly and effectively calibrate the spectrometer once in orbit around Mercury. For $LaBr_3$ we can use its self activity as a calibration source, in particular its ^{138}La line at 1470 keV [9]. This line offers a very reliable calibration point because of its peculiar shape. However, we can effectively use this line to calibrate the instrument's entire dynamic range only if the response is linear. Experiments have shown that $LaBr_3$ spectrometers potentially suffer from photomultiplier tube (PMT) saturation [10,11,12], which could substantially affect the ease to which this calibration can be carried out.
In this chapter, we first examine the problem of signal saturation occurring in $LaBr_3$/PMT assemblies and review possible solutions. We then report on the measurements and results of high energy gamma-ray detection and conclude by assessing operating limits and further implementations. The work is mainly focused on testing 3″×3″ $LaBr_3$ detectors, although results obtained with a smaller 2″×2″ $LaBr_3$ detector are also reported. The main conclusion of this study is that $LaBr_3$ material is entirely suitable for inclusion, not only on the BepiColombo mission to Mercury, but also to the Jovian system as recently proposed by the ESA/NASA Laplace mission.

2 PMT signal saturation with $LaBr_3$ and possible solutions

2.1 Origin and evidence of PMT saturation

Among scintillator detectors, $LaBr_3$ offers superior energy resolution mainly because of its high light output of ~60000 ph/MeV. Its scintillation process is also very fast, with 1/e decay time of 16 ns [10,13]. Light output and decay time directly contribute to the current flowing into the PMT, photocathode and dynode chain, which forms the detection signal.
For scintillator/PMT assemblies the anode peak current I_a can be approximately expressed as:

$$I_a = \frac{Light\ Output \times Quantum\ Efficiency \times e \times Gain}{Decay\ Time} \tag{1}$$

where e is the electron charge. With reference to the literature, e.g. [14,15], I_a can be evaluated for the most common scintillator detectors. This is summarised in Table 1, clearly showing that $LaBr_3$ surpasses all other scintillator detectors in terms of photocathode and anode peak currents. Actually, below a certain scintillation decay time, it is a combination of scintillation decay and PMT transit time spread which determines I_a intensity [16]. A typical value of transit time spread for box and grid PMTs can be taken to be 10 ns [17]. This value summed with the scintillation decay time has been used for a second evaluation of I_a for the "faster" scintillators with decay time <50 ns and it is reported in brackets in Table 1. The two values of I_a represent the lower and upper evaluation limits.
$LaBr_3$ represents a bright and fast source of light pulses which has not been available before with other scintillator detectors, so that new techniques and tailored PMTs are needed to optimize spectroscopic performance.
To date, efforts in improving scintillator performances have concentrated more on increasing the photocathode quantum efficiency (QE), see Hamamatsu "Ultra Bialkali" [18,19,20] and Photonis "Clarity" [21,22]. A review for these new PMTs is available from Mirzoyan et al. [23]. Recently, photocathodes with QE > 40% have been advertised by both Hamamatsu and Photonis. However, beside its benefit for energy resolution through enhanced statistics, an increased QE also increases the current flowing in the photocathode and the dynode chain, which exacerbates saturation problems.

Table 1 – Comparison of photocathode and anode peak currents generated in the most common scintillation detectors for 1 MeV absorbed gamma-ray. The anode peak currents (I_a) are evaluated assuming a PMT gain of 2.5×10^5, typical for 8-stage PMTs.

	Density (g/cm^3)	Z_{eff}	Wavelength of max emission (nm)	Light Yield (phe/keV)	Decay Time (ns)	Typical photocathode QE (%)	Photocathode current per absorbed MeV (μA)	Anode peak current (I_a) per absorbed MeV (mA)
NaI:Tl	3.7	50	415	38	250	30	0.0073	1.82
CsI:Tl	4.5	54	550	54	1000	7	0.0006	0.15
CsI:Na	4.5	54	420	41	630	30	0.0031	0.77
CsI*	4.5	54	315	2	16	17	0.0034	0.85 (0.52)
BGO	7.1	73	480	10	300	21	0.0011	0.28
BaF_2 (fast)*	4.9	51	220	1.8	0.8	1	0.0036	0.9 (0.07)
BaF_2	4.9	51	310	10	630	15	0.0004	0.09
$LaCl_3$:Ce*	4.5	40	350	49	28	27	0.0745	18.6 (13.7)
$LaBr_3$:Ce*	5.1	45	380	63	16	30	0.1890	47.3 (29.1)
LYSO*	7.1	62	420	32	41	29	0.0368	9.21 (7.4)

*For these scintillation crystals, we report in brackets the anode peak current value evaluated using PMT transit time plus scintillation decay time.

In proton measurements at the Kernfysisch Versneller Instituut in Groningen, The Netherlands [24], we obtained evidence of saturation, as shown in Fig. 1. Two different setups have been used to detect protons with energies from 8 MeV to 90 MeV. The first setup is a standard $LaBr_3$/PMT assembly; in the second we have introduced a neutral density filter between crystal and photocathode to attenuate the light yield by a factor of 15. The proton energy range has been achieved using calibrated layers of degraders, i.e. aluminium plates that reduce the primary beam energy, 90 MeV, by a known amount; a similar technique was used for the proton irradiations [4]. Because the energy degradation process is stochastic, the intrinsic beam energy spread increases after degradation affecting the energy resolution evaluation. At the highest energy, 90 MeV, we have measured a FWHM of 1.1% with the attenuated setup and 0.8% with the unattenuated setup. The latter value is corrected for the non-proportional response, having carried out its evaluation in the energy scale, while the higher value measured with the attenuated setup is consistent with the loss of photons in the filter. Both values could be affected by the intrinsic beam energy spread of 0.5%.

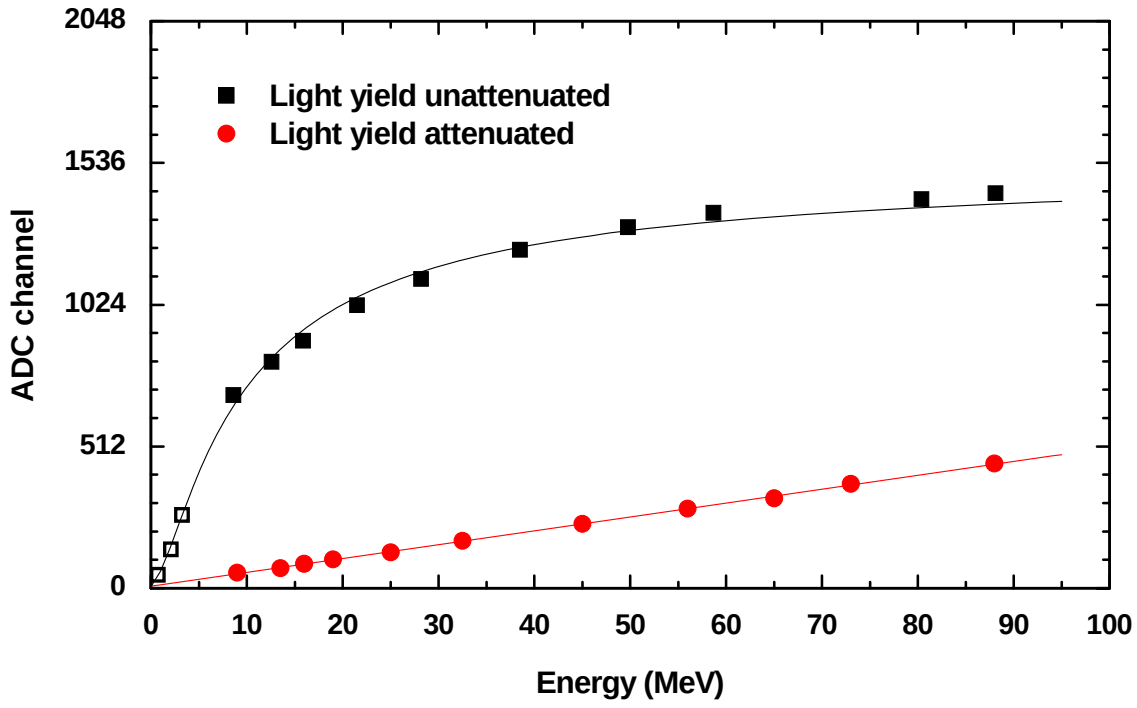

Fig. 1 – Evidence of saturation in the energy response of $LaBr_3$ detector to protons. When the scintillation light reaching the photocathode is attenuated by a factor of 15 (using a filter between the crystal and the photocathode), the response proportionality again becomes linear. The open square symbols used for the unattenuated plot indicate data from gamma-ray detection.

As seen in Fig. 1, a linear proportionality is only achieved with the attenuated setup, meaning that the non-proportional response observed when collecting all the scintillation light is due to saturation of either the photocathode, the dynode chain, or both.
For the unattenuated setup we have included three gamma-ray lines in Fig. 1 after correcting for the difference in ionization of protons and gamma-rays in $LaBr_3$. In a parallel experiment, we have estimated the proton ionization to be 0.76±0.03 times less than that of gamma-rays. The three gamma-ray lines are: the 511 keV annihilation line, the 1470 keV from $LaBr_3$ self activity, and the 2.27 MeV decay line of ^{24}Na generated in Al by proton activation. We can not report the same gamma-ray lines for the attenuated setup because of the degraded energy resolution, caused by light attenuation. The data acquired with the unattenuated configuration clearly show that saturation starts to occur to some extent already for the lower proton energy of 8.6 MeV. In case of gamma-rays, the limit before saturation occurs could be even lower because of their higher ionization rate.

2.2 The main causes of PMT saturation

In order to avoid the anode current influencing the dynode voltage drop, with negative consequences for gain loss and then for response proportionality, the current flowing in the voltage divider has to be over 10 times higher than the electron multiplication current [16,25].
For $LaBr_3$ we expect an anode peak current of approximately 47 mA for a detected gamma-ray of 1 MeV and 15 times that current for a 15 MeV photon. For operation at this energy, we would need a totally unpractical HV supply capable of delivering at least 0.047 A × 15 × 10 = 7 A at ~1 kV of bias. Since the HV supply maximum current requirement is for a peak and not a direct current, we can in principle relax the need by inserting capacitors in parallel with the resistor [16]. However for this solution we will need high value capacitors along the whole voltage divider network, and we have experienced that a high capacitive voltage divider chain deteriorates the signal-to-noise ratio and the energy resolution.
Another solution could be active voltage dividers. However, these are not particularly attractive for space applications because of the extra demands on power and the relatively more complex circuitry. A classic example of this kind of voltage divider is available from [26]. The scheme recently proposed by Kalinnikov et al. [27] is a promising alternative more suitable for space applications because of the reduced demand for power. We have not yet explored its possible application with $LaBr_3$.

In parallel to the effects on the voltage divider, high anode peak current (and charge) also generates space charge effects between dynodes which can modify the electron trajectories and deteriorate the multiplication process and response proportionality [17,25,28]. It is mainly the particular dynode design which determines the maximum tolerable current, and typically for box and grid PMTs this is reported by Photonis to be 10-50 mA [28], - a value comparable with the detection of 1 MeV gamma-rays (Table 1).
Photocathode saturation can occur if the photocathode current exceeds a particular value causing a potential drop across its surface. This potential drop modifies the electric field between the photocathode and the 1st dynode, deteriorating the collection of photoelectrons. The current limit depends on the actual photocathode resistivity, which depends on the particular photocathode material and operational temperature. In fact, most of the studies of photocathode saturation have been carried out in the context of PMT cryogenic applications where the photocathode resistivity dramatically increases because of the low temperature. In this case, even a few nA of photoelectron current can saturate the photocathode [29,30]. For Hamamatsu "Ultra Bialkali" photocathodes, Nakamura et al. [19] and Suyama and Nakamura [20] report a value of ~300 nA as a current limit before saturation occurs. This value is very close to the estimated photocathode current corresponding to the absorption of a 1 MeV photon in $LaBr_3$, ~200 nA (Table 1). We found no specific data for Photonis PMTs. In general, the maximum tolerable photocathode current can vary as much as 3 orders of magnitude for bialkali photocathodes (0.01 μA – 10 μA), depending on its particular composition [17].

2.3 Configurations for $LaBr_3$ scintillation readout

Once a particular PMT photocathode is chosen, saturation cannot be avoided, but only mitigated in its effects by keeping a high bias between the photocathode and the 1st dynode [17]. This is simply achieved by increasing the resistor values in the photocathode-grid-1st dynode part of the chain.
In our study, we have focused on reducing the effect of anode peak current on PMT saturation by testing several solutions to reduce PMT gain and therefore the current flowing in the PMT. A possible way to reduce the PMT gain is simply to reduce its bias. Alternatively, the number of PMT stages can be reduced.
Reducing PMT bias has two advantages: reducing the gain and slowing down electrons during the multiplication process. On the other hand, reducing the number of active stages allows PMT operation at a higher inter dynode bias reducing the variance in the electron multiplication and hence enhancing the energy resolution [10,16,25].

Table 2 – Resistor ratio of the voltage dividers used for the two configurations, under-biased and 4-stage reduced, and for the tapered voltage divider.

	K	G	D1	D2	D3	D4	D5	D6	D7	D8	A
under-bias	2.2	2.2	1	1	1	1	1	1	1	1	
4-stage reduced	2	2	1	1	1	n/a	n/a	n/a	n/a	n/a	
tapered	2.1	2.1	1	1.3	1.3	1.6	2.3	2.6	3.2	2.8	

We tested a number of alternative solutions to reduce the PMT gain and/or the number of active stages. These include: 1) tapered voltage dividers (its scheme is reported in Table 2); 2) extraction of signals from an intermediate dynode with the insertion of a resistor between the dynode and the voltage divider chain leaving the rest of the voltage divider operating as in standard conditions (this has been tested by extracting the signal at the 4th, 5th and 6th dynode); 3) extraction of signals from a particular dynode leaving the rest of the voltage divider unbiased; 4) extraction of signals from a particular dynode leaving the rest of the voltage divider at the same potential as that of that particular dynode.
Laboratory tests up to ~2.5 MeV, and in some cases measurement campaigns up to 9 MeV, showed that none of the 4 configurations above is satisfactory because of degraded energy resolution (>4% at 662 keV) and/or persistent saturation (>10% deviation at 9 MeV) for a wide range of HV settings, typically from 200 V up to 1200 V.
Voltage divider schematics of the two best configurations are reported in Fig. 2 and Table 2, while their nominal characteristics vs. applied bias are reported in Table 3. Configuration 1 is simply a standard voltage divider operated at low HV bias with slightly higher value resistors between the photocathode and the 1st dynode. In the reduced stage configuration the dynode chain is truncated at the 4th dynode where the signal is extracted by the addition of a load resistor between the high voltage divider and the dynode itself. The rest of the dynode chain and the anode are directly connected to the 3rd dynode potential. This arrangement forces an electron possibly emitted by the dynode acting as a collector, back to it to be collected, as schematically reported in Fig. 2. This configuration is derived by Dorenbos et al. [10] but using a positive HV polarity, which is preferred for space applications for grounding reasons.
Moreover, the 4-stage reduced configuration described above has been tested when extracting the signal from the 6th, 5th and 3rd dynode. While extracting from the 6th and 5th dynode a residual saturation is still observable, extracting the signal from the 3rd dynode results in a disproportionate increase in noise. This is

most likely caused by the PMT manufacturer design that has two distinct pin contacts to the 3rd dynode, possibly creating an internal electrical loop.

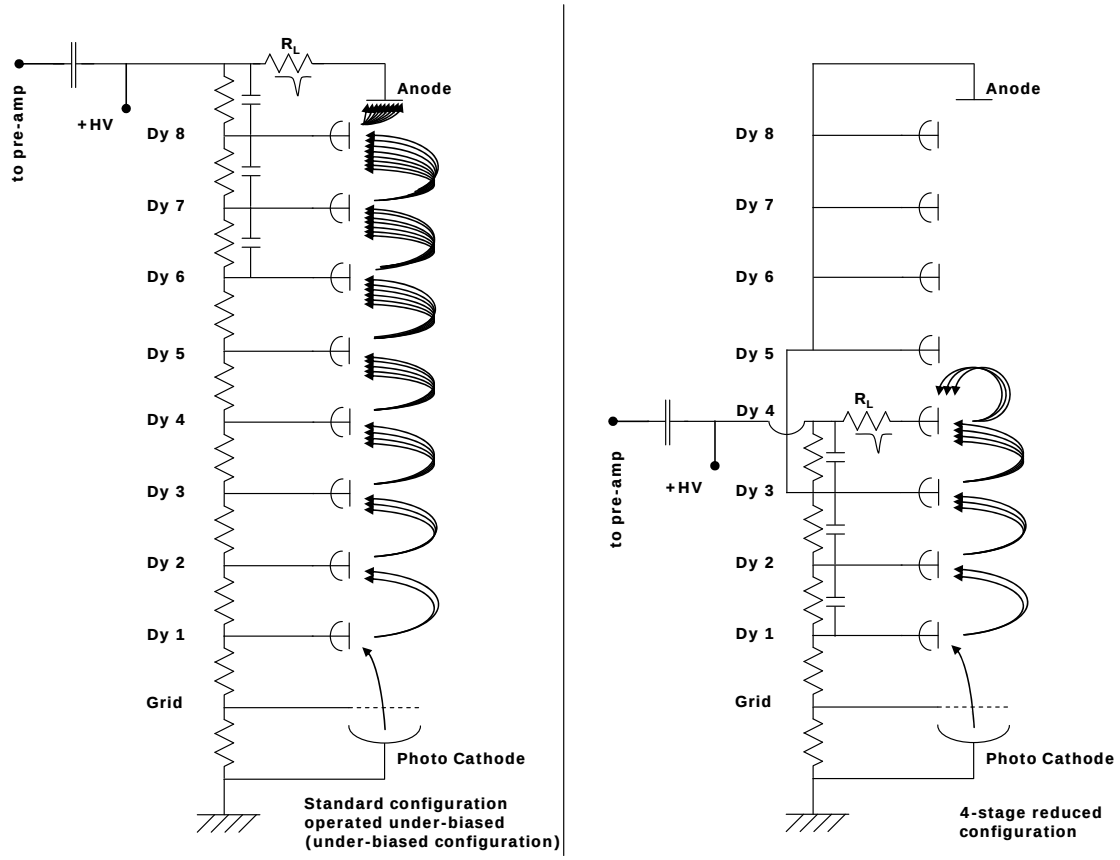

Fig. 2 – Schematic of the two voltage divider configurations chosen for testing using high energy gamma-rays. Left-hand: the standard configuration, operated under-biased. Right-hand: the 4-stage reduced configuration.

Table 3 – Electron multiplication characteristics vs. PMT bias for the two configurations based on manufacturer data, i.e. slope log gain vs. log bias: 5.6, for the Photonis XP5300 PMT. Because of the very similar characteristics these values apply to Hamamatsu R6231 PMT as well.

	PMT bias (V)							
	200	300	400	500	600	800	1000	1200
	Under-biased / 4-stage reduced							
Inter-dynode bias (V)	16 / 29	24 / 43	32 / 57	40 / 71	48 / 86	65/ 114	81/ 143	97/ 171
Multipl. Factor (δ)	1.5 / 2.2	2 / 2.9	2.4 / 3.6	2.8 / 4.2	3.2 / 4.8	3.9 / 5.9	4.6 / 6.9	5.2 / 7.8
Gain	23 / 11	226 / 24	1133 / 45	3954 / 73	1.1×10^4 / 110	5.5×10^4 / 206	1.9×10^5 / 329	5.3×10^5 / 473
Variance $1+\nu = \delta / (\delta - 1)$	3.0 / 1.8	2 / 1.5	1.7 / 1.4	1.5 / 1.3	1.4 / 1.3	1.3 / 1.2	1.3 / 1.2	1.2 / 1.2

3 Experiments

3.1 Devices and setup description

In our experiments we have used two packaged 3″×3″ $LaBr_3$ crystals supplied by Saint-Gobain Crystals [31] in the framework of our development project. The $LaBr_3$ crystals were coupled with two Photonis XP5300B PMTs. These PMTs, of the box and grid kind, are equipped with borosilicate windows.
We have used the voltage divider provided by Saint Gobain for the under-biased configuration, which follows Photonis's recommendation, with a unity gain buffer preamplifier. For the 4-stage reduced configuration, we used a Cremat 110 charge sensitive preamplifier [32].
Other standard spectroscopy instrumentation has been used for the experiments i.e. Ortec 671 shaping amplifiers (generally operated at 1 μs shaping time) and AmpTek 8000A multichannel analyzers [33]. We have also used low noise HV supplies from Bertan Associates Inc. [34] and Iseg Spezialelektronik GmbH [35].
In addition, we have tested a 2″×2″ $LaBr_3$ coupled with a Hamamatsu PMT R6231 with two voltage divider configurations using the same experimental setup as with the 3″×3″ $LaBr_3$. This PMT also is of the box and grid kind and has a borosilicate window.

3.2 Preliminary testing

We have carried out preliminary tests to investigate the optimization of bias settings for the two configurations and to evaluate their characteristic photoelectric yield (PY), i.e. *light output* × *quantum efficiency* × *collection efficiency*. We found that our two assemblies have an almost identical PY of about 19500+/-500 phe/MeV. This feature allows experiments to be run in parallel with two "twin" spectrometers.
The PY has been measured using the method described in Bertolaccini et al. [36] and de Haas et al. [37]. It consists of measuring the mean value corresponding to the multiplication of a single photoelectron (sphe) and using it to normalise the peak position corresponding to a given gamma-ray energy, 662 keV from ^{137}Cs and 88 keV from ^{109}Cd in our case. Due to the low signal to noise ratio characteristic of the sphe multiplication process, its measurement can only be carried out at high PMT biases, say from 1000 V and above, using all the PMT 8 stages of amplification, i.e. the standard configuration. Note that the error introduced in PY measurements by possible PMT saturation is 1%-2% against

the measurement's systematic error of about 5%, so that PMT saturation does not substantially affect the PY evaluation.

We also tested the behaviour of the energy resolution at 662 keV (^{137}Cs) versus the applied HV. For the standard configuration, we have found an energy resolution of 3% FWHM at 450 V. Below this bias the energy resolution quickly worsens to 4.5% at 350 V (see Fig. 3). At 750 V, the energy resolution slightly improves to 2.9%, although at 750V the saturation is far too high for proportional operation. Saturation is evaluated as departure from linearity in the energy range from 662 keV to 6130 keV using the gamma-ray lines reported in Table 4, with the exception of the La(n,γ) that overlaps with the 6130 keV double escape, 7 gamma-ray lines in total. The evaluation is carried out using a linear function with only one coefficient ($y = mx$) to calibrate the response in energy and evaluating its residuals as:

$$Residual\,(\%) = 100 \times \frac{Expected - Observed}{Expected} \tag{2}$$

The overall departure from linearity is then evaluated defining a Figure of Merit (FoM) that is simply the sum of the absolute values of the residuals over the entire set of energies, as:

$$FoM = \sum \sqrt{Residual\,(\%)^2} \tag{3}$$

The FoM against the HV bias setting is plotted in the upper part of Fig. 3 for the two configurations.

For the standard configuration, we have decided to use a 450 V bias which gives a good compromise between energy resolution and response proportionality for detection of high energy gamma-rays.

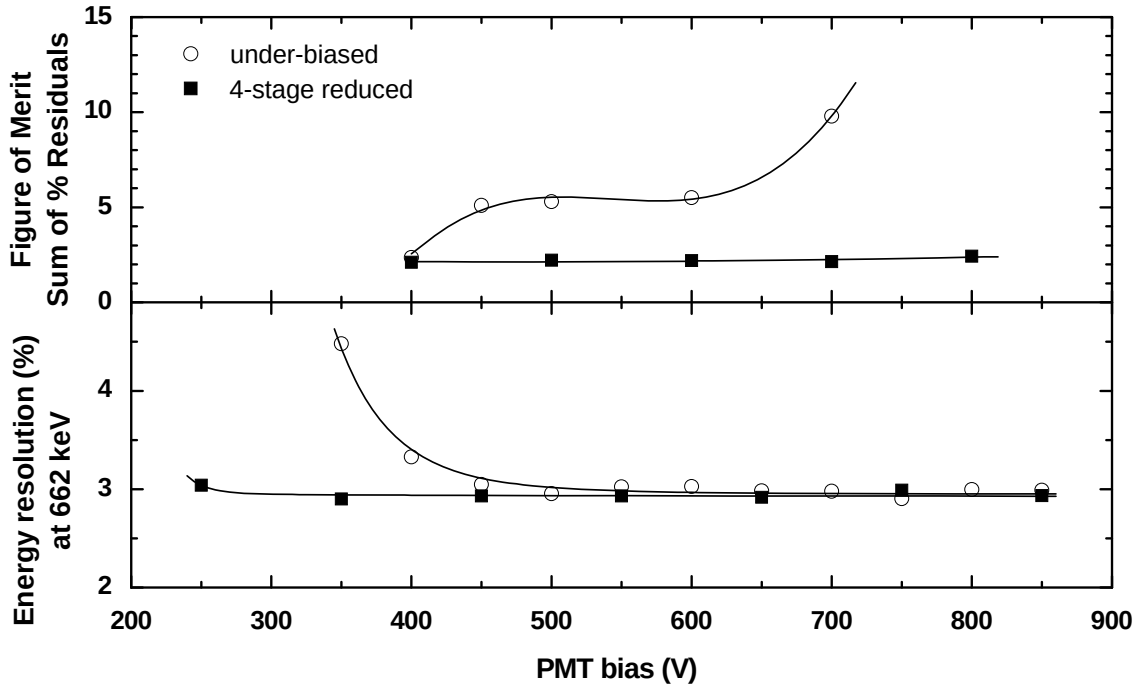

Fig. 3 - Energy resolution at 662 keV (bottom) and deviation from linearity (top) as function of applied PMT bias and for the two configurations. The deviation from linearity is expressed in FoM (Eq. (3)) for a linear fit in the energy range 662 keV to 6130 keV.

For the 4-stage reduced configuration, the energy resolution is 3% FWHM at 250 V applied bias (which corresponds to ~400 V of the standard configuration, see Table 3), and improves to 2.9% for 350 V bias (see Fig. 3). Above this bias, there is no further improvement in energy resolution. The reduced PMT gain allows the dynamic range of this configuration to have no HV limit. For this configuration, the saturation depicted in FoM only slightly increases from 400 V to 800 V of bias. We decided for this configuration to use a bias of 400 V.

3.3 The experimental facilities

The High Intensity Gamma-ray Source (HIγS) at Triangle University Nuclear Laboratory, in Durham, North Carolina, USA, provides an energy-adjustable high-intensity gamma-ray beam produced with an electron-storage-ring free-electron-laser (FEL). The FEL consists of electromagnetic undulators installed in a 1.2-GeV-electron storage ring [2,38]. The undulators also form the active elements of a 54 m optical cavity. The gamma-ray beam is produced by

backscattering the photons in the optical cavity off the stored electrons. The facility can produce photons up to energies of 60 MeV at the present time. This will increase to 100 MeV in the near future [38]. The highest intensity, after collimation, is close to 10^9 photons/sec at 10 MeV. For our measurements, in order to have ~100 counts/sec in the photopeak, we have attenuated the beam intensity using precision copper attenuators located about 30 m upstream.

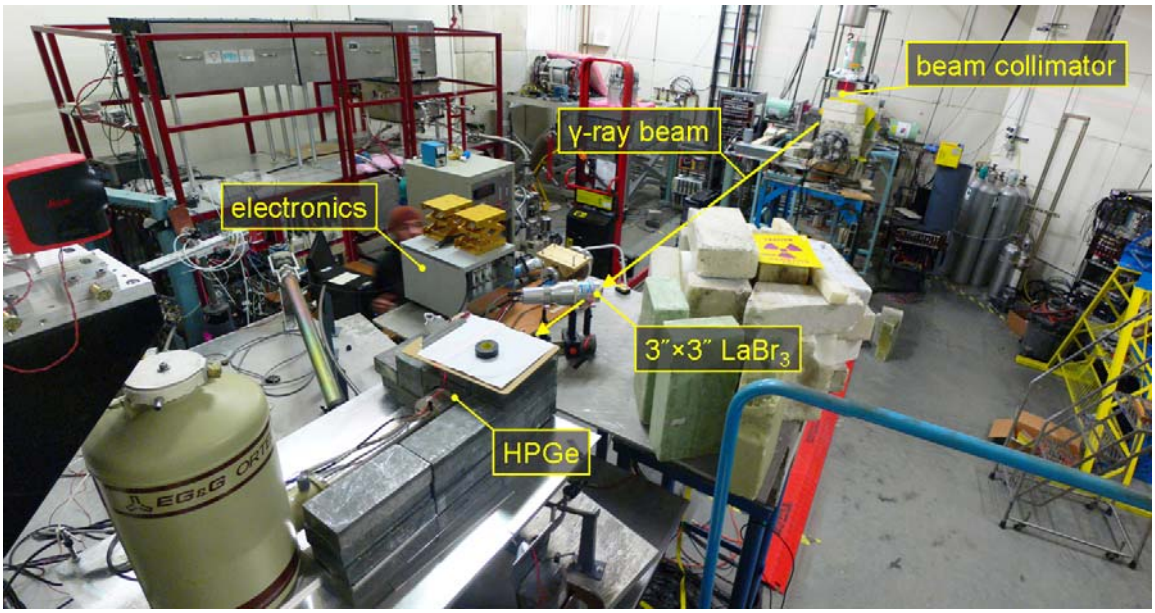

Fig. 4 – The gamma-ray beam vault at the HIγS facility. On the central bench is a 3″×3″ $LaBr_3$ ready for testing. Behind the wall is the electron storage ring.

Two different mirror configurations were used for the optical cavity to cover the energy range of interest up to 16 MeV. The 1st range was from 2.5 MeV up to 7.5 MeV and the 2nd range from 5.5 MeV up to 15.5 MeV. The two ranges overlap in order to allow the normalization of data points in the two energy ranges. The kinematics of the scattering process in which the gamma-rays are generated creates an intrinsic energy spread. This beam energy spread has been monitored by collecting reference spectra with a calibrated High Purity Ge (HPGe) spectrometer shown in Fig. 4. Across the entire test campaign the gamma-ray beam was found to be reproducible both in terms of peak energy and energy spread as measured by the HPGe spectrometer (Table 4). Using the HPGe spectrometer, the mean energy of the gamma-ray beam is known to a precision of about 0.1%.

Table 4 – Gamma-ray energies used in the experiments at the HIγS and LNS facilities. Beam energies and beam energy spreads have been measured using a calibrated HPGe spectrometer available at HIγS. The energy attributed to ^{138}La is taken from [9].

HIγS energy settings

Nominal energy (keV)	Beam energy (keV)	Beam energy spread (keV)
1st range		
2500	2517 ±3	34 ±5
3500	3504 ±2	46 ±4
4500	4488 ±2	53 ±4
5500	5537 ±2	74 ±11
6500	6527 ±6	88 ±10
7500	7463 ±8	87 ±8
2nd range		
5500	5527 ±5	51 ±5
6500	6519 ±5	59 ±7
7500	7549 ±3	66 ±6
9500	9527 ±4	82 ±5
11500	11534 ±7	113 ±21
13500	13544 ±11	123 ±13
15500	15597 ±16	108 ±24

Gamma lines from radioactive sources

Energy (keV)	Nuclide or reaction
661.66	^{137}Cs
1173.24	^{60}Co
1332.5	^{60}Co
1470	^{138}La ($LaBr_3$ self activity)
2223	H(n,γ)
4437	Am-Be and ^{12}C(n,γ)
5126	La(n,γ)
6130	PuC and ^{12}C(n,γ)
8997	Ni(n,γ)
15100	^{12}C(n,γ)

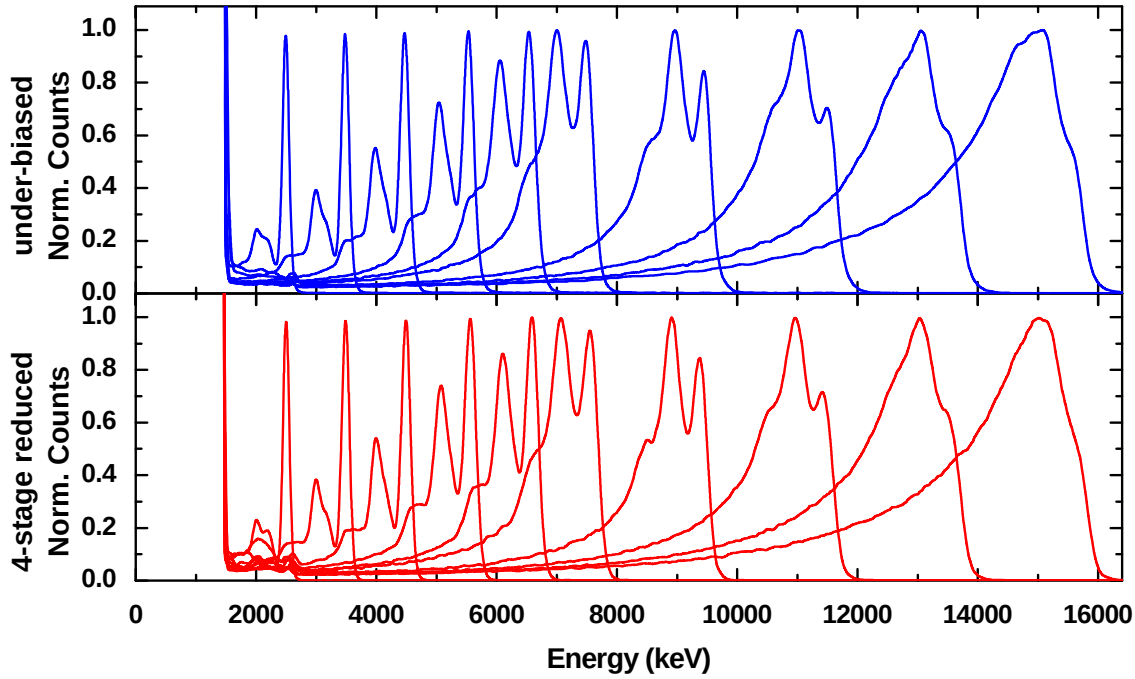

Fig. 5 – The gamma-ray spectra collected at HIγS with 3″×3″ $LaBr_3$ using the two PMT configurations. The energy settings are reported in Table 4. Top: under-biased. Bottom: 4-stage reduced. The PMT HV biases are 450 V for the under-biased configuration and 400 V for the 4-stage reduced configuration.

In addition to the gamma-ray beam, we have used gamma-ray sources to cover the lowest part of the energy range of interest (below 2.5 MeV) and to monitor the stability of our instruments during the two week measurement campaign. The used sources are ^{137}Cs, ^{60}Co and an Am-Be plus Ni capable of generating gamma-rays of energy 8997 keV [39].

More experiments have been performed at the Laboratori Nazionali del Sud (LNS) in Catania, Italy [1], part of the Istituto Nazionale di Fisica Nucleare (INFN). There, a 20 MeV proton beam from the 13 MV van der Graaf Tandem accelerator has been used to generate a gamma-ray line at 15.1 MeV from the de-excitation of ^{12}C. The count rate achieved from this reaction is low (< 1 count per second). From experience gained in early campaigns we placed the ^{12}C target inside the vacuum, in direct exposure to the proton beam to avoid protons reacting with air and generating undesired gamma-rays. An HPGe spectrometer was also available at LNS as a reference detector. The same set of radioactive sources used at HIγS has also been used at LNS with the addition of a Pu-C source emitting a gamma line at 6.130 keV.

4 Results and discussion

4.1 Proportionality of the response

Because of the capability of generating a given gamma-ray energy, the study of response proportionality has been carried out using HIγS data. The spectra collected are shown in Fig. 5 and correspond to the energy settings reported in the upper part of Table 4. The spectra are characterized by a high pair production probability and the related presence of 511 keV escape peaks. Because of the high pair production probability the Compton continuum is almost absent. From the extracted data, i.e. photon energy and relative peak channel, linear and quadratic fits can be computed to evaluate the proportionality quantitatively.

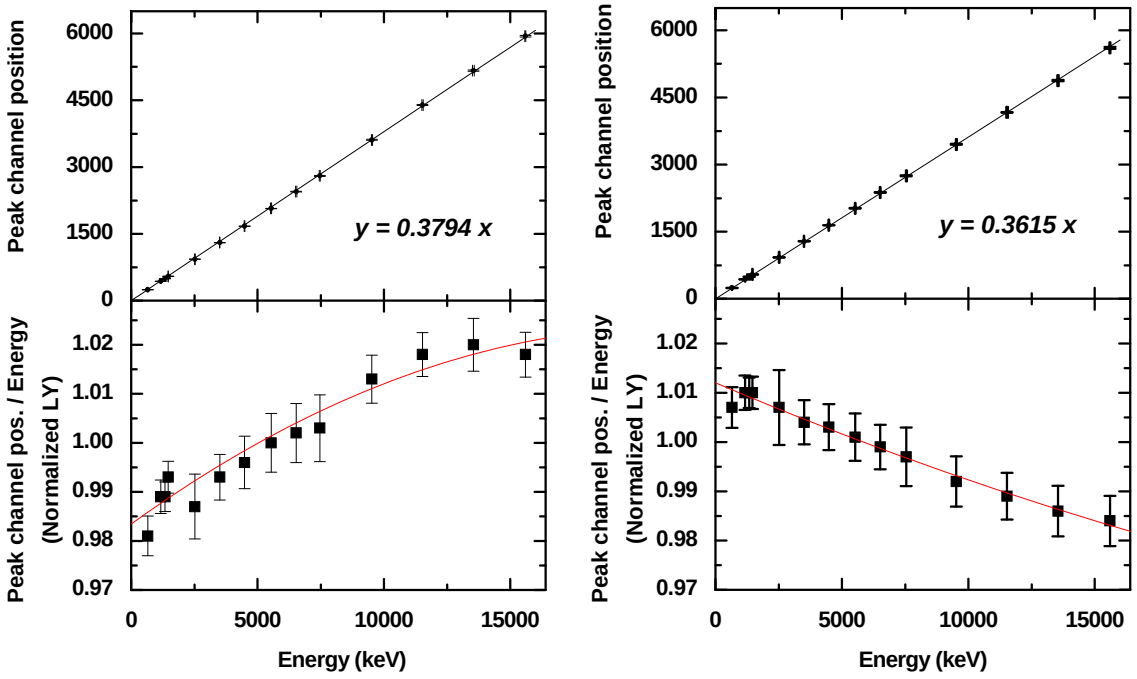

Fig. 6 – 3″×3″ $LaBr_3$ response proportionality: under-biased configuration (left), 4-stage reduced configuration (right). PMT HV biases are 450 V for the under-biased configuration and 400 V for the 4-stage reduced configuration.

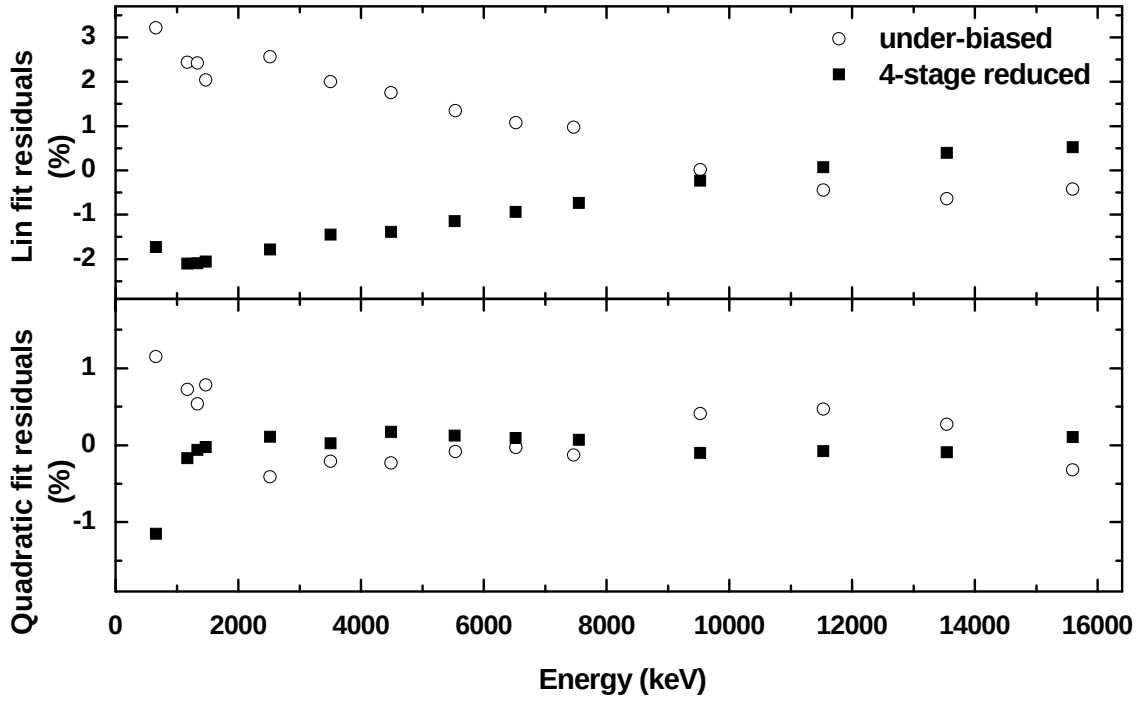

Fig. 7 – 3″×3″ $LaBr_3$ residuals of linear (top) and quadratic fits (bottom) for the two configurations.

As can be seen from Fig. 5, at the highest gamma-ray energies, the intrinsic beam energy spread causes the photopeak, the 511 keV escape peak and the Compton edge to overlap, reducing the capability of determining the peak centroid. For this reason, the first escape peaks have not been included in the proportionality studies. A derivative analysis has been applied to estimate the centroids for the 13.5 MeV and 15.5 MeV photopeaks. Peak channel position vs. energy is plotted in Fig. 6 for the two configurations.
In Table 5 we give the FoM for linear (1 coefficient) and quadratic (3 coefficients) fits while Fig. 7 shows the residuals for the two configurations. Residual and FoM values are evaluated using Eq. (2) and Eq. (3) respectively.

Table 5 – FoM values after linear and quadratic fits for the two 3″×3″ $LaBr_3$ configurations.

	FoM under-biased configuration	**FoM** 4-stage reduced configuration
1 coefficient linear fit	21.9	16.6
3 coefficients quadratic fit	5.8	2.4

Response proportionality can also be evaluated in terms of photon energy divided by peak channel position, plotted against photon energy. This represents the measured energy divided by the actual energy, which for an ideally linear detector would be a horizontal straight line. Fig. 6 shows this evaluation of proportionality, for the two configurations, normalised with its average. The maximum deviation from a straight line is 3.9% for the under-biased base and 2.6% for the 4-stage reduced base. PMT instabilities due to temperature and HV supply fluctuations are typically of the order of 1 % to 2 % so that the evaluation may be partially affected by these fluctuations. Nevertheless, the two configurations show different behaviours. The under-bias configuration shows an increase in the ratio measured-energy / actual-energy at higher energies, while the 4-stage reduced configuration shows a decreasing ratio - consistent with a loss of proportionality because of photocathode saturation.

4.2 Energy resolution

The analysis of the energy resolution is based on the experiments that we have carried out at LNS in Catania, since, unlike the gamma-rays generated at HIγS, there is not intrinsic spreading in energy. An investigation of the energy resolution from HIγS data is also ongoing, specifically modelling the broadened response taking into account photopeak, Compton edges and pair production.
Fig. 8 shows examples of spectra collected at LNS up to 15.1 MeV with the 4-stage reduced configuration and PMT HV bias of 400 V. The determination of the FWHM is also schematically shown and is based on the method described in [40]. This is simply the interpolation of the peak channel corresponding to half of the photopeak maximum once the background is subtracted. In our case this includes the Compton edge. Fig. 9 and Table 6 show the energy resolutions found for the two configurations. These were evaluated from spectra covering the entire energy range and containing all the available gamma-ray lines (Fig. 8). The relatively low gain and high background for the 662 keV line are the reason why, for both configurations, its energy resolution is slightly higher than the one recorded in our laboratory (Fig. 3).
The specific energies at which we have evaluated the energy resolution are shown in Table 4 (right) with the exception of Am-Be line at 4436 keV which has an intrinsic width much larger than the detector energy resolution, more likely because of Doppler broadening. The HPGe spectrometer gave an intrinsic energy width of ~100 keV FWHM for this line.
The 4-stage reduced configuration offers a better energy resolution, 3.1 % at 662 keV and 0.9% at 15.1 MeV against 3.4% and 1.3%, respectively, measured with the under-biased configuration. Both configurations show a deviation from a

$E^{-0.5}$ curve at high energy (see dotted lines in Fig. 9) indicating the presence of a second component, in addition to the statistical term, affecting the energy resolution. In [40] a simplified model for the measured energy resolution, R_{tot}, is obtained taking into consideration the two main components. It has the form:

$$(R_{tot})^2 = (R_{stat})^2 + (R_{const})^2 \tag{4}$$

where R_{stat} is the statistical contribution to energy resolution proportional to $E^{-0.5}$ and R_{const} a constant term representing the whole contribution from spectrometer non-idealities. For the energy resolution measured in percent, the two components of R_{tot} can be expressed as [41,42]:

$$(R_{tot})^2 = \left(100 \times 2.355 \times \sqrt{\frac{1+\nu}{PY}}\right)^2 + (constant)^2 \tag{5}$$

where ν is the fractional variance of the multiplication process and PY the photoelectric yield, which implicitly is a function of the energy. From our preliminary testing we have found $PY \sim 19.5 \times E(keV)$ for both configurations. However, the resolution formula in Eq. (5) fails to fit the observed energy resolution for the under-biased configuration within the errors and does not fit the 4-stage reduced case particularly well either. This resolution fit is reported in Fig. 9 as bold lines for both configurations.

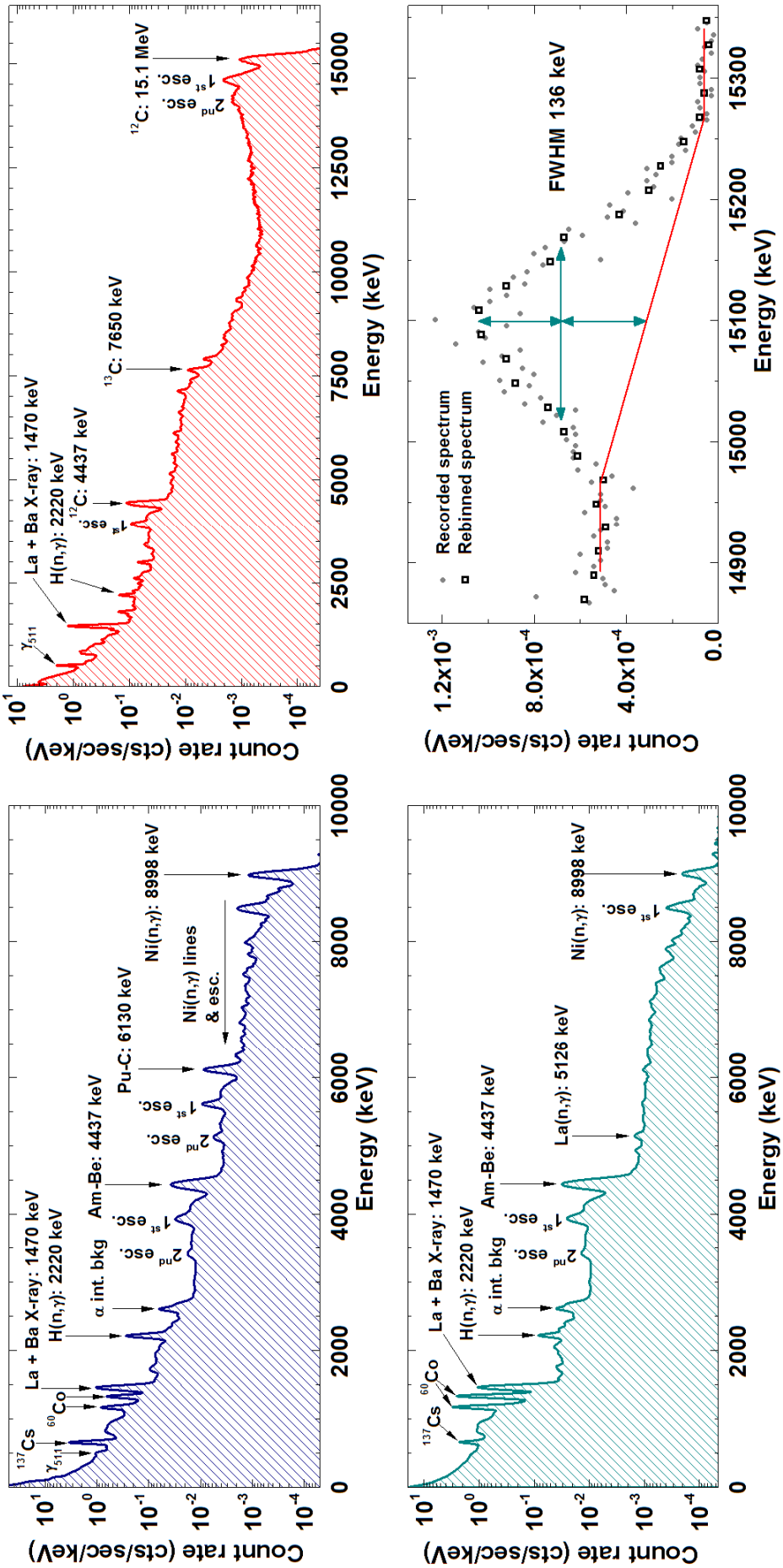

Fig. 8 – The gamma-ray spectra collected with a 3″×3″ $LaBr_3$ using the 4-stage reduced configuration with the PMT HV bias of 400 V. From bottom left and clockwise: spectra collected at HIγS, spectra collected at LNS including the PuC 6.130 MeV line, spectra with the mono-energetic 15.1 MeV from nuclear excitation of ^{12}C, the method adopted for FWHM determination. Similar spectra have been collected with the under-biased configuration.

Table 6 – Measured energy resolution vs. photon energy for the two 3″×3″ $LaBr_3$ and two 2″×2″ $LaBr_3$ configurations.

	3″×3″ - Photonis PMT		**2″×2″ - Hamamatsu PMT**	
	under-biased	**4-stage reduced**	**under-biased**	**4-stage reduced**
	PMT HV = 450 V	PMT HV = 400 V	PMT HV = 500 V	PMT HV = 300 V
Energy (keV)	**Energy resolution FWHM (%)**			
661.66	3.45 ±0.09	3.05 ±0.05	3.05 ±0.10	3.20 ±0.10
1173.24	2.50 ±0.14	2.10 ±0.07	2.40 ±0.14	2.40 ±0.07
1332.5	2.40 ±0.12	2.00 ±0.07	2.30 ±0.12	2.20 ±0.07
2223	1.90 ±0.10	1.60 ±0.05	1.75 ±0.10	1.65 ±0.05
5126	1.35 ±0.15	1.18 ±0.10	n/a	n/a
6130	1.26 ±0.15	1.10 ±0.10	1.30 ±0.15	1.20 ±0.10
8997	1.25 ±0.07	1.00 ±0.07	0.92 ±0.07	0.95 ±0.10
15100	1.29 ±0.11	0.93 ±0.12	n/a	0.80 ±0.10

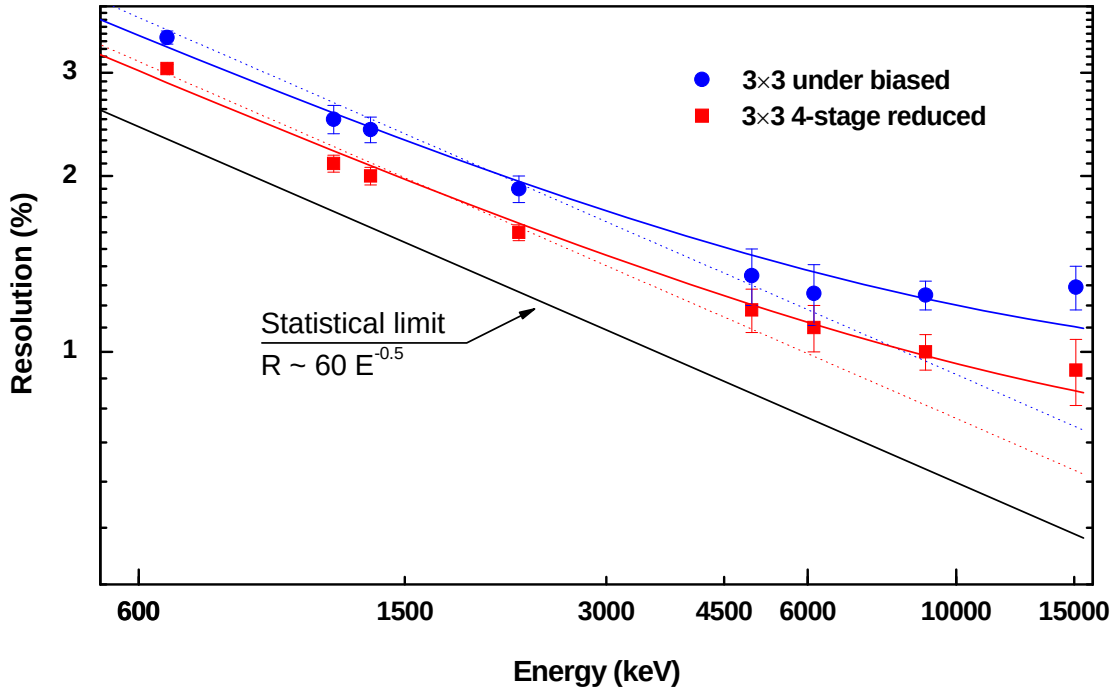

Fig. 9 – Energy resolution vs. photon energy for the two 3″×3″ $LaBr_3$ configurations. The dotted lines represent best fits with a purely statistical energy resolution in the form $\propto E^{-0.5}$ while the bold lines represent best fits with an energy resolution in the form of Eq. (4). PMT HV biases are 450 V for the under-biased configuration and 400 V for the 4-stage reduced configuration, i.e. the same biases used for the HIγS experiments.

In Table 7 we report the fit parameters and the fractional variance compatible with the measured PY of 19500 phe/MeV. The two values found show a contribution from statistical fluctuations higher than expected from the PMT datasheet as listed in Table 3. For the 4-stage reduced, it could be caused by using a dynode to collect the electrons.

Table 7 – Results from the energy resolution fit of the two 3″×3″ $LaBr_3$ configurations. The reported fractional variance is estimated from the fit parameters and the values already found for the light yield. The values correspond to a photon energy expressed in keV.

	R_{stat} [%]	$1+\nu$	R_{const} [%]	R_{tot} [%]
under-biased	$83.3/\sqrt{E}$	2.4	0.9	$\sqrt{\left(83.3\,E^{-0.5}\right)^2+(0.9)^2}$
4-stage reduced	$74.3/\sqrt{E}$	1.9	0.5	$\sqrt{\left(74.3\,E^{-0.5}\right)^2+(0.5)^2}$

The PMTs used are characterized by very close values of cathode blue sensitivity of nearly 14 (μA/Lm-410 nm) roughly corresponding to a QE at 380 nm of about 35%. This is consistent with the PY measurement showing a PY of ~20000 phe/MeV, i.e. 19500 phe/MeV for the 3″×3″ and 20.500 phe/MeV for the 2″×2″. In fact, *light output × quantum efficiency × collection efficiency = 60000 × 0.35 × 0.9 = 19000 phe/MeV.*
A purely statistical resolution function with fractional variance $1+\nu=1.25$ and $PY=19000\ phe/MeV$ can be evaluated as:

$$\left(\frac{\Delta E}{E}\right)_{\%}=100\times 2.355\sqrt{\frac{1+\nu}{PY}}=100\times 2.355\sqrt{\frac{1.25}{19\,E}}=60.4/\sqrt{E} \qquad (6)$$

with *E* expressed in keV [41,42]. This function, plotted in Fig. 9, represents the optimum energy resolution of an ideal $LaBr_3$/PMT assembly and corresponds to a resolution value of 2.3%. at 662 keV. The energy resolution achieved with the 4-stage reduced configuration is closer to this limit than the under biased configuration.

4.3 Result with 2″×2″ $LaBr_3$

We also report measurements with a smaller 2″×2″ $LaBr_3$ coupled to a Hamamatsu PMT, i.e. same that in Chapter 4. This assembly was also tested in two configurations, but, in this case, the under-biased configuration was tested at HIγS, while the 4-stage reduced configuration was tested at LNS. For this reason the data points are different in the studies of linearity, while for the under-bias configuration the 15.1 MeV point for the energy resolution is not available. As for the 3″×3″ configurations we have first set the operational bias to optimise both response proportionality and the energy resolution.
For the 2″×2″ under-biased configuration we have chosen a PMT bias of 500 V (instead of the 450 V used for the 3″×3″) for which we measured an energy resolution of 3% at 662 keV. In order to optimize energy resolution, we used a higher bias than what we expected to use from previous experience ([11] and Chapter 4), mainly because of an increase in environmental noise and a long cable driving the signal. The 4-stage reduced configuration has been operated at 300 V (instead of the 400 V used for the 3″×3″) with an energy resolution of 3.2% at 662 keV.
Response proportionality data are shown in Fig. 10 and Fig. 11. Apart the different energy of the data point used for the two configurations, their proportionality curves are very similar.

The measured energy resolutions for the two 2″×2″ configurations substantially overlap in the range 600 keV - 9 MeV so that using a reduced stage configuration yields no benefit. Energy resolution fit parameters are reported in Table 8 and apply to both 2″×2″ configurations. For the 4-stage reduced configuration the energy resolution at 15.1 MeV measures 0.8% as shown in Table 6 and Fig. 12. Recently, Ciemala et al. [12] have found similar energy resolution with their 2″×2″ $LaBr_3$ assembly.

Table 8 – Results from the energy resolution fit with the 2″×2″ configurations. As for the 3″×3″ (Table 7) the reported fractional variance is estimated from the fit parameters and the values already found for the light yield.

	R_{stat} [%]	$1+\nu$	R_{const} [%]	R_{tot} [%]
4-stage reduced and under-biased	$80.3/\sqrt{E}$	2.4	0.4	$\sqrt{\left(83.3\,E^{-0.5}\right)^2+(0.35)^2}$

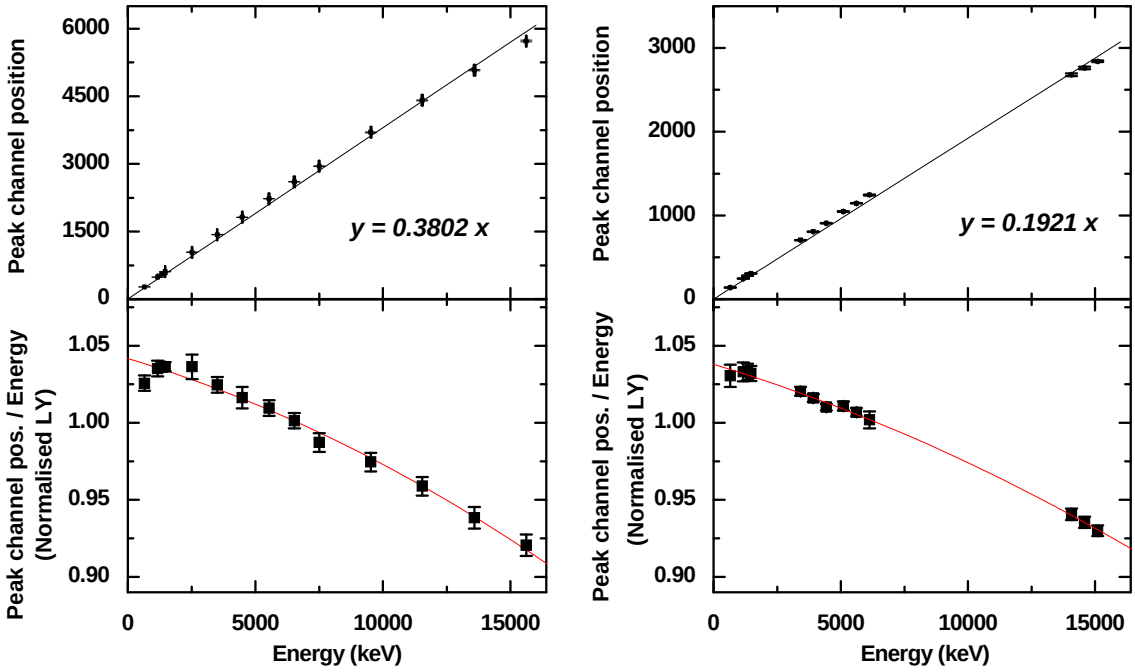

Fig. 10 – Proportionality of a 2″×2″ $LaBr_3$ crystal coupled with a 2″ Hamamatsu PMT and for the two voltage divider configurations: under-biased configuration (left) and 4-stage reduced configuration (right). PMT HV biases are 500 V for the under-biased configuration and 300 V for the 4-stage reduce configuration.

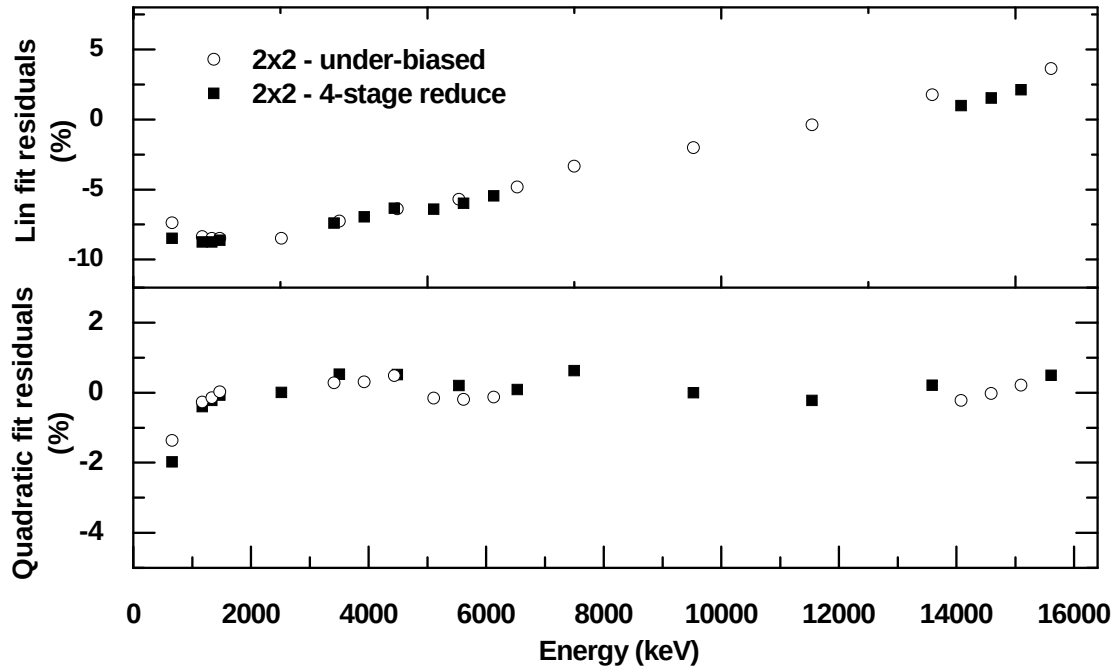

Fig. 11 – Proportionality of a 2″×2″ $LaBr_3$ crystal coupled with 2″ Hamamatsu PMT and for the two voltage divider configurations. Residuals of a 1-coefficient linear fit –top, and 3-coefficients quadratic fit -bottom.

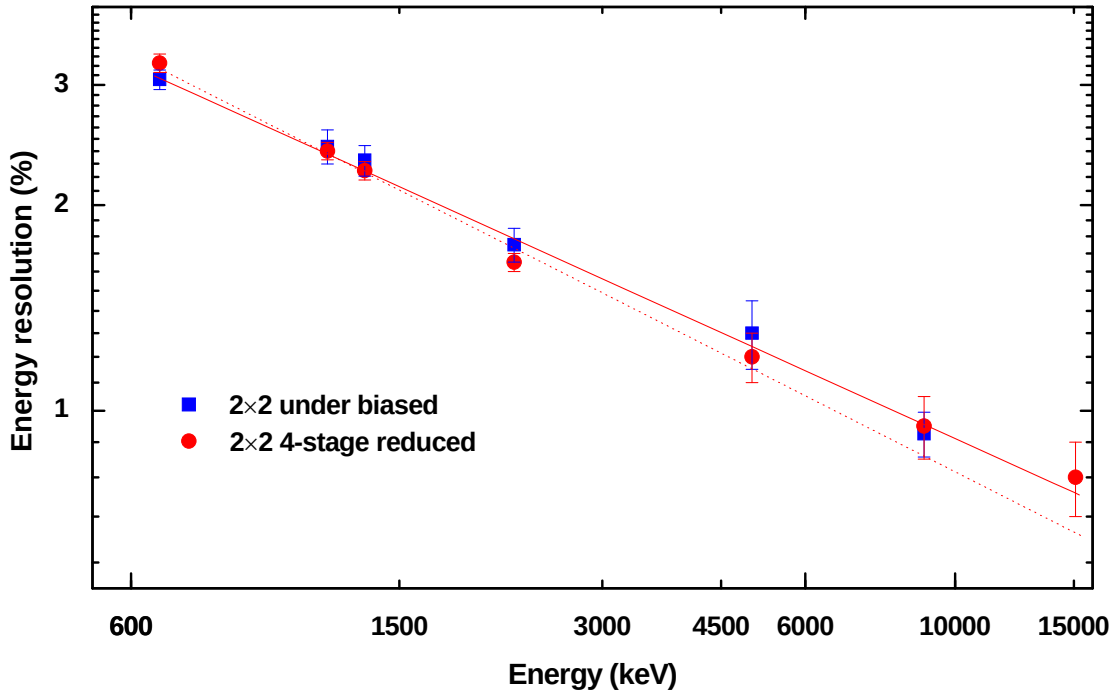

Fig. 12 – Energy resolution of a 2″×2″ $LaBr_3$ crystal coupled with 2″ Hamamatsu PMT and for the two kinds of configurations. Dotted and bold lines have the same meaning as in Fig. 9. Since the best fits below 8997 MeV substantially overlap for the two configurations, for clarity, we have plotted only those found for the 4-stage reduced configuration.

4.4 In-flight calibration capabilities

We have applied a simple procedure to verify the configurations that can be calibrated using the ^{138}La gamma-ray line. This procedure will be particularly useful during the operation of BepiColombo to provide a reliable first approximation of the instrument energy calibration. A two-point calibration, using the baseline (0-energy equals to 0-channel) and the self activity line at 1470 keV, was constructed, and an estimation of the errors in calibration across the entire energy range is defined as the actual energy minus the estimated energy. In other words, we have extended the calibration using the 1470 keV line up to 15 MeV without further correction and estimated its correlation with experimental data, with results shown in Fig. 13. The two 3″×3″ configurations are able to predict the actual energy with an error of < 200 keV at 9.5 MeV (1.8 % for the 4-stage reduced configuration and 2.1% for the under-biased configuration). At the same energy, 9.5 MeV, the calibration of both 2″×2″ configurations is off by about 600 keV, ~6% error.

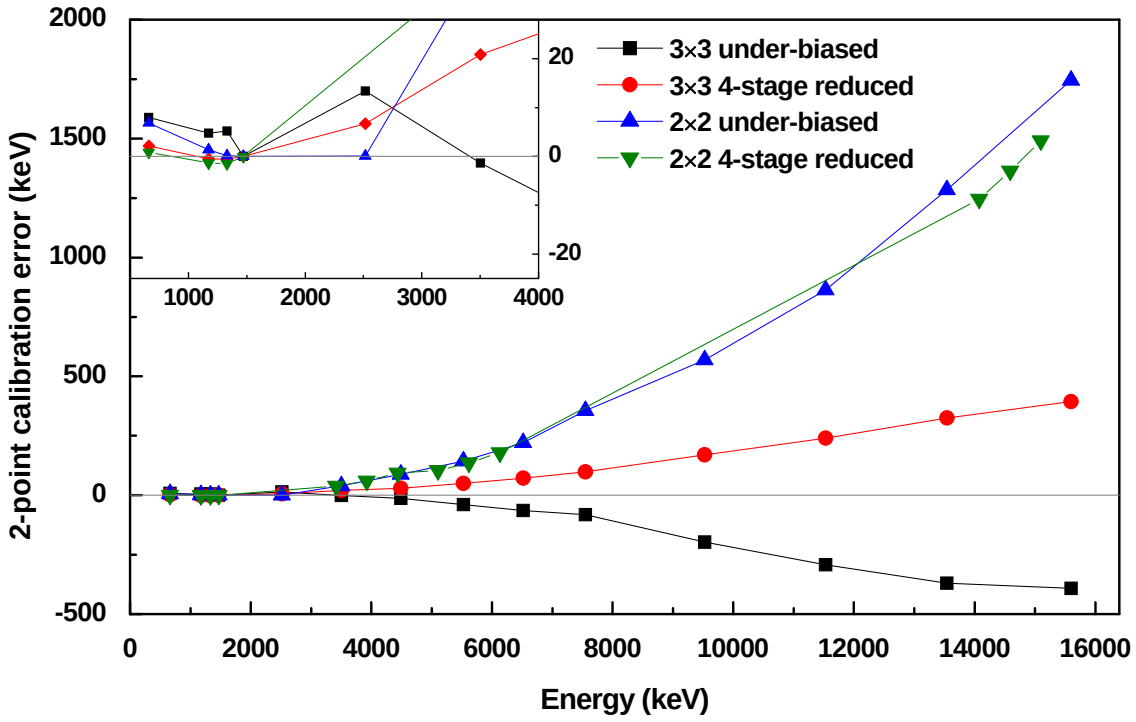

Fig. 13 – Comparison of a 2 point calibration (0 energy 0 channel and 1470 keV internal background) with the actual saturated proportionality of a 2″×2″ $LaBr_3$ crystal coupled with 2″ Hamamatsu PMT.

4.5 Summary of results

For the 3″×3″ assemblies, the use of a 4-stage reduced configuration slightly improves the response linearity and calibration capability. The same is not the case for the 2″×2″ assemblies. In spite of the much lower PMT gain (see Table 3), the 2″×2″ 4-stage reduced configuration shows very similar saturation behaviour to the 2″×2″ under-biased configuration. This suggests that the response of our Hamamatsu 2″ PMT is mainly affected by photocathode saturation which produces much the same effects in both configurations.
The slope of the residuals curves (Fig. 7 and Fig. 11) and ratio peak channel / photon energy (Fig. 6 and Fig. 10) are similar for the two 2″×2″ configurations and the 3″×3″ 4-stage reduced, suggesting that all three configurations are limited by photocathode saturation and that the 2″×2″ assembly suffers the most - with a maximum deviation of about 15% over the whole dynamic range, against the 2% for the 4-stage reduced configuration. The behaviour of the 3″×3″ under-biased (Fig. 6 – left) can be explained considering that even for the lower photon energies (<5 MeV) the spectrometer is affected by anode peak current saturation. At higher photon energies, the photocathode also begins to saturate, reducing the number of photoelectrons reaching the 1st dynode and being multiplied. In this way, the photocathode saturation compensates for the higher current that would flow in the PMT, giving rise to an over-linearity and to an apparent more proportional response.
We can operate our 3″×3″ and 2″×2″ spectrometers with energy resolution of at least 3.4% at 662 keV and 1.3% at 8997 MeV. This surpasses BepiColombo requirements (4.5% at 662 keV). Moreover we still have room for further optimization of energy resolution and response linearity as well.
All assemblies present a deviation from a purely statistical limited energy resolution above 5 MeV. This deviation is stronger for the 3″×3″ assemblies than the 2″×2″ assemblies. The energy resolution of both 2″×2″ and 3″×3″ assemblies is well represented by a function in the form of Eq. (5). Compared to the 2″×2″ assemblies, for the 3″×3″ assemblies a larger constant term is necessary to successfully fit our data. In addition, for the 3″×3″ assemblies, the constant term is larger for the under-biased configuration than for the 4-st reduced one. Such behaviour of the constant term could arise from both intrinsic crystal non-homogeneities of the light yield and non optimal multiplication statistics at high photon energy.
Normally we can expect the multiplication variance to be uniform over the entire energy range, i.e. independent from the total amount of electrons generated and multiplied in the PMT. This assumption is not confirmed for our two configurations. In the case of the under-biased configuration, the low electric field between dynodes could be insufficient to keep all the electrons in their trajectories. For the 4-stage reduced configuration, it is the electron collection process that is problematic because of the double use of the 4th dynode.

The energy resolution extra term can be approximately identified by a non constant fractional variance term that varies with photon energy. This term increases from 1.5 at 662 keV up to 2.5 - 3.0 at 15 MeV, reflecting the approach of the PMT functional limit at that energy. As consequence the R_{stat} would become a more complex function of the photon energy than a simple function of $E^{-0.5}$.

5 Final remarks

Laboratory data and measurement campaigns show how spectrometers based on $LaBr_3$ crystals coupled to PMTs are difficult to optimize because of the characteristic $LaBr_3$ scintillation process, which stress PMTs close to their operational limits. However, successful techniques can be applied to enhance spectroscopic performance especially in the case of PMTs built by Photonis. The achieved performances confirm the superiority of $LaBr_3$ as well for high energy gamma-ray detection putting it at the top-of-the-range among scintillators for spectroscopy applications. In addition its radiation tolerance makes $LaBr_3$ an ideal choice for space application, in particular for those missions implemented with a strict resource budget and with a high need for radiation tolerance such as BepiColombo and the more recently proposed Laplace/JUICE mission to the Jovian system.

Moreover, during a recent workshop held in Milan, Italy, [43] it has been possible to observe the wide interest growing around $LaBr_3$ spectrometers in various research fields ranging from intermediate energy nuclear physics to fusion technology and ground based astrophysics. Also for these disciplines saturation problems are reported, either, as in our case, because of the need for high energy gamma-ray detection, or because of high count rate operation. Of particular interest is the recent result from Crespi et al. [44] showing the discrimination capability of $LaBr_3$ between gamma-rays and alpha particles. The extension of this capability to protons is under investigation mainly because it could enhance the sensitivity of $LaBr_3$ spectrometer making possible to partially suppress the internal and external background due to charge particles.

Unfortunately, in 2009 Photonis announced the closing down of its PMT business operations. Part of its catalogue may still be available through stock reserve, but no further development can be discussed. In any case, for BepiColombo, the PMT used onboard for the $LaBr_3$ spectrometer is already delivered. The experimental data have shown us how to reduce the number of active stages optimizes the spectroscopic performance in terms of response

proportionality and energy resolution for this kind of PMT. This solution could be further improved by designing a PMT with a limited number of active stages including a proper collecting anode and a high current photocathode.
In the case of Hamamatsu PMTs, the data show how, together with an improved PMT design, a different photocathode is needed in order to avoid saturation. Ankowski et al. [29] propose an almost transparent metal deposition able to reduce the unwanted effect of photocathode resistivity. This solution is worth exploration, and the main concern would be the possible loss of QE.
Since PMT and photocathode implementation might be not trivial, we could consider another option to further reduce saturation: making the scintillation process slower by decreasing its Ce concentration. The standard $LaBr_3$ crystals from Saint Gobain are 5% doped with Ce and reducing the doping down to 0.5% would make the scintillation process about twice as slow [45] with the final effect of reducing photocathode and anode currents to about half.
We are setting up direct measurements of the multiplication variance, using laser light pulses of wavelength, intensity and duration equivalent to that of $LaBr_3$. These measurements will be able to quantify the possible contribution of a non uniform variance and consequentially those due to non proportionality at high energy intrinsic to $LaBr_3$ crystals. Depending on the results we can expect a further optimization, reducing the gap between measured energy resolution and that expected on purely statistical grounds.
Nowadays alternative solutions to PMT are available as silicon photomultipliers (SiPMs) and silicon drift detectors (SDDs). SiPMs are available in large area devices of about 2.5″ diameter. Developments of these new technologies are on-going for their application in large crystals. Of most concern for their actual application to space missions is the radiation robustness of these devices.

References

[1] www.lns.infn.it

[2] www.tunl.duke.edu/higs/

[3] E.V.D. van Loef et al., "High-energy-resolution scintillator: Ce activated $LaBr_3$", Appl. Phys. Lett., 79 (2001) 1573.

[4] A. Owens et al., "Assessment of the radiation tolerance of $LaBr_3$:Ce scintillators to solar proton events", Nucl. Instr. and Meth. A 572 (2007) 785.

[5] W. Drozdowski et al., "Effect of Proton Dose, Crystal Size, and Cerium Concentration on Scintillation Yield and Energy Resolution of $LaBr_3$:Ce", IEEE Trans. Nucl. Sci., 54 (2007) 736.

[6] I.G. Mitrofanov et at., "The Mercury Gamma and Neutron Spectrometer (MGNS) on board the Planetary Orbiter of the Bepi Colombo mission", Planetary and Space Science, 58 (2010) 116.

[7] S. Kraft et al., "Development and Characterization of Large La-Halide Gamma-Ray Scintillators for Future Planetary Missions", IEEE Trans. Nucl. Sci., 54 (2007) 873.

[8] D. Rothery et al., "Mercury's surface and composition to be studied by BepiColombo", Planetary and Space Science 58 (2010) 21.

[9] Nicolini et al., "Investigation of the properties of a 1″×1″ $LaBr_3$:Ce scintillator", Nucl. Instr. and Meth. A 582 (2007) 554.

[10] P. Dorenbos et al., "Gamma Ray Spectroscopy With a 19×19 mm^3 $LaBr_3$: 0.5% Ce^{3+} Scintillator", IEEE Trans. Nucl. Sci. NS-51 (2004) 1289.

[11] F. Quarati et al. "X-ray and gamma-ray response of a 2″2″ $LaBr_3$:Ce"scintillation detector", Nucl. Instr. and Meth. A 574 (2007) 115.

[12] M. Ciemala et al. "Measurements of high-energy γ-rays with $LaBr_3$:Ce detectors", Nucl. Instr. and Meth. A 608 (2009) 76.

[13] G. Bizarri et al., "Scintillation Properties of Ø 1×1 $Inch^3$ $LaBr_3$:5%Ce_3^+ Crystal" IEEE Trans. Nucl. Sci. NS-53 (2006) 615.

[14] Saint Gobain Crystals and Detectors Technical Literature, "Physical Properties of Common Inorganic Scintillators". *Available online from*: www.detectors.saint-gobain.com

[15] S. Derenzo, http://scintillator.lbl.gov/

[16] G. Knoll, "Radiation Detection and Measurements", third ed., Wiley & Sons Ltd, New York, 2000.

[17] "Photomultiplier tubes, basics and applications", Hamamatsu Photonics, 3rd ed., 2007. *Available online from*: www.hamamatsu.com

[18] http://sales.hamamatsu.com

(http://sales.hamamatsu.com/en/inprint/inprint-2008/qe-pmt.php)

[19] K. Nakamura et al., "Latest bialkali photocathode with ultra high sensitivity", Nucl. Instr. and Meth. A 623 (2010) 276.

doi:10.1016/j.nima.2010.02.220

[20] M. Suyama and K. Nakamura "Recent progress of photocathodes for PMTs ", in proceedings of "International Workshop on New Photon Detectors, Japan, June 2009", PoS(PD09)013. *Available online from* http://pos.sissa.it/

[21] www.photonis.com

(http://www.photonis.com/upload/industryscience/pdf/pmt/XP5301.pdf)

[22] M. Kapusta et al. "Breakthrough in quantum efficiency of bi-alkali photocathodes PMTs", IEEE Nuclear Science Symposium Conference Record 2007, N06-2.

[23] R. Mirzoyan, M. Laatiaoui, M. Teshima, "Very high quantum efficiency PMTs with bialkali photo-cathode", Nucl. Instr. and Meth. A. 567 (2006) 230.

[24] www.rug.nl/kvi

[25] "Photomultiplier Manual", RCA Corporation, 1970.

[26] R.D. Hiebert et al., "Photomultiplier tube base for high pulsed anode currents", Nucl. Instr. and Meth. 142 (1977) 467.

[27] V. A. Kalinnikov et al., "A Small-Power Transistor Divider for Photomultiplier Tubes", Instruments and Experimental Techniques, 2006 (49) 223.

[28] S.O. Flyckt and C. Marmonier, "Photomultiplier tubes: principles & applications", Photonis, 2002.

[29] A. Ankowski et al., "Characterization of ETL 9357FLA photomultiplier tubes for cryogenic temperature applications", Nucl. Instr. and Meth. A 556 (2006) 146.

[30] H. M. Araujo et al., "Low temperature performance of photomultiplier tubes illuminated in pulsed mode by visible and vacuum ultraviolet light", Rev. Sci. Instrum. 68 (1997) 35.

[31] Saint Gobain Crystals and Detectors - http://www.detectors.saint-gobain.com/

[32] www.cremat.com

[33] www.amptek.com

[34] www.bertan.com

[35] www.iseg-hv.com

[36] M. Bertolaccini et al., "A technique for absolute measurement of the effective photoelectron per keV yield in scintillation counters", presented at the Nucl. Electr. Symp., Versailles, France, Sep. 1968.

[37] J.T.M. de Haas and P. Dorenbos, "Advances in Yield Calibration of Scintillators", IEEE Trans. Nucl. Sci., 55 (2008) 1086.

[38] H. R. Weller et al, "Research opportunities at the upgraded HIGS facility", Progress in Particle and Nuclear Physics, 62 (2009) 257.

[39] J.G. Rogers et al, "A 7–9 MeV isotopic gamma-ray source for detector testing", Nucl. Instr. and Meth. A 413 (1998) 249.

[40] G. Gilmore, "Practical Gamma-ray Spectroscopy", Wiley & Sons Ltd, 2nd ed., 2008.

[41] E. Breitenberger, "Scintillation spectrometer statistics", Progress in Nuclear Physics, 4 (1955) 56.

[42] P. Dorenbos et al., "Non-Proportionality in the Scintillation and the Energy Resolution with Scintillation Crystals", IEEE Trans. Nucl. Sci., 42 (1995) 2190.

[43] Workshop on Developments of new Scintillator Detectors for Gamma Spectroscopy and Imaging, November 16 – 17, 2009, Milano, Italy.

http://www.mi.infn.it/labr2009

[44] F.C.L. Crespi et al., "Alpha–gamma discrimination by pulse shape in $LaBr_3$:Ce and $LaCl_3$:Ce", Nucl. Instr. and Meth. A 602 (2009) 520.

[45] J. Glodo et al "Effects of Ce Concentration on Scintillation Properties of $LaBr_3$:Ce", IEEE Trans. Nucl. Sci., 52 (2005) 1805.

Chapter 6

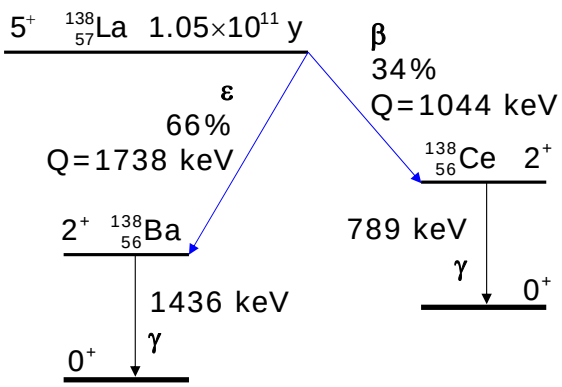

Study of ^{138}La radioactive decays using $LaBr_3$ scintillators

We present a detailed investigation of the intrinsic activity of $LaBr_3$ scintillators from the natural abundance of radioactive isotope ^{138}La. Compared to earlier studies of lanthanum halides intrinsic activity, we gained a sharper insight by using samples of different sizes, ranging from 0.16 cm^3 to 347 cm^3, and by applying recent results on the non-proportionality of scintillation response. In addition, we took advantage of the fact that $LaBr_3$ spectrometers offer a unique

opportunity, never available before, to study the characteristics of the ^{138}La electron capture and β radioactive decays that are 2nd order unique forbidden transitions. The observed shape of the β continuum, measured down to the energy of 2 keV, is found to be different than expected from standard nuclear theory, indicating a possible underestimation of the screening effect for β energies below 75 keV.

With reference to the list of publications the content of this chapter is based on publication 1, i.e.:

Quarati, F.G.A., Khodyuk, I.V., van Eijk, C.W.E., Quarati, P., Dorenbos, P.
Study of ^{138}La radioactive decays using $LaBr_3$ scintillators
Nucl. Instr. and Meth. A 683 (2012) 46

DOI: 10.1016/j.nima.2012.04.066

1 Introduction

Lanthanum halides scintillators are characterized by an intrinsic activity that poses a serious limit for their application in low count rate experiments [1]. This activity has two origins: the contamination due to the radioactive isotope ^{227}Ac and its daughters and the presence of the radioactive isotope ^{138}La. In scintillation pulse height spectra, the contamination due to ^{227}Ac and daughters manifests itself as α particle detection with γ-ray equivalent energy above ~1.6 MeV and below ~3 MeV [2], whereas ^{138}La activity dominates the spectral region below ~1.6 MeV.

Successful efforts have been made to reduce the ^{227}Ac contamination [2], [3], e.g. through raw material purification. However, no simple solution is available to reduce the presence of ^{138}La, which is the only naturally occurring radioactive isotope of lanthanum, with 0.0902% abundance and 1.05×10^{11} yrs half-life [4]. ^{138}La decays by electron capture (ε) into ^{138}Ba with 66.4% probability and for the remaining 33.6% by β-decay into ^{138}Ce [4]. In both cases, ^{138}La decays into an excited state of the daughter nucleus with consequent emission of de-excitation γ-rays, of 1436 keV for ^{138}Ba (ε-decay) and 789 keV for ^{138}Ce (β-decay).

Lanthanum halide scintillators, namely $LaBr_3$:Ce and $LaCl_3$:Ce, show very similar behavior in terms of intrinsic activity and, in principle, the results obtained with one of them are directly applicable to the other. In this work we only studied $LaBr_3$.

In our investigation we concentrated on the spectral energy region below ~1.6 MeV dominated by the detection of ^{138}La decay products and did not further study the α activity. Results show that ^{138}La decays account for almost all intrinsic activity events detected below ~1.6 MeV, with the only exception of a contribution from ^{40}K. This nuclide is also found in the photomultiplier tubes (PMT), and, to some extent, it can be considered part of the intrinsic activity.

Our results differ from those reported in [5]-[7] by making use of various crystal sizes. This allowed us to compare pulse height spectra where the contributions from x-, γ- and β-rays have a different impact on the shape of the intrinsic activity pulse height spectrum because of their specific attenuation lengths and escape probability. In addition we applied recent results on non-proportionality of the scintillation response (nPR) [8] achieving a fine calibration of the intrinsic activity pulse height spectrum. In our study, we exploited the fact that $LaBr_3$ scintillators offer a unique opportunity, never available before, to collect detailed data on the ^{138}La radioactive decay which is due to a 2nd order unique forbidden transition.

In addition to [3], we recorded the β continuum in coincidence with the escaping

789 keV γ-rays from ^{138}Ce de-excitation down to the very low energy of 2 keV, and found that, below 75 keV, the experimental data do not agree with standard nuclear theory, possibly because of an underestimation of the screening effect for β energies below 75 keV. Indeed, $LaBr_3$ appears an ideal detector for β-decay study of ^{138}La, because the energy of the β particles is totally dissipated within the scintillator without any energy loss in dead layers.
In Section 2 of this work we first describe the experimental setup and the activity measurements carried out. In Section 3 we present the experimental determination of the β continuum. In Section 4 we compare the experimental β continuum with the theoretical one.

2 Experimental setup and intrinsic activity measurements

A set of four $LaBr_3$: 5%Ce crystals, all manufactured by Saint-Gobain Crystals [9], have been used to collect intrinsic activity spectra. All samples are Al-encapsulated, cylindrically shaped and equipped with a quartz window for optical coupling to the PMT. Dimensions of the samples are reported in Table 1.

Table 1 – Dimensions of the right cylindrical shaped samples used.

Sample	Diameter mm (inches)	Height mm	Volume cm^3
1	10 (~⅜″)	2	0.16
2	12.7 (0.5″)	12.7	1.61
3	25.4 (1″)	25.4	12.9
4	76.2 (3″)	76.2	347

In addition, a 12.9 cm^3 $CeBr_3$ sample [10], equivalent in dimensions to $LaBr_3$ sample 3, has been used as coincidence detector to collect the β continuum.
For each crystal, two intrinsic activity pulse height spectra have been taken, the first covering the energy range from 9 keV to 3 MeV and the second covering the energy range from 0 to 150 keV.

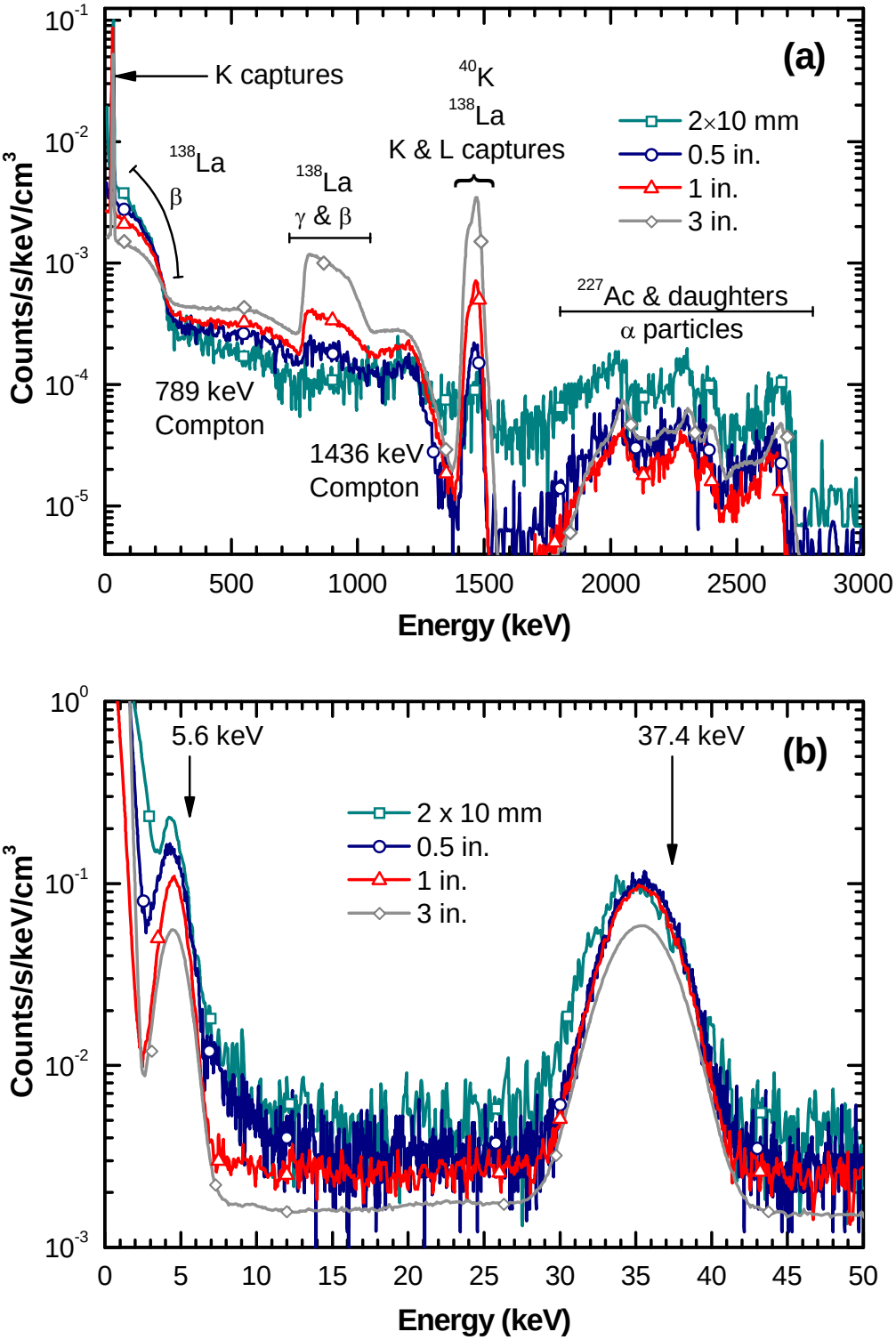

Fig. 1 - Intrinsic activity spectra collected with the set of 4 $LaBr_3$ samples in Table 1. (a): the spectra collected with an energy range from 9 keV to 3 MeV. (b): the spectra collected with an energy range from 0 to 150 keV where the 122 keV peak from ^{57}Co was used for energy calibration. Only the energy range of interest from 0 to 50 keV is shown. The arrows indicate the nominal energies of the L and K cascade peaks while their detection occurs at 4.5 keV and 35.5 keV, respectively, because of the effect of the nPR. No coincidence condition was used to acquire these measurements.

All pulse height spectra have been taken with the scintillator optically coupled to a PMT and placed inside a low-activity lead castle in order to reduce the environmental contribution to the intrinsic activity. Both spectra, for every crystal, are shown in Fig. 1a and Fig. 1b. For the smallest sample the acquisition lasted 121 hrs for the widest energy range and 44 hrs for the 0 to 150 keV energy range. For the bigger samples, acquisition times of several hours were already sufficient to provide satisfactory counting statistics, i.e. well above 100000 counts.

2.1 Effect of scintillation non-proportional response (nPR)

Scintillation non-proportional response (nPR) provides an observable distortion from a linear energy calibration of the intrinsic activity spectra. A description of nPR for lanthanum halide scintillators, including an evaluation of its effect for both x-rays and electrons, is available in [8].

Spectra shown in Fig. 1b are calibrated using the ^{57}Co 122 keV γ-ray, assuming a proportional response with deposited energy. The spectra show two main peaks at equivalent energy of 4.5 keV and 35.5 keV. These two peaks, characteristic of ε-decays, originate from the energy released by the cascade products following the refilling of the hole, left behind by the captured electron, in the K- or L-atomic shell of the daughter nucleus ^{138}Ba. These two peaks are only observed in those cases when the 1436 keV γ-ray escapes from the crystal.

For ^{138}Ba, the K and L binding energies are 37.44 keV and 5.6 keV, respectively. The latter is taken as the weighed average of the L1, L2 and L3 shells. The M-shell binding energy averaged from M1 to M5 is 1.0 keV and the peak from M-shell electron capture is beyond the noise floor. All above values are taken from [11].

The refilling of holes in atomic shells does not proceed through in a unique mechanism. It involves x-ray emission or Auger electron emission or different combinations of both, and each individual cascade product is detected with a specific degree of nPR. For instance, after the capture of a K-shell electron, by far the most probable cascade is as follows. A Ba L-shell electron refills the K-shell hole releasing a 31.84 keV K_α x-ray, and then the created L-shell hole is refilled by Auger processes releasing the remaining 5.6 keV. We can apply the nPR data from [8] to predict the expected equivalent energy. This is the sum of the contribution from the 31.84 keV K_α x-ray with a 95.6% photon-nPR and of the 5.6 keV Auger electron with ~90% electron-nPR corresponding to a total of 35.5 keV equivalent energy, which matches with the experimental result (see Fig. 1b).

Note that, actually, not a single 5.6 keV Auger electron is emitted but one of 4.6 keV plus the energy deposited by the hole in the M-shell. A similar exercise can be done for the sequence of events following the capture of an L shell electron.
In summary, the energy of the two peaks in Fig. 1b is determined by the refilling processes characteristic of the ε-decay of ^{138}La but their equivalent energy, i.e. the energy that is detected by $LaBr_3$, because of nPR effects, is only 4.5 keV and 35.5 keV.

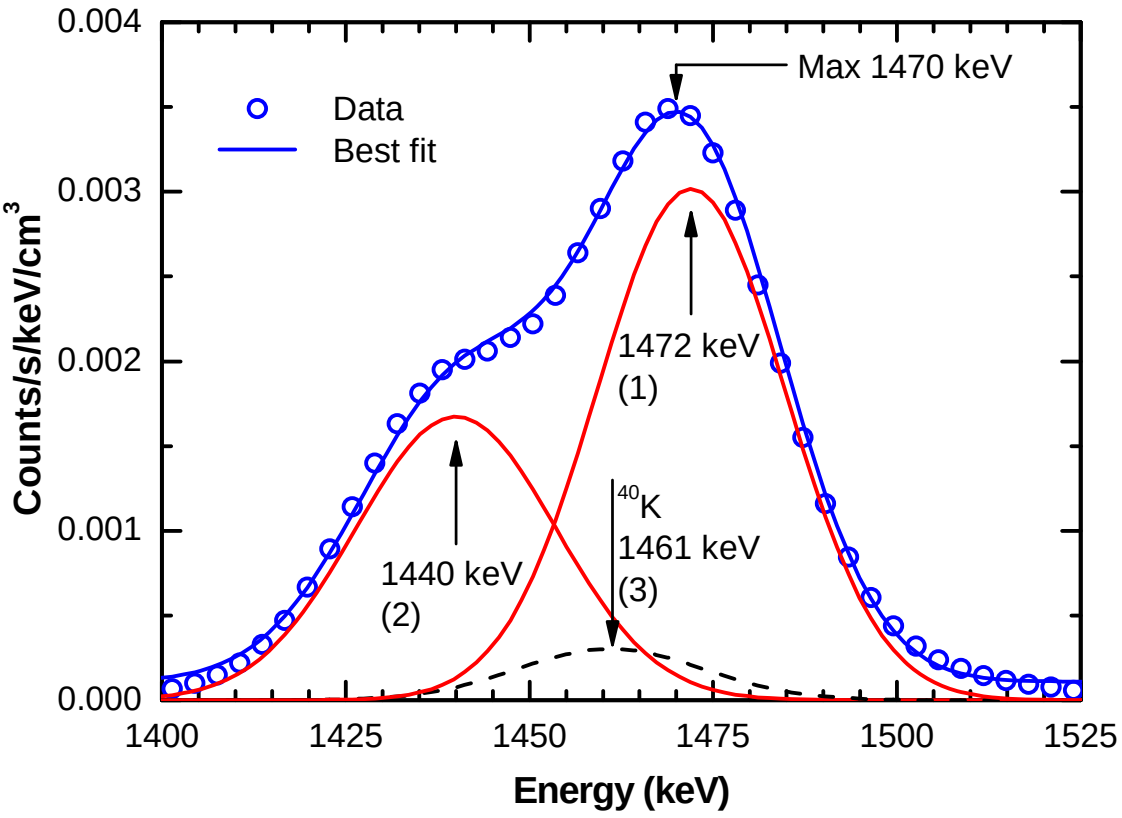

Fig. 2 - The spectral region of the intrinsic activity corresponding to the detection of the ^{138}Ba de-excitation 1436 keV γ-ray using sample 4. The peak is best fitted with the sum of 3 Gaussians: (1) 1436 keV + K cascade, (2) 1436 keV + L and M cascade and (3) 1461 keV from ^{40}K.

K and L cascade peaks are also detected in coincidence with the 1436 keV γ-ray of the ^{138}Ba de-excitation giving rise to a peak centered around 1472 keV (Fig 1a and Fig 2). The γ-ray energy adds to the energy of the K, L and M cascade peaks with their relative intensity and respective nPR. The 1472 keV peak (Fig 2) can be fitted using three Gaussian functions: (1) centered at 1440 keV corresponding to 1436 keV + L and M cascade; (2) centered at 1472 keV corresponding to 1436 keV + K cascade; (3) centered at 1461 keV and corresponding to ^{40}K contribution. The fit is carried out keeping the event ratio between ^{138}Ba de-excitation and ^{40}K contribution fixed. Activity measurements using a standard HPGe spectrometer

have confirmed that this ratio is ~10:1. Similar conclusions were reported in [3].

2.2 Activity measurements

From the analysis of the collected spectra we compiled Table 2 where the sample activities are reported for the energy regions dominated respectively by ^{138}La and ^{227}Ac decay, i.e. 0-1.6 MeV and 1.6-3.0 MeV. Activities are given in counts/s/cm^3, i.e. equivalent to Bq/cm^3.

Table 2 – Detected intrinsic activity with the $LaBr_3$ samples.
Error is ±5% with the exception of ^{138}La activity 0-1.6 MeV for sample 1, for which the error is ±10%. Average ^{138}La activity is 1.49 cts/s/cm^3, and 1.45 cts/s/cm^3 excluding sample 1 from the average.

Sample	Volume cm^3	^{138}La activity 2 keV-1.6 MeV counts/s/cm^3	^{138}La activity 9 keV-1.6 MeV counts/s/cm^3	^{227}Ac activity 1.6-3 MeV counts/s/cm^3
1	0.16	1.61	1.36	0.097
2	1.61	1.52	1.25	0.030
3	12.9	1.43	1.22	0.019
4	347	1.39	1.27	0.031

We expect to observe a constant ^{138}La activity independent of sample size. In fact, as we have seen in the previous sub-Section 2.1, during the ε decay of ^{138}La not only the 1436 keV ^{138}Ba γ-ray is emitted, but also the peaks corresponding to the cascade from the refilling of the hole left behind by the captured electron in one of the atomic shells. The smallest sample has almost no efficiency for detection of the 1436 keV γ-ray because of a high escape probability. Nevertheless we still count the occurring ε decays through the presence of the K and L cascade peaks. The same applies for the β-decays. If the 789 keV γ-ray from ^{138}Ce de-excitation escapes detection, still the emitted β particle is always detected. Therefore, even with the smallest sample, every ^{138}La decay contributes one count and one count only to the pulse height spectrum.
As can be seen in Fig. 1b, the electronic noise contribution to the spectrum allows

undisturbed detection of the K cascade peak whereas the L and M cascade peaks are, respectively, partially and totally merged with the noise. By fitting the first 10 keV part of the spectrum with a "Gaussian + exponential" function we determined the number of events that originates from L electron capture decays.
The total intrinsic activity has been evaluated merging the data from the two different spectral ranges acquired for each crystal. We evaluated measurement errors below ±5% for samples 2, 3 and 4 and about 10% for sample 1, which has the lowest signal to noise ratio because of its lowest count rate. In Table 2, 4th column, we report also the activities evaluated using exclusively the wide range spectra (Fig. 1a) which do not include L capture events.
Within experimental error, all samples show approximately the same ^{138}La activity, independently from their size. This does not apply to the ^{227}Ac activity. In fact its concentration depends on the geographical origin and contamination of the raw materials and varies upon purification processes.
We can compare the measured ^{138}La total activity with that calculated from its half-life of 1.05×10^{11} yrs and natural abundance of 0.090% [4]. Taking into account the chemical composition of $LaBr_3$:Ce 5% and its density of 5.1 g/cm^3, the calculated activity of 1.46 counts/s/cm^3 is in good agreement with our data. Excluding sample 1 because of its larger error, the averaged measured activity is 1.45 counts/s/cm^3, within ±5% error. There are variations in literature on the ^{138}La half-life, and [4],[12]-[15] report values ranging from 1.05×10^{11} yrs and 1.02×10^{11} yrs. Using the spectra in Fig. 1b, we also evaluated the partial half-life of ^{138}La for ε- and β-decay and found good agreement with the values reported in literature, e.g. [4].
The observed approximately constant ^{138}La activity across the different sample volumes confirms that environmental contributions like from ^{40}K are insignificant.

2.3 L/K capture ratio

Information on the ratio between the probabilities of L-shell electron to K-shell electron capture (L/K-ratio) can be obtained using the integral number of count in the L and K cascade peaks in Fig. 1b corrected for the background counts that are mostly from the Compton and β continua. Results are reported in Table 3.

Table 3 – Experimental K and L capture rates.
Error is ±5% for the K and L capture events and ±10% for their ratio, with the exception of sample 1 for which the L capture events error is ±10% and 15% for the ratio. The theoretically determined ratios are 0.402 for L/K and 0.449 for (L+M)/K. The experimentally determined L/K capture ratio averaged on the 4 samples is 0.442.

Sample	K captures counts/s/cm^3	L captures counts/s/cm^3	L/K capture ratio
1	0.516	0.274	0.530
2	0.529	0.246	0.464
3	0.471	0.194	0.412
4	0.313	0.113	0.362

We also evaluated the L/K-ratio based on the theory of electron capture using the tables in [4], [16] and [17]. According to [4], the capture probability λ_x per second for an electron from an atomic shell x due to a 2nd order unique forbidden transition as in ^{138}La, is proportional to:

$$\lambda_x \propto n_x \frac{\left(p_x^{2k_x-2}\ \beta_x^{\,2}\ B_x\right)}{(2k_x-1)!\left(2(3-k_x)+1\right)!}\ q_\nu^{8-2k_x} \qquad (1)$$

where n_x is the relative occupation number of atomic shell x, $k_x = 1$ for K, L1, L2, M1, M2 shells, $k_x = 2$ for L3, M3, M4 shells and $k_x = 3$ for the M5 shell, p_x is the bound electron linear momentum, β_x is the Coulomb amplitude of the bound-state electron radial wave function, B_x is the associated electron exchange and overlap correction, and q_ν the antineutrino energy.
The theoretically determined L/K ratio is 0.402, and the fractions are: L1/K=0.065,

L2/K=0.002 and L3/K=0.335. The M/K ratio is 0.047. K electron capture accounts for 69.0% of the ε decays, L electron capture for 27.7% and M electron capture for the 3.2%.

Within the 10% error, the L/K capture ratio for samples 3 and 4 is in agreement with theory, whereas sample 1 and 2 show about 30% and 15% larger values, respectively. Such deviation can be explained by the x-ray escape probability as follows. A K x-ray fluorescence ($K_{\alpha 1}$, $K_{\alpha 2}$ and $K_{\beta 1}$) has about 50% chance of crossing without absorption or scattering a 100 μm layer of $LaBr_3$ against 0% chance for the L x-ray fluorescence [18]. Then, the K x-ray escaping from the first 0.1-0.2 mm below the sample surface leads to a sizable reduction of the content of the K cascade peak, particularly for the smallest sample. This is confirmed by the observed lower count rate in the K cascade peak of sample 1 compared to that of sample 2, see column 2 of Table 3. In addition, the cascade from refilling of the K shell hole will add a count to the L cascade peak. Both effects will increase the L/K ratio with decreasing sample size.

As pointed out in [19], the L/K ratio can also be determined by comparing the area of the two Gaussian functions fitted through the ^{138}Ba de-excitation peak as shown in Fig. 2. For sample 4, which offers the better statistics for that peak, we evaluated a ratio of 0.477±7%. This value actually relates to the (L+M)/K ratio because the lower energy Gaussian includes the events from the M-shell hole cascade in coincidence with the 1436 keV ^{138}Ba γ-ray. For sample 3 we obtained an extra measurements of the L/K ratio of 0.414±5% based on the collection of the β continuum (see Section 3).

3 The measured β continuum

In the ^{138}La β-decay one β particle, one γ-ray, and one antineutrino are emitted. The β particle energy can have any value from zero to the end point energy of 255.11 keV (rounded to 255 keV) and the γ has energy of 788.7 keV (rounded to 789 keV) [4] [15].

Fig. 1a shows that in $LaBr_3$ the γ is always detected in coincidence with the β, giving rise to a so-called shifted β continuum. When the γ escapes the crystal only the single β particles are detected. Below 255 keV in Fig. 1a, it can be seen how the intensity of the β continuum increases with decreasing of the detector size, i.e. when the γ-ray escapes the crystal more frequently.

3.1 Measuring the β continuum in coincidence with escaping 789 keV gamma-rays

By detecting the 789 keV γ-ray escaping from the $LaBr_3$ scintillator with another detector one may generate an electronic gate on the signal acquisition of the $LaBr_3$ scintillator and then acquire the β continuum in isolation.
We used the 12.9 cm^3 $LaBr_3$ sample 3 for detection of the β continuum in isolation and a $CeBr_3$ scintillator [10] as coincidence detector for the escaping 789 keV γ-ray. Fig. 3 shows that over the entire energy range the intrinsic count rate of $CeBr_3$ is an order of magnitude smaller than that of an equivalent $LaBr_3$ scintillator allowing a clear detection of the 789 keV γ-ray. In addition $CeBr_3$ scintillation decay time matches that of $LaBr_3$ so that signal delays are not needed for generating the coincidence timing window and the window can be as narrow as few μs reducing the number of random coincidences.

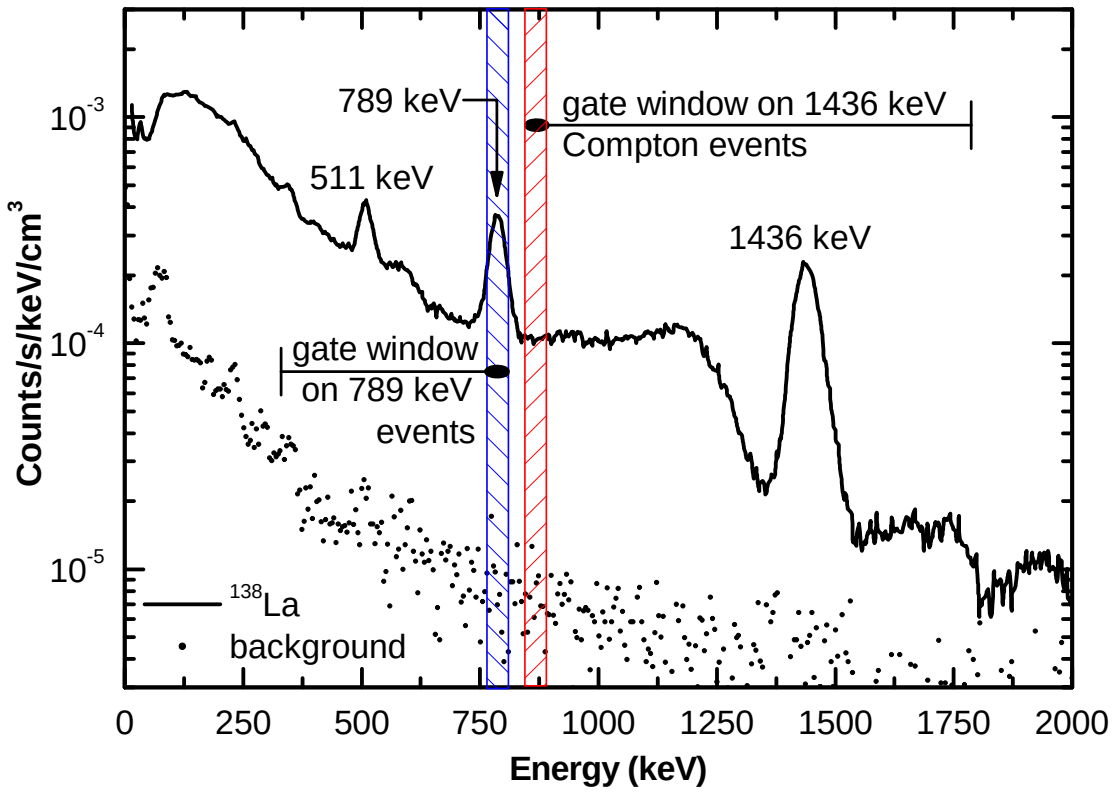

Fig. 3 - Solid spectrum shows the pulse height spectrum from ^{138}La γ-rays from sample 3 detected with the $CeBr_3$ scintillator. Dotted spectrum shows the intrinsic activity spectrum of the $CeBr_3$ detector. The two vertical dashed regions show the two discriminator settings (around and above 789 keV) used to acquire the β continuum in isolation.

With the use of a signal discriminator, every event falling in the energy region from 710 to 810 keV (which include the 789 keV peak) detected with the $CeBr_3$ (see Fig 3) triggers a gate generator controlling the signal acquisition (MCA/PHA) connected with the $LaBr_3$ detector. In this way events from the β-decay with escaping 789 keV γ-ray, in which we are interested, are collected. The obtained spectrum (line (1) in Fig. 4) shows the β continuum but also reveals a contribution from the K and L cascade peaks from the ε decays. These appear in the spectrum whenever the coincidently emitted 1436 γ from the ^{138}Ba de-excitation escapes the $LaBr_3$ and creates a Compton scattered photon in $CeBr_3$ with energy that falls within the signal discriminator window (see Fig. 3). These Compton scattered events are part of a relatively flat region of the Compton continuum in the pulse height spectrum. By repeating the measurement with the gate window positioned at energies just above the 789 keV peak we were able to acquire a spectrum containing exclusively the K and L cascade peaks with full absence of the β continuum, see spectrum (2) in Fig. 4. The acquisition lasted for 227 hrs for both spectra in Fig. 4 with a net number of collected β events of about 20000, i.e. ~1.5 counts/min. We know from the activity measurements the amount of 789 keV γ-rays emitted by samples 3 in 4π-str, and we can evaluate the detection efficiency of our setup to be ~0.6%.

The spectrum acquired with the gate window above 789 keV (spectrum (2) in Fig. 4), shows no other features apart from the K and L cascade peaks and by simple subtraction of it to the other spectrum in Fig. 4, the shape of the true β continuum is obtained as shown in Fig. 5. Here the channels are rebinned to a channel width of 1.3 keV corresponding to 256 channels for an energy range of about 0-330 keV.

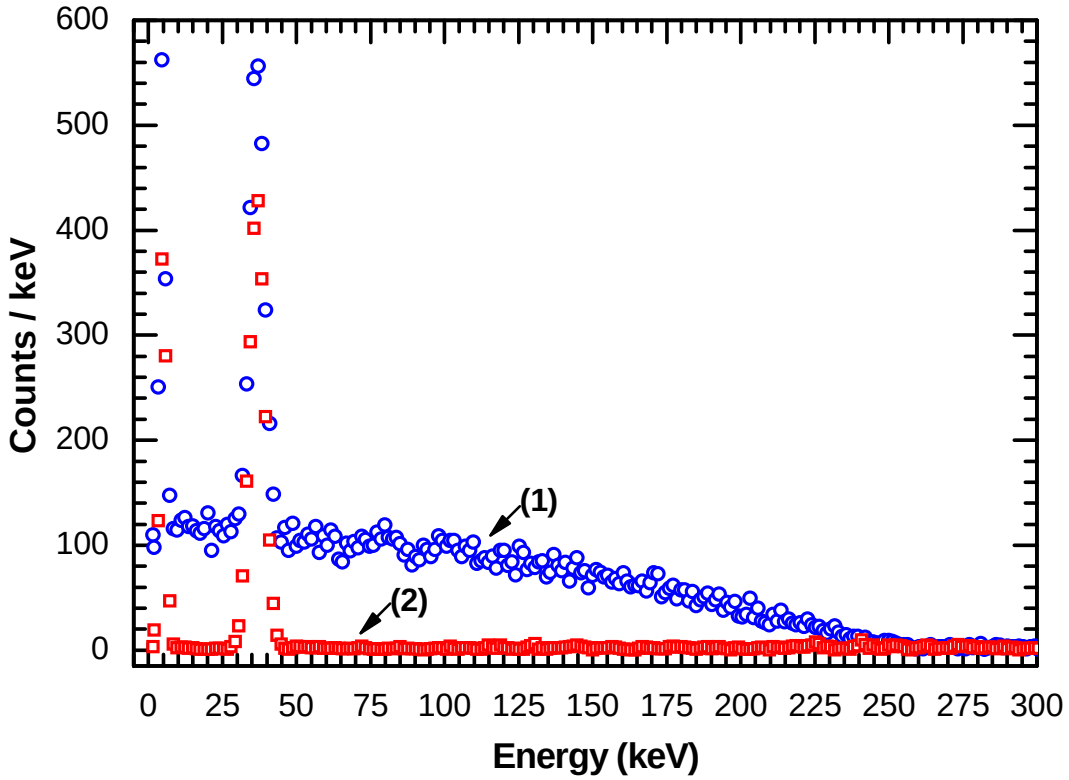

Fig. 4 - β spectrum and K and L cascade peaks spectrum collected gating the $LaBr_3$ acquisition respectively at and above the 789 keV peak as detected by the $CeBr_3$.

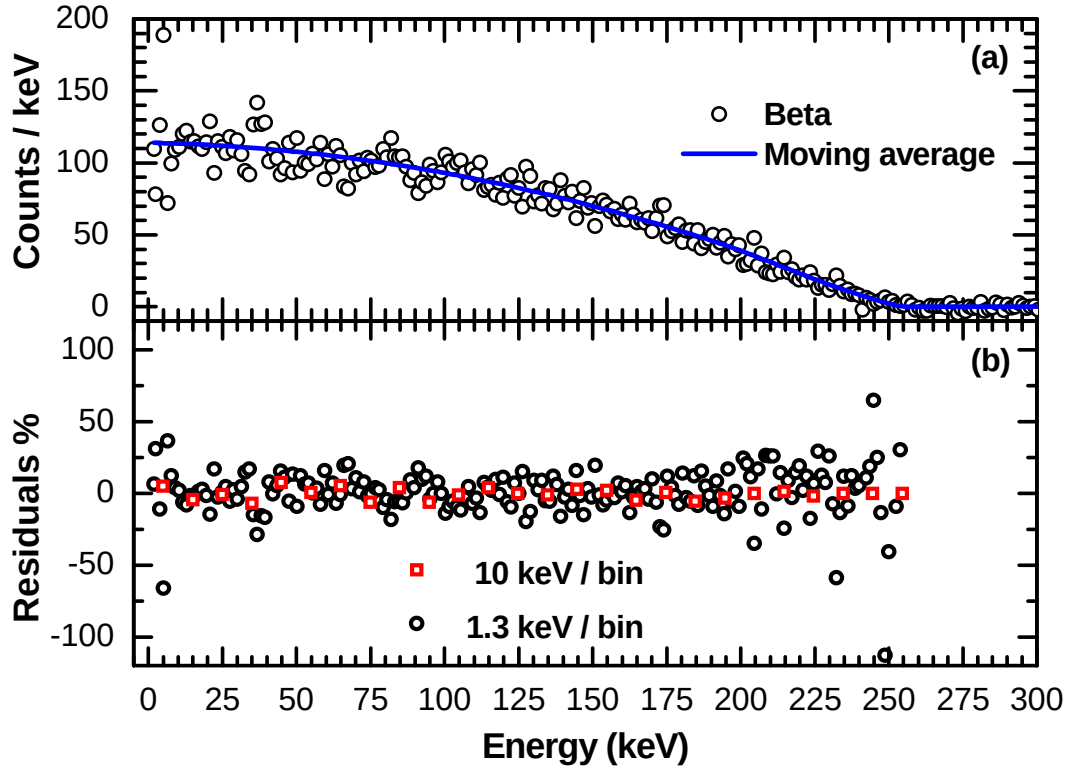

Fig. 5 - The net β continuum after the K and L cascade peaks subtraction and β continuum moving average. The residuals from Eq. (2) are also reported for two different rebinning, 1.3 keV/channel and 10 keV per channel.

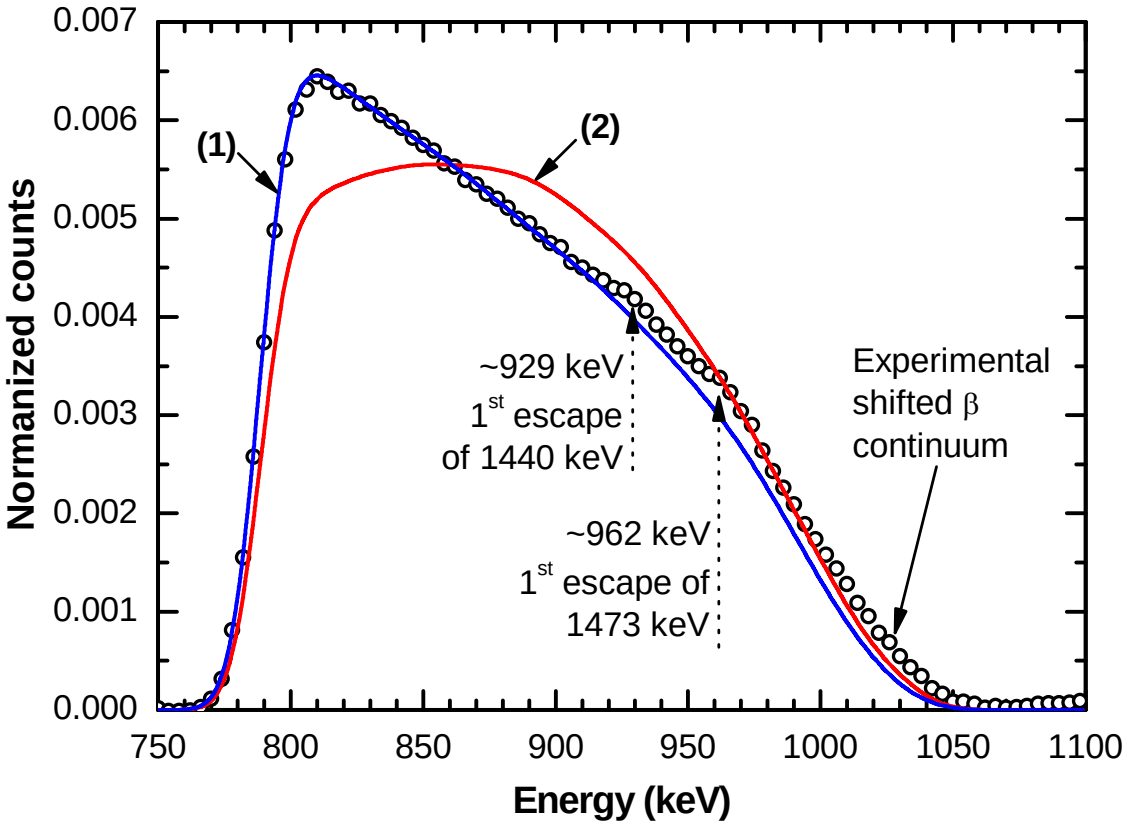

Fig. 6 - The shifted β continuum (dotted data symbols) collected with sample 4 is compared to the measured in coincidence β continuum convoluted with the 789 keV γ-ray (1) and theoretical β continuum also convoluted with the 789 keV γ-ray (2).

The K and L cascade peaks recorded in coincidence with escaping γ-rays show a slight degradation in energy resolution as compared to that recorded of the intrinsic activity in Fig. 1b, i.e. for the K peak in coincidence the resolution is 5 keV FWHM compared to 4.5 keV in Fig. 1b. When taking into account that the activity measurement lasted about 5 hrs compared to 227 hrs for the coincidence experiment we conclude that the long duration of the coincidence experiment is not substantially affected by gain and/or electronic drifts.

The spectra shown in Fig. 4 are the ones used for a further evaluation of the K/L-ratio in sub-Section 2.3.

The range of 255 keV β particles in $LaBr_3$ is about 0.2 mm [20], and in the part of the $LaBr_3$ volume that is close to the surface incomplete energy detection is possible due to β escape. For the chosen $LaBr_3$ sample 3, this volume is of the order of 2% of the total and it will not affect the shape of the measured β continuum.

From the β continuum shown in Fig. 5a, (that will be redisplayed normalized later in Fig. 7) we created a moving average to reduce its statistical dispersion

(see Fig. 5) and evaluated the deviation between true data and the averaged curve. Defining the deviation as:

$$Deviation = 100\,\frac{true\ data - averaged\ data}{averaged\ data} \tag{2}$$

considering the whole energy range, the average deviation of the residuals is 11%. The largest deviation is found towards the end point, in the energy range 210-255 keV, and is 13% (see Fig. 5). After further rebinning of the experimental data to ~10 keV per channel the average deviation reduces to less than 2%, this is also plotted in Fig. 5.

3.2 Deconvolution of the ^{138}La β continuum

The shape of the β continuum can also be obtained using the shifted β continuum that appears in the spectral region from 789 keV and above in Fig 1a. For sample 4, this part of the spectrum is replotted in Fig. 6 (dotted data symbols). The shape of the shifted β continuum is the result of a convolution of the 789 keV γ-ray total absorption peak with the genuine β continuum. The detected shape is slightly disturbed by the presence of the two single 511 keV escape peaks from the detection of 1440 keV and 1473 keV of the ^{138}Ba de-excitation by means pair creation. In Fig. 6, the positions of these escape peaks are indicated.

The measured shifted β continuum was deconvolved numerically and the resulting β continuum is shown as spectrum 3 in Fig. 7. This β continuum and spectrum 2, measured by the coincidence method, are totally independent measures obtained with two different crystals, sample 4 and sample 3, respectively. Both spectra match very well providing good confidence in the accuracy of the experimentally determined shape of the β continuum.

We did also carry out the reverse operation convoluting the β continuum measured in coincidence, with the 789 keV γ-ray and the results are shown in Fig. 6, lines (1). The convolution creates the shape of a shifted β continuum based on the shape of the β continuum measured in coincidence. Again we found a good matching of the two shapes.

4 Theoretical evaluation of the β continuum and comparison with experiment

We have carried out a theoretical evaluation of the shape of the β continuum for ^{138}La decay. The decay process is characterized by a second order unique forbidden transition [21], [22]. In fact, it is a neutron of the nuclear shell 1 $h_{11/2}$ that decays into a proton of the nuclear shell $2d_{5/2}$ generating a transition from level 5^+ to 2^+ with conservation of parity. Therefore the evaluation of the β continuum is more complex than for an allowed transition where the electron and antineutrino escape with total orbital angular momentum equal to zero.
The expression for the probability *P(E)* of a β emitted with energy *E*, according to Behrens and Jäneke [16] is,

$$P(E) = \frac{c\,G^2\left|M_{if}\right|^2 m_e c^2}{2\pi^3(\hbar c)^7}\left(\frac{p_e c}{m_e c^2}\right)\cdot(E + m_e c^2)\left(255 - E\right)^2\, F_R(Z+1,E)\, S\, a_2 \qquad (3)$$

where F_R the relativistic Fermi function, *S* the correction for electron screening and a_2 is the shape factor; *c* the light velocity, *G* the Fermi constant, M_{if} the transition matrix element and *E* the electron kinetic energy, p_e its momentum and m_e its mass. The a_2 factor includes the correction due to the penetration of the centrifugal barrier for charged particles with non-zero angular momentum [23,24]. The values of F_R are taken from the tables by Behrens and Jänecke [16]. In these tables, F_R refers to a nucleus of atomic number *A* of 140 instead of 138, as in our case. A correction for the actual atomic number is also provided by [16]. However, its evaluation did lead to a negligible correction for F_R of the order of only +0.21% at low energies and +0.22% toward the end point and we did not apply it. The obtained F_R values are compiled in column 3 of Table 4. The table by Behrens and Jänecke [16] also provides the screening correction *S* whereas for shape factors a_2 we used the analytical formulation proposed by [23]. Together, F_R, *S* and a_2 provided the theoretical probability *P(E)*, or equivalently the shape of the β continuum, as compiled in column 6 of Table 4 and displayed as spectrum (1) in Fig. 7.

Table 4 – Theoretical evaluation of the β distribution.

$\frac{v}{c}$ $\left(\frac{p_e c}{m_0 c^2}\right)$	Energy [keV]	$F_R(58,E)$	S	a_2	$P(E)_{Th}$ $\times 10^{-3}$ [$keV^{-1}s^{-1}$]
0.05	0.64	166.115*	0.9703*	0.220	4.80
0.09	1.90	97.835*	0.9705*	0.223	4.90
0.10	2.55	84.959	0.9705	0.224	4.94
0.20	10.12	42.902	0.9710	0.239	5.09
0.30	22.50	29.058	0.9716	0.265	5.29
0.40	39.36	22.263	0.9722	0.303	5.48
0.50	60.32	18.288	0.9727	0.356	5.60
0.60	84.92	15.723	0.9733	0.430	5.56
0.65	98.46	14.759	0.9737	0.479	5.46
0.70	112.75	13.956	0.9741	0.537	5.27
0.80	143.40	12.680	0.9750	0.694	4.57
0.90	176.48	11.723	0.9761	0.924	3.30
1.00	211.66	10.984	0.9771	1.261	1.51
1.05	229.95	10.667*	0.9777*	1.481	0.62
1.117	255.11	10.296*	0.9784*	1.844	0.00

* These values of F and S are evaluated interpolating the data in [16].

From the comparison of the theoretical and the two experimental β continua in Fig. 7 and Table 5, a significant deviation is observed. Experimentally, the probability of emission at energies below, say 75 keV, is significantly to much higher than predicted with standard theory.
We did also carry out a convolution of the theoretical β continuum, as done before for the measured in coincidence β continuum, to compare it with the shifted β continuum (Fig. 6, lines (2)). Also in this case we found a mismatch with the shifted β continuum and the theoretical evaluated shifted continuum.
A recent publication, McIntyre et al. [25] reports the ^{138}La β continuum, measured in a $LaCl_3$ scintillator by coincidence technique. This β continuum, which is collected down to 15 keV, shows the same behaviour as we found, with an excess of events at energies below 75 keV compared to the theoretical evaluation.

Table 5 – Theoretical and experimental β distributions.
Coincidence P_{Ex} and deconvolution P_{Ex} are both corrected for electron nPR (see text). Values correspond to Fig. 6 curves. P_{Th} is reported from Table 4 for easier comparison. 1.9 keV for the coincidence P_{Ex} is the lower point detected.

Energy (keV)	P_{Th} $\times 10^{-3}$ $keV^{-1}s^{-1}$	Coincidence P_{Ex} $\times 10^{-3}$ $keV^{-1}s^{-1}$	Deconvolution P_{Ex} $\times 10^{-3}$ $keV^{-1}s^{-1}$
0.64	4.80	--	6.67
1.90	4.90	6.49	6.59
2.55	4.94	6.48	6.57
10.12	5.09	6.44	6.61
22.50	5.29	6.35	6.51
39.36	5.48	6.15	6.19
60.32	5.60	5.85	5.75
84.92	5.56	5.45	5.15
98.46	5.46	5.20	4.87
112.75	5.27	4.90	4.59
143.40	4.57	4.06	3.91
176.48	3.30	2.75	2.96
211.66	1.51	1.23	1.27
229.95	0.62	0.44	0.54
255.11	0.00	0.03	0.00

An evaluation of the transformation matrix M_{ij} based on the ^{138}La half life was used to determine the coefficient D defined as $P(E) = D \cdot (255 - E)^2$ with respect to Eq. (3). This allowed generating a Kurie-Fermi plot (see Fig. 8) for the experimental data points corresponding to that energies for which D is known. The disagreement between experiment and theory in Fig. 7 below 75 keV is also evident for the Fermi-Kurie plot in Fig. 8 below 75 keV where the experimental data deviate upwards from theory. Similar deviations were observed in earlier experiments, e.g. by Wu [26]. Towards the end point energy of 255 keV agreement between theory and experiment is good.

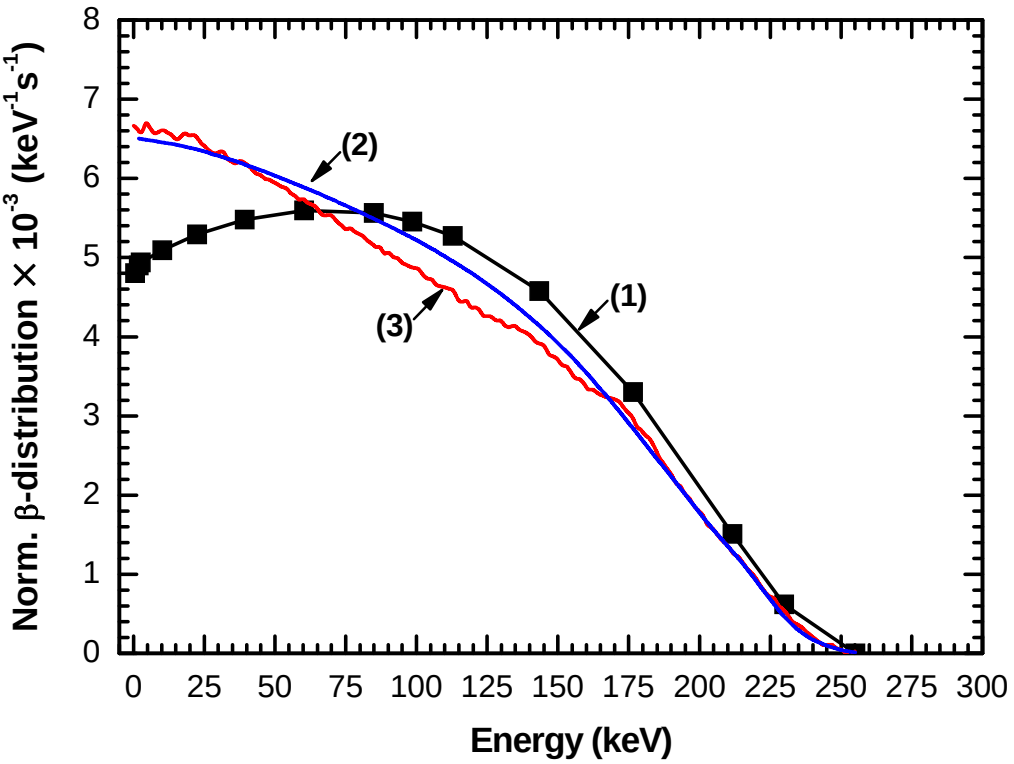

Fig. 7 - Comparison of β continuum spectra of ^{138}La. (1) theoretical evaluated, (2) experimentally evaluated using coincidence method, (3) experimentally evaluated using deconvolution method.

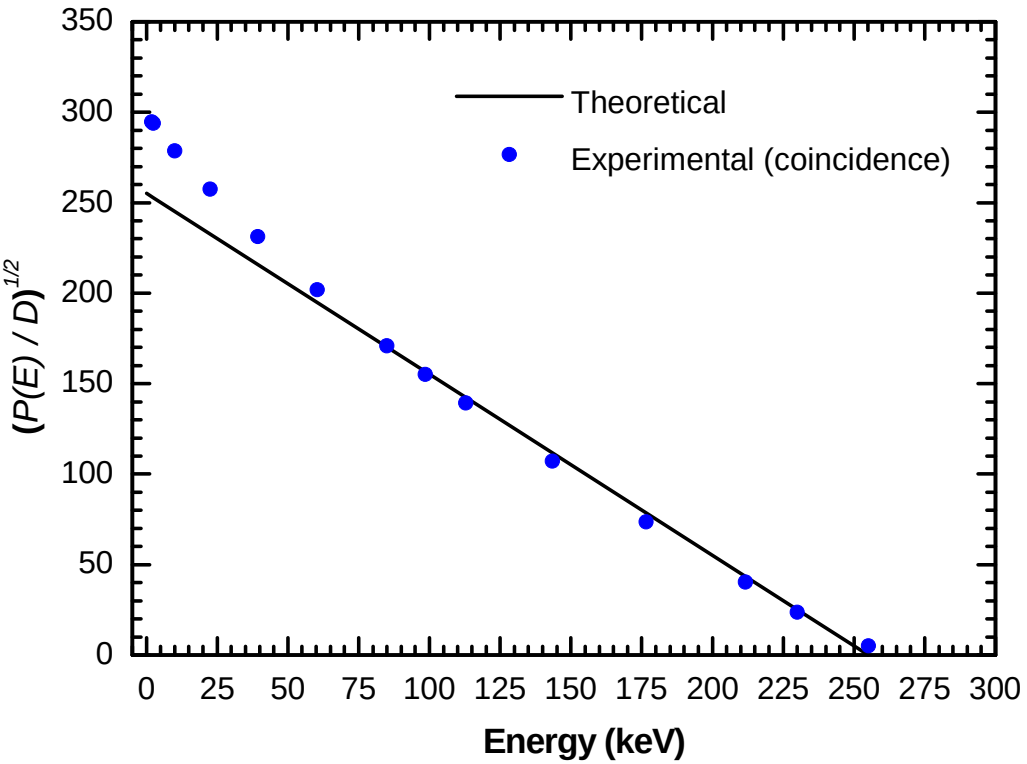

Fig. 8 - Kurie-Fermi plot of ^{138}La β decay. Solid line is obtained from the theoretical probability *P(E)* and data symbols are obtained from experiment in this work. The coefficient *D*, appearing in ordinates, is defined in the text.

Works by Wilkinson [27] report that the shape of the β continuum will alter due to radiative energy loss by electrons emitted in unique second order forbidden transitions. The proposed correction is almost constant across the β energy range of ^{138}La and it cannot explain the observed disagreement.
If instead of using the analytical formulation for the shape factor a_2 proposed by [24] one uses the shape factors a_2 from the Landolt-Bornstein tables in [16] the effect on the theoretical β continuum shape is marginal, showing overlapping of the two respective shapes within ~1.5%.
Apparently there is not a trivial explanation for the observed difference between the theoretically and experimentally found shapes for the β continua. It may be that the theory on either the shape factor a_2 or the screening factor S is not entirely correct at low β energies. Already Blatt and Weisskopf [23] mentioned a possible underestimation of the screening effect S at low β energies. From Table 4 a correction factor can be derived in order to match the theoretical spectrum with the experimental data. Whether the corrections should then be used to revise the shape factor a_2 or the screening factor S is outside the scope of this work.
On the experimental side, other scintillator materials can provide opportunity for similar experiments as in this work. For instance, the elpasolite scintillator family as in [28,29] that contains ^{40}K, or $Bi_4Ge_3O_{12}$ (BGO) scintillators grown with some concentration of ^{207}Bi.

5 Summary of results

From a study on the intrinsic activity from ^{138}La decay in four different sized $LaBr_3$ scintillators we established an activity of 1.45 counts/s/cm^3 that agrees with expectations from the natural abundance of ^{138}La isotope. Making use of nPR data we also precisely evaluate the equivalent energy of the intrinsic activity peaks. These are 4.5 keV 35.5 keV and 1470 keV. The peak at 1470 keV is a combination of three sub-peaks with main component being the 1436 keV γ-ray from ε-decays plus the cascade products from the refilling of a hole in the K-shell in the Ba-atom. This event deposits 37.4 keV but only 35.5 keV are detected because of the nPR for a total ~1472 keV equivalent energy. Because of the other two components the maximum of the three components peak occurs at the lower energy of 1470 keV, as already reported in [7]. We propose to use this value in calibrating pulse height spectra when based on the intrinsic photopeak.

Moreover, the intrinsic activity study of this work provides a L/K capture ratio of about 0.44±10% for the ε decay of ^{138}La that agrees well with theory.
Several methods were used to determine the shape of the β continuum emitted in the β-decay of ^{138}La. Since the β particles are generated inside the scintillator, and because $LaBr_3$ has excellent energy resolution, an accurate spectral shape down to less than 2 keV has been obtained. By comparing that shape with the one predicted from standard nuclear theory a significant deviation was found for β energies of 75 keV and lower. An explanation for that observation is beyond the scope of this work and should most likely be sought within the theory of second order forbidden β-decay and, more in particular, within the evaluation of the screening factor.

References

[1] B. D. Milbrath et al., "Contamination Studies of $LaCl_3$:Ce Scintillators", IEEE Trans. Nucl. Sci. 53 (2006) 3031.

[2] B. D. Milbrath et al., "Characterization of alpha contamination in lanthanum trichloride scintillators using coincidence measurements", Nucl. Instr. and Meth. A 547 (2005) 504.

[3] F. Quarati et al., "X-ray and gamma-ray response of a 2″×2″ $LaBr_3$:Ce scintillation detector", Nucl. Instr. and Meth. A 574 (2007) 115.

[4] R. B. Firestone, "Table of Isotopes", 8th edition Wiley-VCH, 1999.

Available http://ie.lbl.gov/toi.html

[5] R. Bernabei et al., "Performances and potentialities of a $LaCl_3$:Ce scintillator", Nucl. Instr. and Meth. A 555 (2005) 270.

[6] W. J. Kernan, "Self-Activity in Lanthanum Halides", IEEE Trans. Nucl. Sci. 53 (2006) 395.

[7] R. Nicolini et al., "Investigation of the properties of a 1″×1″ $LaBr_3$:Ce scintillator", Nucl. Instr. and Meth. A 582 (2007) 554.

[8] I.V. Khodyuk and P. Dorenbos, "Nonproportional response of $LaBr_3$:Ce and $LaCl_3$:Ce scintillators to synchrotron x-ray irradiation", J. Phys.: Condens. Matter 22 (2010) 485402.

[9] Saint-Gobain Crystals http://www.detectors.saint-gobain.com

[10] R. Billnert et al., "New information on the characteristics of 1 in. × 1 in. ceriumbromide scintillation detectors", Nucl. Instr. and Meth. A 647 (2011) 94.

[11] Lawrence Berkeley National Laboratory X-ray data booklet (3rd ed.) September 2009. Available: http://xdb.lbl.gov/

[12] T. Tanaka and A. Masuda, "The La–Ce geochronometer A new dating method", Nature 300 (1982) 515.

[13] E. B. Norman and M. A. Nelson "Half-life and decay scheme of ^{138}La", Phys. Rer. C 27 (1983) 1321.

[14] Nuclear Wallet Cards and Evaluated Nuclear Structure Data File (ENSDF). Available: http://www.nndc.bnl.gov

[15] A. A. Sonzogni, "Nuclear Data Sheets for A = 138", Nucl. Data Sheets 98 (2003) 515.

[16] The Landolt-Bornstein Database, H. Behrens and J. Jänecke, "Numerical Tables for Beta-Decay and Electron Capture", Springer-Verlag, 1969.

[17] W. Bambynek et al., "Orbital electron capture by the nucleus" Rev. Mod. Phys. 49 (1977) 77-221; W. Bambynek et al., "Erratum: Orbital electron capture by the nucleus", Rev. Mod. Phys. 49 (1977) 961.

[18] National Institute of Standards and Technology (NIST), XCOM: Photon Cross Sections Database.

Available: http://www.nist.gov/pml/data/xcom/index.cfm

[19] F. Camera et al., "Investigation of the self activity and high energy γ-rays response of a 1″×1″ and 3″×3″ $LaBr_3$:Ce scintillators", IEEE Nucl. Sci. Symp. Conf. Rec. 2007, N24-186.

[20] National Institute of Standards and Technology (NIST), ESTAR: Stopping Powers and Ranges for Electrons.

Available: http://physics.nist.gov/PhysRefData/Star/Text/ESTAR.html

[21] A.M. Mandal and A. P. Prato, "(L+M+…)/K capture ratio in the decay of ^{207}Bi", J. Physc. G: Nucl. Phys 11 (1985) 1025.

[22] J. L DuBard et al., "Three-Quasiparticle States in ^{139}La", Phys. Rev. C 3 (1971) 1391.

[23] J. M. Blatt and V. F. Weisskopf, "Theoretical Nuclear Physics", J. Wiley & Sons, New York, 1960.

[24] C.S. Wu and S.A. Moszkowski, "Beta Decay" J. Wiley & Sons, New York, 1966.

[25] J.I. McIntyre et al., "$LaCl_3$:Ce coincidence signatures to calibrate gamma-ray detectors", Nucl. Instr. and Meth. A 652 (2011) 201.

[26] C. S. Wu, "Recent Investigation of the Shapes of β-Ray Spectra", Rev. Mod. Phys. 22 (1950) 386.

[27] D.H. Wilkinson, "Evaluation of beta-decay, Part VII: The Z-independent outer radiative correction for unique-forbidden decay", Nucl. Instr. and Meth. A 406 (1998) 89.

[28] R. Hawrami et al., "New scintillator materials K_2CeBr_5 and Cs_2CeBr_5", J. Crystal Growth 310 (2008) 2099.

[29] J.C. van't Spijker et al., "Scintillation and luminescence properties of Ce^{3+} doped K_2LaCl_5", J. Lumin. 85 (1999) 1.

Chapter 7

Recent developments

This chapter closes the thesis describing current efforts and successes in the development of new scintillator detectors that can compete with $LaBr_3$ in terms of energy resolution and detection efficiency but with increased gamma-ray detection sensitivity because of a reduced intrinsic activity. Experiments and results have shown that $LaBr_3$ is, among gamma-ray spectrometers, an optimum choice for applications in space, however further developments are still possible as described below.

At the energy of the gamma-ray emitted by ^{40}K (1.4 MeV), $LaBr_3$ presents a low sensitivity caused by the overlapping of the gamma-ray energies of ^{138}La and ^{40}K. In space applications, amongst other applications, efficient detection of ^{40}K is of interest and a corresponding improvement in detector sensitivity is sought. Granted by ESA, a consortium composed by TU Delft, Praeseape BV, Schott AG, Hellma Material GmbH and Scionix BV was set up in 2011 to develop possible alternatives to $LaBr_3$. After significant effort spent developing the growth technique, $CeBr_3$ crystal are now available with dimensions larger than 2″×2″ and can effectively compete with $LaBr_3$ in terms of sensitivity for gamma-ray detection.

Current $CeBr_3$ spectrometers offer an energy resolution at 662 keV of 4% FWHM, slightly inferior than that of $LaBr_3$. Nevertheless, thanks to their low intrinsic activity of 0.04 – 0.07 Bq/cm^3, (i.e. over 20 times reduced compared to $LaBr_3$) an increasing in sensitivity of 8 times is achieved for the detection of ^{40}K.
In this chapter, the results obtained with a state of art 2″×2″ $CeBr_3$ are presented through a comparison with an equivalent size $LaBr_3$ detector. Nowadays, the scintillator research is working towards deeper understanding of scintillation processes, e.g. of the non-proportionality of the response, with the final goal to further optimizing scintillator performance.

The content of this chapter is based on ongoing research.

Recent developments and ongoing research

For the spectroscopic detection of high energy gamma-rays, large volume detectors are needed to reach sufficiently high detection efficiency. At present, the possible choice is reduced to two options: HPGe or scintillator. Before the discovery of $LaBr_3$ the choice of scintillator implies a substantial compromise since these detectors did not offer sufficiently good energy resolution for most scientific applications. In this thesis, it has been demonstrated that $LaBr_3$ could, and will, be used as the gamma-ray spectrometer onboard BepiColombo thanks to its superior energy resolution, to its radiation tolerance and because the operation of scintillator detector is possible with a fraction of the resources needed to operate an HPGe.

Still, improvements of $LaBr_3$ are possible. In fact, the major drawback of $LaBr_3$ is the presence of ^{138}La as seen in detail in the previous Chapter 6. An important parameter in planetary studies is the ratio of the occurring natural isotope ^{40}K and ^{232}Th [1]. $LaBr_3$ because of the presence of ^{138}La presents a lack of sensitivity for the detection of ^{40}K. Moreover, the whole energy range below 1.5 MeV is strongly affected by intrinsic activity. If for BepiColombo the ^{138}La intrinsic activity does not substantially affect the performance, other space missions, as well as other applications in radiation monitoring, could strongly benefit from a scintillator with energy resolution and detection efficiency matching that of $LaBr_3$ but characterised by a much lower intrinsic activity. For this reason a new project for the development of low-noise scintillators has been initiated by ESA and granted to a consortium comprising TU Delft, Praeseape BV, Schott AG, Hellma Material GmbH and Scionix BV.

The project first task was to select two materials with the capability to supersede $LaBr_3$ in sensitivity. To quantify possible improvement, the simplified formula for sensitivity evaluation of a spectrometer introduced in Chapter 2 (Eq. (1)) can be used The formula, based on [2,3], fixes the spectrometer sensitivity as function of detection efficiency, energy resolution and background, as:

$$Sensitivity \propto \frac{Efficiency}{\sqrt{Energy\ Resolution \times Background}} \quad . \tag{1}$$

Assuming that the activity is evenly spread over the energy range of interest and that the sensitivity is related to the sensitivity at a specific gamma line, Eq. (1) can be further simplified using more practical parameters as effective atomic number Z_{eff}, light yield (LY) and intrinsic activity, becoming:

$$Sensitivity \propto \frac{Z_{eff}}{\sqrt{LY^{-0.5} \times Intrinsic\ Activity}} \quad (2)$$

The -0.5 exponent used for the LY reflects its influence on the statistical energy resolution, see Chapter 4.

We can now compare the effect on the sensitivity of varying one of the parameter, Z_{eff}, LY or intrinsic activity, while keeping the other two constant. Taking $LaBr_3$ as reference, the parameter values are Z_{eff} = 45.3, LY = 60 ph/MeV and Intrinsic Activity = 1.46 Bq/cm^3 and the result is shown in Fig. 1. The suppression of the intrinsic activity (red dots in Fig. 1) has indeed the greatest benefit on the sensitivity. The same benefit cannot be achieved even when the LY is made twice that of $LaBr_3$. More quantitatively, reducing the intrinsic activity by a factor of 10 makes an increase in sensitivity of about 3 times.

In other words, aiming to increase in sensitivity, the first parameter to optimize should be the intrinsic activity.

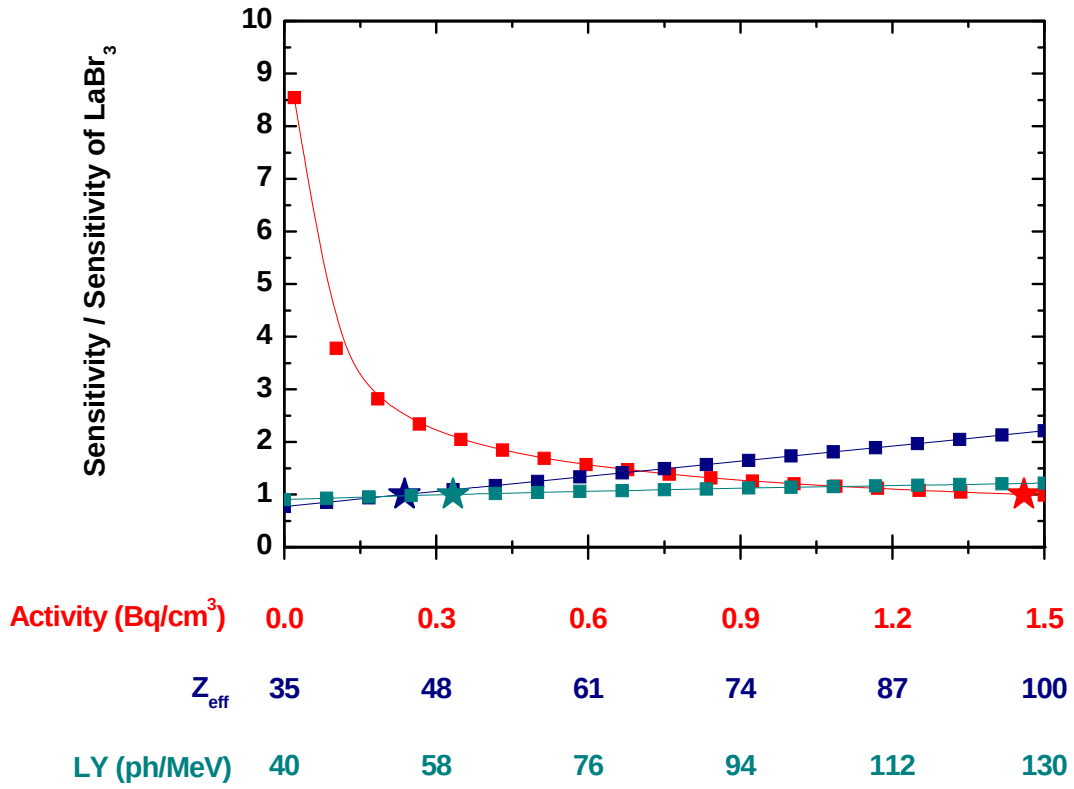

Fig. 1 – The effect in the sensitivity of varying one of the parameters Z_{eff}, LY or intrinsic activity and keeping the other two fixed at the corresponding value for $LaBr_3$. Star data points indicate the typical parameter values for $LaBr_3$.

For this reason, the project focused on radionuclide-free compounds. Two materials were selected for study and development: $CeBr_3$ and SrI_2:Eu. Both offer the additional benefit to have been grown and studied in small samples so that large volume spectrometers could be expected within the project time-frame of two years. After initial trials, and in spite of its low intrinsic activity, SrI_2:Eu was dismissed for the time being because preserving its energy resolution at the minimum size needed in space application ≥ 2″ is rather difficult, as experienced by Sturm et al. [4].

$CeBr_3$ crystals have been grown by Schott AG and more recently by Hellma Materials GmbH and detectors fabricated by Scionix BV. As $LaBr_3$, the material is highly hydroscopic and precaution must been taken to avoid deterioration. The first test was the measurement of the intrinsic activity. In Fig. 2 intrinsic activity spectra of $LaBr_3$ and $CeBr_3$ are compared, clearly showing a great improvement.

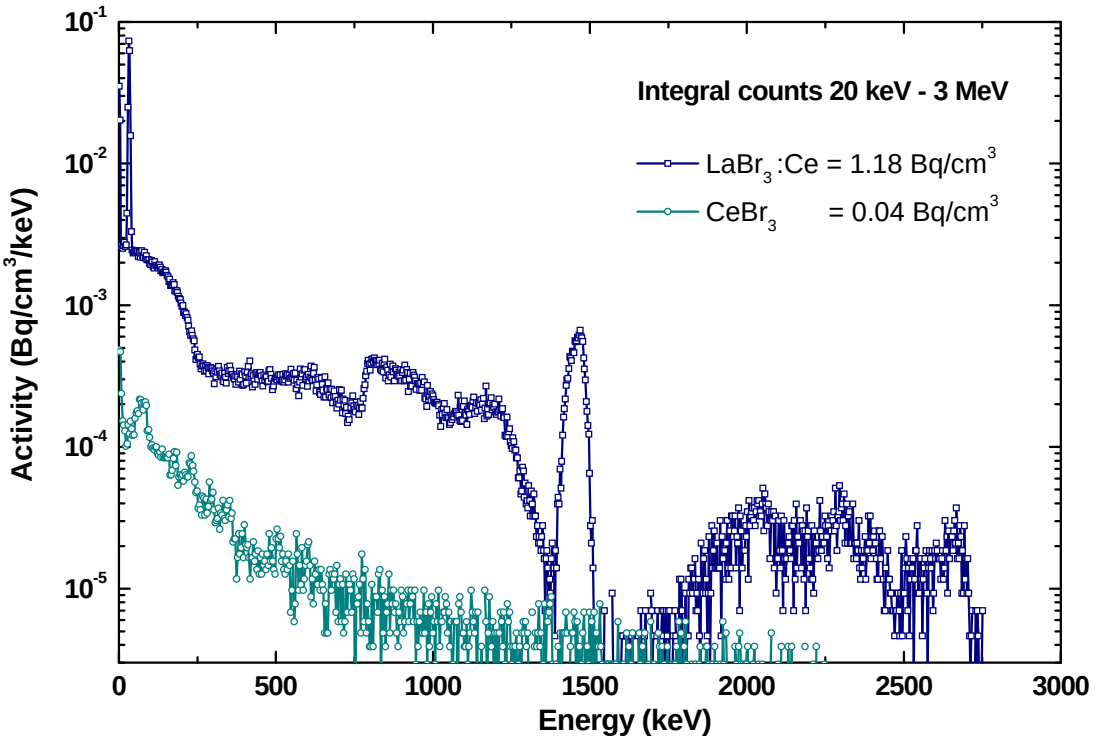

Fig. 2 – Intrinsic activity measured with $LaBr_3$ and $CeBr_3$ using the same experimental conditions, which include a lead castle and a PMT (2″ Electrontubes 9266B) with low ^{40}K content. Integral activity in the energy range from 23 keV up to 3 MeV is 1.18 Bq/cm³ for $LaBr_3$ and 0.04 Bq/cm³ for $CeBr_3$.

In the energy range from 23 keV up to 3 MeV, $CeBr_3$ presents an intrinsic activity over 20 times less compared to $LaBr_3$. For $CeBr_3$ the absence of spectroscopic peaks in the spectrum indicates that the measured intrinsic activity is mainly due to residual environmental activity (not shielded by or present in the lead castle), cosmic rays and possible (undefined) radioactive impurities present in the raw materials and then in the crystals.

Early in 2011, the project target dimension of a 2″×2″ $CeBr_3$ was reached. ^{137}Cs pulse height spectra of such a large detector are shown in Fig. 3. The observed energy resolution is 4.1 % FWHM, in good agreement with the energy resolution observed with smaller sample, i.e. 4.0 %, indicating that, similarly to $LaBr_3$, the scaling up of the size does not imply substantial LY loss.

More spectra have been collected with laboratory gamma-ray sources up to 3 MeV and the corresponding curve energy resolution vs. energy plotted in Fig. 4 together with that of $LaBr_3$. It is found that $CeBr_3$ as well shows a statistics dominated energy resolution. The fitting function in Fig. 4 is in fact $R = 124\sqrt{E}$, with E the energy expressed in keV. Using this correlation, the background spectra shown in Fig. 2 and Eq. (1), the sensitivity can be evaluated as a function of energy. For the photopeak efficiency the data of Ciemala et al. [5] have been used for both materials. This introduces a small error lying within the relative difference of Z_{eff} for the two compounds, 45.3 and 45.9 for $LaBr_3$ and $CeBr_3$ respectively. Results are shown in Fig. 5.

In $CeBr_3$, intrinsic activity due to alpha particles has been observed in some samples grown with raw material from a defined stock and with characteristics similar to the alpha contamination observed in $LaBr_3$ and ascribed to ^{227}Ac and daughters as reported in the previous Chapter 6. The integral count rate in the energy range 23 keV 3 MeV is 0.04 Bq/cm^3. With presence of alpha contamination the intrinsic activity can rise to a maximum of 0.07 Bq/cm^3.

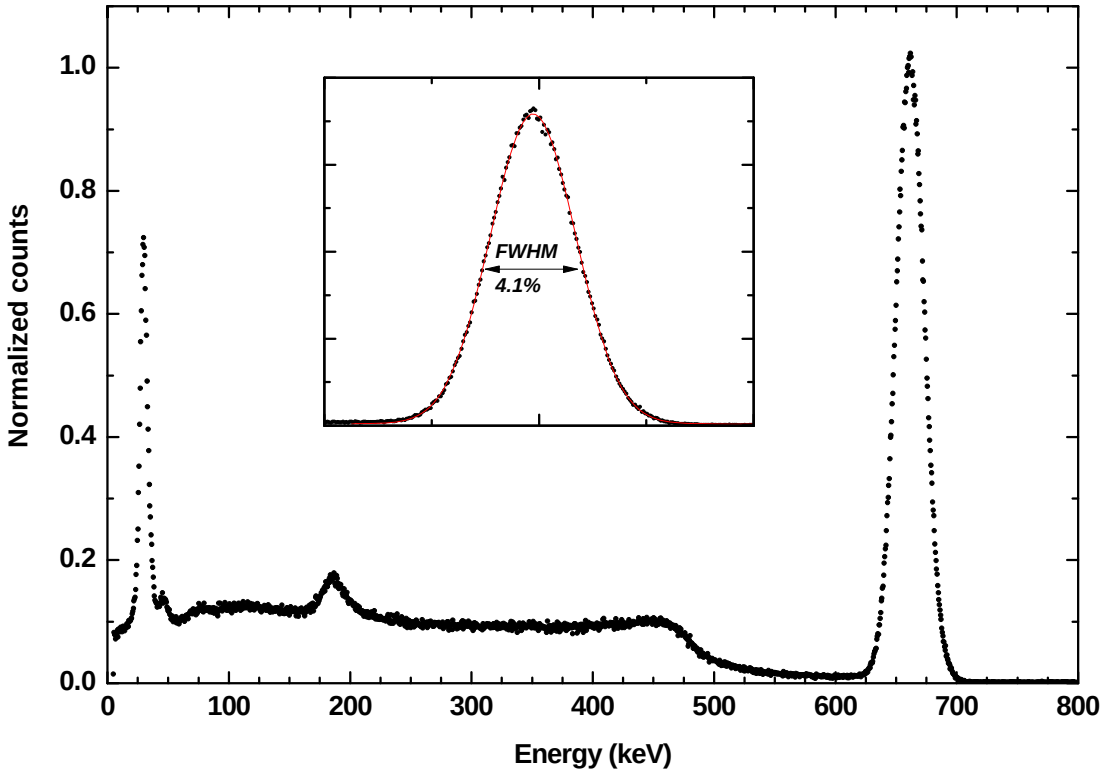

Fig. 3 – ^{137}Cs pulse height spectrum of a 2″×2″ $CeBr_3$ sample.

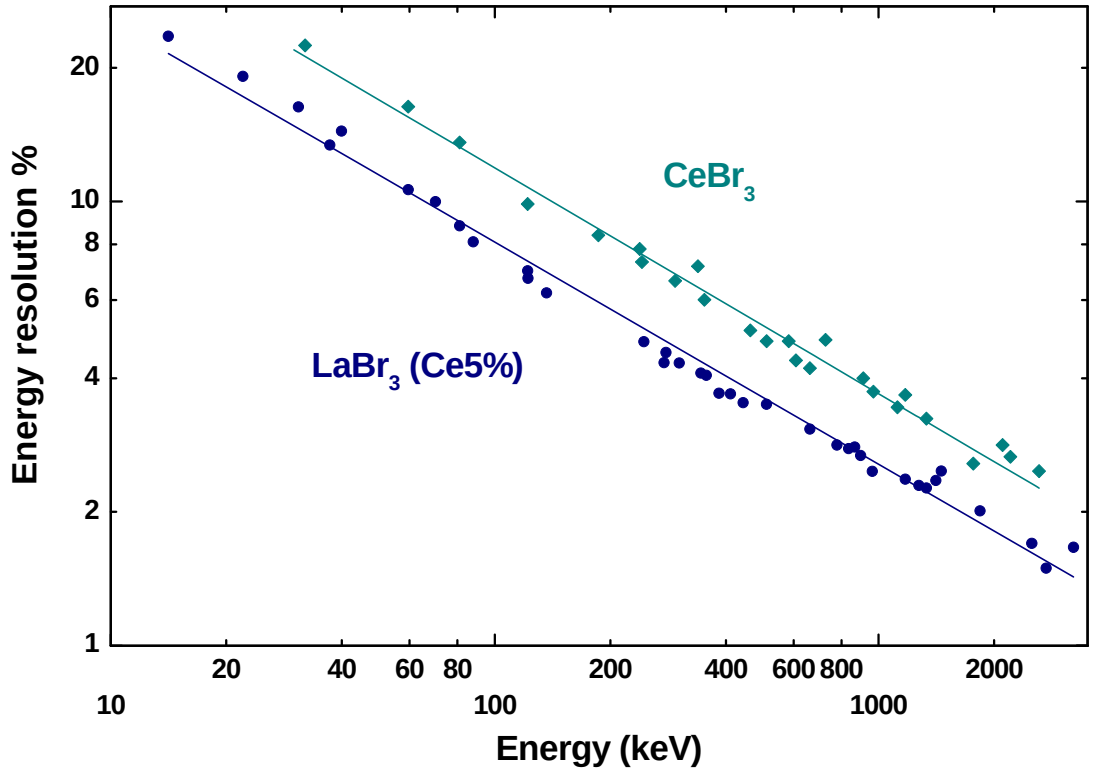

Fig. 4 – Experimental energy resolution FWHM in % for $LaBr_3$ and $CeBr_3$. For $LaBr_3$ the data are the same as in Fig. 6 in Chapter 4. Both samples show an $E^{-1/2}$ dependence.

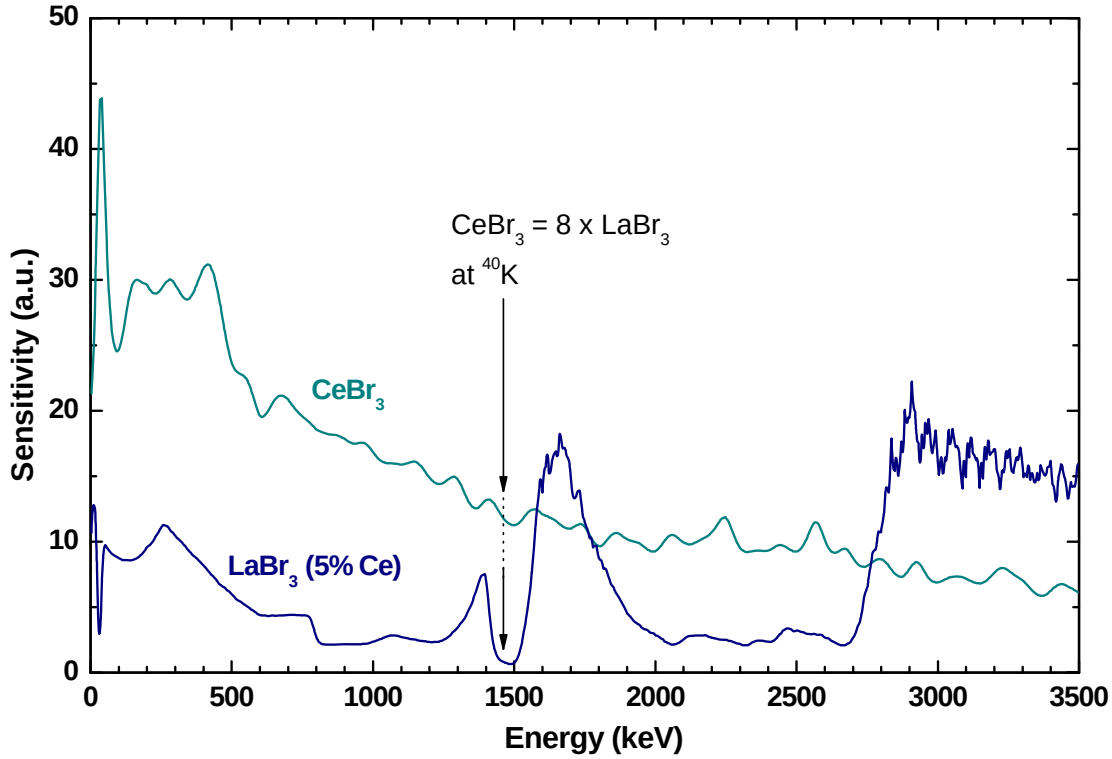

Fig. 5 – Sensitivity curves for 2″×2″ $LaBr_3$ and $CeBr_3$. A clear benefit in sensitivity is found for $CeBr_3$ at energies below 1.5 MeV.

Up till now, $CeBr_3$ has been developed as an alternative compound to $LaBr_3$. Applications requiring high sensitivity for gamma-ray detection will benefit from this new scintillator. Radiation tolerance assessment, as described in Chapter 2, is being organized to test the suitability of $CeBr_3$ for space applications. Results of $CeBr_3$ proton irradiation have already been published by Kim et al. [6] reporting a moderate damaging after the extremely high dose of 60 Mrad.

Research on the scintillation non proportionality of response (nPR) [7,8] is ongoing. $CeBr_3$ has been tested at beamline X1 of HasyLab, Hamburg, synchrotron facility, the same described in Chapter 3, and, compared to $LaBr_3$, its nPR is found more severe. The nPR does contribute significantly to broadening the energy resolution, however, a model which relates quantitatively a specific nPR to the energy resolution does not exist yet.

References

[1] Radioactive Elements on Mercury's Surface from MESSENGER: Implications for the Planet's Formation and Evolution, Science 333, 1850 (2011).

DOI: 10.1126/science.1211576 (and relevant supporting online material (SOM))

[2] J.A. Cooper, "Factors Determining the Ultimate Sensitivity of Ge(Li) Gamma-Ray Spectrometers", Nucl Instr and Meth 82 (1970) 273.

[3] E.L. Chupp, "Gamma Ray Astronomy (Nuclear Transition Region)", D. Reidel Publishing Company, Dordrecht, Holland (1976).

[4] B.W. Sturm et al. "Effects of packaging SrI2(Eu) scintillator crystals", Nucl. Instr. and Meth. A 652 (2011) 242.

http://dx.doi.org/ 10.1016/j.nima.2010.10.041

[5] M. Ciemala, et al., Nucl. Instr. and Meth. A608 (2009) 76.

[6] S. Kim et al. J. Korean Phys. Soc. 52 (2008) 814.

[7] P. Dorenbos et al., Non-proportionality in the scintillation response and the energy resolution obtainable with scintillation crystals, IEEE Trans. Nucl. Sci. 42 (1995) 2190.

[8] I.V Khodyuk and P. Dorenbos, Nonproportional response of $LaBr_3$:Ce and $LaCl_3$:Ce scintillators to synchrotron x-ray irradiation J. Phys.: Condens. Matter 22 (2010) 485402.

Summary

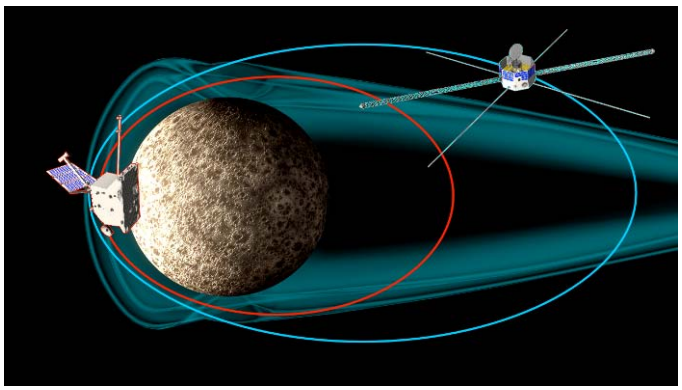

Image: BepiColombo/ESA & JAXA

$LaBr_3$ has been developed into large volume scintillator detectors within an ESA and TU Delft programme during this thesis work. The programme, which aimed at the space applications of $LaBr_3$, also led to extensive experiments within a collaborative framework which included representatives for all the development aspects, i.e., from crystal growers to scintillator materials researchers to final users. The research presented in this thesis is the result from my in-depth involvement in that programme.

The thesis's first achievement was the assessment of the radiation tolerance of $LaBr_3$ in Chapter 2. In fact, BepiColombo's payload must withstand proton fluence as high as 6×10^{10} protons/cm^2 to guarantee successful scientific observations. It was found that $LaBr_3$ exceeds that requirement without substantial deterioration of its performance. Such an ability, together with the relative low mass and power resources demand that is typical for scintillation detectors, has made $LaBr_3$ the choice for the BepiColombo onboard gamma-ray spectrometer.

$LaBr_3$ detectors is a new technology, and experimental studies were necessary to support instrument design and optimization for space applications. The deterioration of performance with increased detector size has been closely monitored in Chapter 4. The limits of $LaBr_3$ application were also studied and, with the use of synchrotron radiation, it was found that $LaBr_3$ is a non-ideal scintillator for photon detection in the X-ray domain, below 100 keV. The same technique proved to be an effective tool for non-proportionality studies and extensively applied by TU Delft colleagues.

Scintillation readout of $LaBr_3$ pushes the PMT to its operational limits. Experimental campaigns were performed to study the response to high energy gamma-rays as reported in Chapter 5. This gave a unique opportunity to observe the correlation between gamma-ray energy and energy resolution up to 15 MeV. In addition, it offered the benchmark to verify in flight energy calibration capability. As demonstrated in Chapter 5 of this thesis, results are satisfactory, which makes $LaBr_3$ applicable for the BepiColombo mission. However the results also suggest to initiate new programmes to develop alternative scintillation readout techniques as with silicon Photomultipliers and Silicon Drift Detectors.

The major disadvantage of $LaBr_3$ is a lack of sensitivity because of the intrinsic activity generated by ^{138}La decays, in particular at 1.4 MeV, which is relevant for the detection of ^{40}K. Full characterization of this activity in Chapter 6 led to the first experimental determination of the low-energy end of a second-order-unique-forbidden β continuum. A deviation with the standard theoretical models on nuclear decay was found of which an explanation is not at hand yet.

Development of alternative materials able to challenge $LaBr_3$ for energy resolution and efficiency but with much reduced intrinsic activity is presently ongoing. A selection of recent results achieved with $CeBr_3$ spectrometers were presented in Chapter 7, showing that $CeBr_3$ detection sensitivity at 1.4 MeV is about 8 times higher compared to $LaBr_3$.

Samenvatting

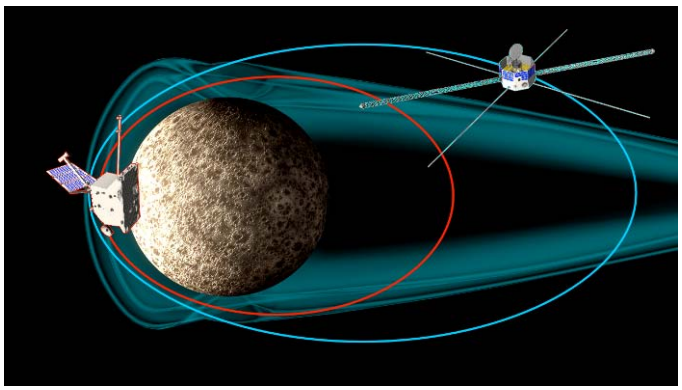

Afbeelding: BepiColombo/ESA & JAXA

Tijdens dit dissertatieonderzoek is $LaBr_3$ in het kader van een onderzoeksprogramma van ESA en de TU Delft ontwikkeld tot een scintillatie detector met een groot volume. Het programma, gericht op toepassingen van $LaBr_3$ in de ruimte, heeft ook geleid tot uitvoerige experimenten in een samenwerkingskader met vertegenwoordigers van alle ontwikkelingsaspecten, van kristalontwikkelaars tot onderzoekers van scintillatormateriaal tot eindgebruikers. Het hier gepresenteerde onderzoek is het resultaat van mijn vergaande betrokkenheid bij het programma.

Het eerste resultaat van het dissertatieonderzoek is de vaststelling van de stralingstolerantie van $LaBr_3$ in hoofdstuk 2. De instrumenten aan boord van BepiColombo moeten een protonflux van 6×10^{10} protonen/cm^2 kunnen doorstaan om succesvolle wetenschappelijke waarnemingen te garanderen. $LaBr_3$ bleek ruimschoots aan deze eis te voldoen zonder substantiële verslechtering van de prestaties. Een dergelijk vermogen, gecombineerd met de relatief geringe massa en de lage energiebehoefte die typerend zijn voor scintillatordetectoren, betekent dat $LaBr_3$ de juiste keuze is voor de gammaspectrometer aan boord van BepiColombo.

$LaBr_3$-detectie is een nieuwe technologie en experimentele studies waren noodzakelijk ter ondersteuning van het instrumentontwerp en voor optimalisering ten behoeve van ruimtetoepassingen. De afname van de prestaties bij toenemende detectorgrootte wordt nauwkeurig beschreven in hoofdstuk 4. Ook de beperkingen van de toepassing van $LaBr_3$ zijn bestudeerd en met behulp van synchrotronstraling is ontdekt dat $LaBr_3$ geen ideale

scintillator is voor fotondetectie in het röntgenstralingbereik, onder 100 keV. Gebruik van synchrotronstraling is ook effectief gebleken voor non-proportionaliteitsstudies en op grote schaal toegepast door collega's van de TU Delft.

Het uitlezen van scintillatie met behulp van $LaBr_3$ dwingt de fotomultiplicator tot de grenzen van zijn operationele mogelijkheden. Er zijn experimentele campagnes uitgevoerd om de reactie op hoogenergetische gammastraling te onderzoeken. Hiervan wordt verslag gedaan in hoofdstuk 5. Dit bood een unieke mogelijkheid om de correlatie waar te nemen tussen de energie van gammastraling en energieresolutie tot 15 MeV. Bovendien leverde het een benchmark op voor de energiecalibratiecapaciteit tijdens de vlucht. Zoals in hoofdstuk 5 van deze dissertatie wordt getoond, zijn de uitkomsten bevredigend en is $LaBr_3$ toepasbaar voor de BepiColombo-missie. Toch wijzen de uitkomsten ook op de noodzaak van nieuwe programma's om alternatieve uitleestechnieken voor scintillatie te ontwikkelen, bijvoorbeeld met silicium fotomultiplicatoren en siliciumdriftdetectoren.

Het voornaamste nadeel van $LaBr_3$ is een te lage gevoeligheid vanwege de intrinsieke activiteit die wordt gegenereerd door ^{138}La-verval, in het bijzonder bij 1,4 MeV, hetgeen relevant is voor de detectie van ^{40}K. De volledige karakterisering van deze activiteit in hoofdstuk 6 heeft geleid tot de eerste experimentele meting van het laagenergetische deel van het zogenaamd *second-order-unique-forbidden* β-continuüm. Er werd een afwijking van de theoretische standaardmodellen voor nucleair verval geconstateerd die vooralsnog niet verklaard is.

De ontwikkeling van alternatieve materialen die in staat zijn $LaBr_3$ te verslaan in energieresolutie en efficiëntie, maar met veel minder intrinsieke activiteit, is momenteel gaande. Een selectie van recente resultaten met $CeBr_3$-spectrometers wordt gepresenteerd in hoofdstuk 7. Hieruit blijkt dat de gevoeligheid van $CeBr_3$-detectie bij 1,4 MeV ongeveer 8 keer zo groot is als die van $LaBr_3$.

Acknowledgements

I warmly thank the management and my colleagues at ESA SCI-A (then SRE-PA), at TU Delft RD&M and at Praesepe B.V. for supporting and contributing to the presented research as well as for making the work exciting and the spare time very enjoyable.

I am grateful to my thesis supervisor Prof. P. Dorenbos, to Dr Alan Owens and to Dr O.R. Williams for supporting my PhD project. I have learned a lot working with you and I hope to have assisted you worthily.

I owe a special thank to Prof. P. Quarati and Prof. C.W.E. van Eijk for their contribution to Chapter 6 and to Prof. P. Brovetto for his precious encouragement.

Substantial part of my work is based on experiments carried out in external facilities: the Kernfysisch Versneller Instituut (KVI) in Groningen, the Netherlands, the Hamburger Synchrotronstrahlungslabor (HASYLAB) at DESY in Hamburg, Germany, the Laboratori Nazionali del Sud (LNS INFN) in Catania, Italy, the High Intensity Gamma-Ray Source (HγGS) at the Triangle Universities Nuclear Laboratory in Durham, North Carolina, USA, the Institute of Experimental and Applied Physics of the Czech Technical University and the Czech Metrology Institute, both in Prague, Czech Republic. I wish to thank them for their fundamental collaboration during and after the measurement campaigns.

I am grateful to the promotion committee for their constructive and helpful reviews of my thesis.

Curriculum Vitae

Professional History

From Sept. 2010, Praesepe B.V. & Delft University of Technology Delft, The Netherlands, Applied Scientist / Project Manager.
Technical manager of a research project for development of novel scintillation-based radiation-detector for application in space. The project is in collaboration with university and industry, and does include modelling, hardware evaluation and optimization.

From February 2005 till August 2010, Praesepe B.V. & European Space Agency ESTEC Advanced Studies and Technology Preparation Div. Noordwijk, The Netherlands, Research Engineer/Applied Scientist.
Conducted research and development of advanced sensors for application in space science and exploration.

November and December 2004, Czech Technical University, Institute of Experimental and Applied Physics, Prague, Czech Republic, Internship.
Collaborated in the testing of tracker detectors for the ATLAS experiment at CERN.

From September 2002 till September 2004, University of Glasgow Physics and Astronomy Department, Glasgow, UK, Research Assistant.
Participated in research and development of a X-ray imaging system for medical application in angiography targeting a drastic dose reduction to patients.

June and August 2002, Auvergne University and Spinelix S.A., Clermont-Ferrand, France, Consultant and Trainer MicroDiaGene project.
Ensured transfer of know-how developed in the previous position to the new project laboratory in France, including the training of staff and the supervision for further development.

From December 2000 till April 2002 University of Cagliari Physics Department, Cagliari, Italy, Scientific Collaborator MicroDiaGene project.
Design and implementation of a novel detection technique for nucleic acid (DNA) as well as its integration in a sequencing instrument for molecular biology.

Research interest

I concentrate on the research and development of devices and detection techniques for photons, visible, UV, X- and gamma-ray radiation. Presently, I apply my expertise supporting applications in space science and exploration.
For the last few years, I have focused on development of high-resolution scintillators sensors for applications in space science with an emphasis on the optimization of their scintillation readout for the detection of high energy gamma-ray. This includes a number of experiments in external facilities and the implementation of techniques for high energy gamma-ray production. More recently, I have focusing on the development of novel scintillator detectors with low intrinsic activity properties.
I have participated in the implementation of an original technique to experimentally replicate Solar Proton Events and undertaken an exhaustive series of experiments on germanium and other semiconductor sensors, in order to assess their capability to restore after harsh radiation damaging.
During my experience in the MicroDiaGene project I worked in a hybrid physics/molecular biology laboratory where I could successfully interface with colleagues having different professional backgrounds.

List of publications

1) Quarati, F.G.A., Khodyuk, I.V., van Eijk, C.W.E., Quarati, P., Dorenbos, P.
Study of ^{138}La radioactive decays using $LaBr_3$ scintillators
Nucl. Instr. and Meth. A 683 (2012) 46
DOI: 10.1016/j.nima.2012.04.066

2) Hansson, C.C.T., Owens, A., Quarati, F., Kozorezov, A., Gostilo, V., Lumb, D.
Synchrotron radiation studies of spectral response features caused by Te inclusions in a large volume coplanar grid CdZnTe detector
Nucl. Instr. and Meth. A 695 (2012) 283
DOI: 10.1016/j.nima.2011.10.021

3) Kroupa, M., Granja, C., Janout, Z., Kralik, M., Krejci, F., Owens, A., Pospisil, S., Quarati, F., Solc, J., Vobecky, M.
Wide energy range gamma-ray calibration source
JINST 6 (2011) art. no. T11002
DOI: 10.1088/1748-0221/6/11/T11002

4) Quarati, F.G.A., Owens, A., Dorenbos, P., De Haas, J.T.M., Benzoni, G., Blasi, N., Boiano, C., Brambilla, S., Camera, F., Alba, R., Bellia, G., Maiolino, C., Santonocito, D., Ahmed, M., Brown, N., Stave, S., Weller, H.R., Wu, Y.K.
High energy gamma-ray spectroscopy with LaBr3 scintillation detectors
Nucl. Instr. and Meth. A 629 (2011) 157
DOI: 10.1016/j.nima.2010.11.035

5) Kroupa, M., Janout, Z., Kralik, M., Krejci, F., Owens, A., Pospisil, S., Quarati, F., Solc, J.
Wide energy range gamma-ray calibration facility
IEEE NSS Conf. Rec. (2010) 352
DOI: 10.1109/NSSMIC.2010.5873779

6) Kozorezov, A., Gostilo, V., Owens, A., Quarati, F., Shorohov, M., Webb, M.A., Wigmore, J.K.
Polarization effects in thallium bromide x-ray detectors
J. App. Phys. 108 (2010) art. no. 064507
DOI: 10.1063/1.3481433

7) Quarati, F., Brandenburg, S., Buis, E.-J., Dressler, P., Kraft, S., Lampert, M.-O., Ostendorf, R.W., Owens, A., Peacock, A., Quirin, P., Quirion, D.
Solar proton event damage in space-borne Ge detectors
Nucl. Instr. and Meth. A 610 (2009) 354
DOI: 10.1016/j.nima.2009.05.108

8) Owens, A., Brandenburg, S., Gostilo, V., Ivanov, V., Ostendorf, R.W., Quarati, F., Van Den Berg, L., Van Der Graaf, E.R.
Assessment of the radiation tolerance of CdZnTe and HgI2 to solar proton events
IEEE Trans. Nucl. Sci. 56 (2009) 771
DOI: 10.1109/TNS.2009.2015307

9) Crespi, F.C.L., Camera, F., Blasi, N., Bracco, A., Brambilla, S., Million, B., Nicolini, R., Pellegri, L., Riboldi, S., Sassi, M., Wieland, O., Quarati, F., Owens, A.
Alpha-gamma discrimination by pulse shape in LaBr3:Ce and LaCl3:Ce
Nucl. Instr. and Meth. A 602 (2009) 520
DOI: 10.1016/j.nima.2009.01.101

10) Drozdowski, W., Dorenbos, P., Bos, A.J.J., Bizarri, G., Owens, A., Quarati, F.G.A.
CeBr3 scintillator development for possible use in space missions
IEEE Trans. Nucl. Sci. 55 (2008) 1391
DOI: 10.1109/TNS.2007.908579

11) Drozdowski, W., Dorenbos, P., Bos, A.J.J., Owens, A., Quarati, F.G.A.
Gamma ray induced radiation damage in 1 in × 1 in$LaBr_3$:5 %Ce
Radiation Measurements, 43 (2008) 497
DOI: 10.1016/j.radmeas.2007.11.017

12) Owens, A., Andersson, S., den Hartog, R., Quarati, F., Webb, A. and Welter, E.
An inexpensive spectroscopic beam monitor for hard X-ray synchrotron applications
JINST 2 (2007) art. no. P05002
DOI:10.1088/1748-0221/2/05/P05002

13) Owens, A., Brandenburg, S., Buis, E-J., Kozorezov, A.G., Kraft, S., Ostendorf, R.W., and Quarati, F.
Effect of prolonged annealing on the performance of coaxial Ge gamma-ray detectors
2007 JINST 2 (2007) art. no. P01001

14) Owens, A., Brandenburg, S., Buis, E.-J., Kiewiet, H., Kraft, S., Ostendorf, R.W., Peacock, A., Quarati, F., Quirin, P.
An assessment of radiation damage in space-based germanium detectors due to solar proton events
Nucl. Instr. and Meth. A 583 (2007) 285
DOI: 10.1016/j.nima.2007.07.144

15) Owens, A., Andersson, S., den Hartog, R., Quarati, F., Webb, A., Welter, E.
Hard X-ray detection with a gallium phosphide Schottky diode
Nucl. Instr. and Meth. A 581 (2007) 709
DOI: 10.1016/j.nima.2007.07.146

16) Buis, E.-J., Quarati, F., Brandenburg, S., Bos, A.J.J., Dathy, C., Dorenbos, P., Kraft, S., Maddox, E., Ostendorf, R., Owens, A.
Proton induced activation of LaBr3:Ce and LaCl3:Ce
Nucl. Instr. and Meth. A 580 (2007) 902
DOI: 10.1016/j.nima.2007.06.052

17) Owens, A., Den Hartog, R., Quarati, F., Gostilo, V., Kondratjev, V., Loupilov, A., Kozorezov, A.G., Wigmore, J.K., Webb, A., Welter, E.
Hard x-ray response of a CdZnTe ring-drift detector
J. App. Phys. 102 (2007) art. no. 054505
DOI: 10.1063/1.2776373

18) Kraft, S., Maddox, E., Buis, E.-J., Owens, A., Quarati, F.G.A., Dorenbos, P., Drozdowski, W., Bos, A.J.J., De Haas, J.T.M., Brouwer, H., Dathy, C., Ouspenski, V., Brandenburg, S., Ostendorf, R.
Development and characterization of large la-halide gamma-ray scintillators for future planetary missions
IEEE Trans. Nucl. Sci. 54 (2007) 873
DOI: 10.1109/TNS.2007.903515

19) Drozdowski, W., Dorenbos, P., Bos, A.J.J., Kraft, S., Buis, E.J., Maddox, E., Owens, A., Quarati, F.G.A., Dathy, C., Ouspenski, V.
Gamma-ray induced radiation damage in LaBr3:5%Ce and LaCl 3:10%Ce scintillators
IEEE Trans. Nucl. Sci. 54 (2007) 1387
DOI: 10.1109/TNS.2007.902373

20) Buis, E.J., Beijers, H., Brandenburg, S., Bos, A.J.J., Dathy, C., Dorenbos, P., Drozdowski, W., Kraft, S., Maddox, E., Ostendorf, R.W., Owens, A., Quarati, F.
Measurement and simulation of proton induced activation of LaBr3:Ce
Nucl. Instr. and Meth. A 578 (2007) 239
DOI: 10.1016/j.nima.2007.05.148

21) Drozdowski, W., Dorenbos, P., Bos, A.J.J., De Haas, J.T.M., Kraft, S., Maddox, E., Owens, A., Quarati, F.G.A., Dathy, C., Ouspenski, V.
Effect of proton dose, crystal size, and cerium concentration on scintillation yield and energy resolution of LaBr3:Ce
IEEE Trans. Nucl. Sci. 54 (2007) 736
DOI: 10.1109/TNS.2007.896217

22) Owens, A., Bos, A.J.J., Brandenburg, S., Dathy, C., Dorenbos, P., Kraft, S., Ostendorf, R.W., Ouspenski, V., Quarati, F.
γ-ray performance of a 1242 cm^3 $LaCl_3$:Ce scintillation spectrometer
Nucl. Instr. and Meth. A 574 (2007) 110
DOI: 10.1016/j.nima.2007.01.091

23) Owens, A., Bos, A.J.J., Brandenburg, S., Dorenbos, P., Drozdowski, W., Ostendorf, R.W., Quarati, F., Webb, A., Welter, E.
The hard X-ray response of Ce-doped lanthanum halide scintillators
Nucl. Instr. and Meth. A 574 (2007) 158
DOI: 10.1016/j.nima.2007.01.092

24) Quarati, F., Bos, A.J.J., Brandenburg, S., Dathy, C., Dorenbos, P., Kraft, S., Ostendorf, R.W., Ouspenski, V., Owens, A.
X-ray and gamma-ray response of a 2″×2″ LaBr3:Ce scintillation detector
Nucl. Instr. and Meth. A 574 (2007) 115
DOI: 10.1016/j.nima.2007.01.161

25) Owens, A., Bos, A.J.J., Brandenburg, S., Buis, E.-J., Dathy, C., Dorenbos, P., van Eijk, C.W.E., Kraft, S., Ostendorf, R.W., Ouspenski, V., Quarati, F.
Assessment of the radiation tolerance of LaBr3:Ce scintillators to solar proton events
Nucl. Instr. and Meth. A 572 (2007) 785
DOI: 10.1016/j.nima.2006.12.008

26) Quarati, F., Hijmering, R.A., Maehlum, G., Owens, A., Welter, E.
Evaluation of a CdZnTe pixel array for X- and γ-ray spectroscopic imaging
Nucl. Instr. and Meth. A 568 (2006) 446
DOI: 10.1016/j.nima.2006.06.018

27) Sun, G.C., Mañez, N., Rao, R., Bourgoin, J.C., Smith, K.M., Quarati, F., Al-Ajili, A.
Application of epitaxial GaAs to medical imaging
IEEE Trans. Nucl. Sci. 53 (2006) 1671
DOI: 10.1109/TNS.2006.876775

28) Buis, E.-J., Beijersbergen, M., Kraft, S., Owens, A., Quarati, F., Brandenburg, S., Ostendorf, R.
New scintillators for focal plane detectors in gamma-ray missions
Experimental Astronomy, 20 (2005) 333
DOI: 10.1007/s10686-006-9027-4

29) Quarati, F., O'Shea, V., Smith, K.M.
Image quality of Medipix2 assemblies with silicon detectors of two different thicknesses
Nucl. Instr. and Meth. A 546 (2005) 42
DOI: 10.1016/j.nima.2005.03.039

30) Blue, A., Grant, J., Cunningham, W., Quarati, F., Smith, K.M., Rahman, M., O'Shea, V., Manolopoulos, S.
GaN UV detectors for synchrotron-based protein structure studies
Nucl. Instr. and Meth. A 546 (2005) 131
DOI: 10.1016/j.nima.2005.03.115

31) Sun, G.C., Mañez, N., Zazoui, M., Al-Ajili, A., Davidson, D.W., O'Shea, V., Quarati, F., Smith, K.M., Chambellan, D., Gal, O., Pillot, Ph., Lenoir, M., Montagne, J.P., Bchetnia, A., Bourgoin, J.C.
State of the art on epitaxial GaAs detectors
Nucl. Instr. and Meth. A 546 (2005) 140
DOI: 10.1016/j.nima.2005.03.110

32) Salis, M., Anedda, A., Quarati, F., Blue, A.J., Cunningham, W.
Photocurrent in epitaxial GaN
J. App. Phys. 97 (2005) art. no. 033709
DOI: 10.1063/1.1848191

33) Sun, G.C., Mañez, N., Rao, R., Bourgoin, J.C., Smith, K.M., Quarati, F., Al-Ajili, A.
Progress on epitaxial GaAs detectors
IEEE NSS Conf. Rec. 7 (2004) 4273
DOI: 10.1109/NSSMIC.2004.1466834

34) Quarati, F., Cadeddu, S., Lai, A., Sesselego, A., Caria, M.
Fabrication process validation for a double-sided silicon pixel detector
Nucl. Instr. and Meth. A 509 (2003) 92
DOI: 10.1016/S0168-9002(03)01555-9

35) Quarati, F., Quarati, P.
Phase space cell in nonextensive classical systems
Entropy, 5 (2003) 239
doi:10.3390/e5020239

36) Caria, M., Cadeddu, S., Lai, A., Sesselego, A., Quarati, F.
Characterization of a silicon pixel detector for imaging with low energy radiation
Nucl. Instr. and Meth. A 487 (2002) 170
DOI: 10.1016/S0168-9002(02)00961-0

37) Brovetto, P., Maxia, V., Quarati, F., Salis, M.
Radioluminescence investigation of Nasicon materials
Materials Research Bulletin, 35 (2000) 1797
DOI: 10.1016/S0025-5408(00)00389-5

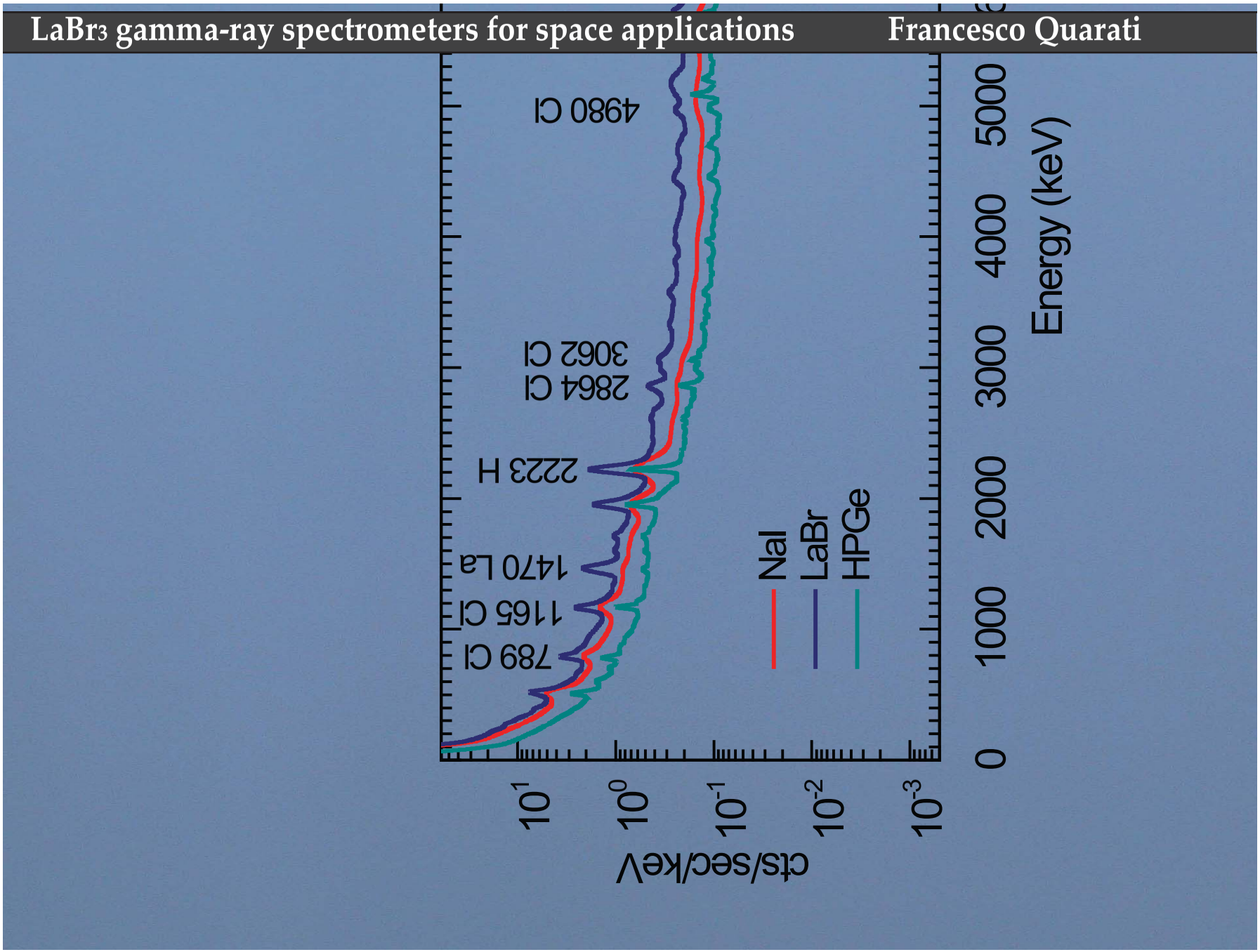
4980 Cl
3062 Cl
2864 Cl
2223 H
1470 La
1165 Cl
789 Cl
NaI
LaBr
HPGe
cts/sec/keV
10^{1}
10^{0}
10^{-1}
10^{-2}
10^{-3}
0
1000
2000
3000
4000
5000
Energy (keV)